SATELLITE-BASED CLOUD REMOTE SENSING: FAST RADIATIVE TRANSFER MODELING AND INTER-COMPARISON OF SINGLE-/MULTI- LAYER CLOUD RETRIEVALS WITH VIIRS

A Dissertation

by

YIFENG DING

Submitted to the Office of Graduate and Professional Studies of
Texas A&M University
in partial fulfillment of the requirements for the degree of

DOCTOR OF PHILOSOPHY

Chair of Committee,	Ping Yang
Committee Members,	Andrew Dessler
	Kenneth Bowman
	Casey Papovich
Head of Department,	Ping Yang

August 2017

Major Subject: Atmospheric Sciences

ABSTRACT

This dissertation consists of three parts, each of them, progressively, contributing to the problem of great importance that satellite-based remote sensing of clouds.

In the first section, we develop a fast radiative transfer model specialized for Visible Infrared Imaging Radiometer Suite (VIIRS), based on the band-average technique. VIIRS, is a passive sensor flying aboard the NOAA's Suomi National Polar-orbiting Partnership (NPP) spacecraft. This model successfully simulates VIIRS solar and infrared bands, in both moderate (M-bands) and imagery (I-bands) spatial resolutions. Besides, the model is two orders of magnitude faster than Line-by-line & discrete ordinate transfer (DISORT) method with a great accuracy.

The second and third parts are going to investigate the retrieval of single-/multi-layer cloud optical properties, especially, cloud optical thickness (τ) and cloud effective particle size (D_e) with different methods. By presenting the comparison between results derived from VIIRS measurements and benchmark products, potential applications of Bayesian and OE retrieval methods for cloud property retrieval are discussed. It has proved that Bayesian method is more suitable for single-layer scenarios with fewer variables with fast speed, while Optimal Estimation method is superior to Bayesian method for more complicated multi-layer scenarios.

ACKNOWLEDGEMENTS

I am going to take this opportunity to express my most sincere thanks to my advisor, Dr. Ping Yang, for his guidance, patience and encouragement throughout my Ph.D. study. He is not only an advisor for me, but also a true mentor who cares about my future and career. I would also send my gratitude to all my committee members. I am tremendously fortunate to Dr. Dessler, Dr. Bowman, and Dr. Papovich. Dr. Dessler gave me a lot help that few could match for the presentation skills. Dr. Bowman and Dr. Papovich also provided me many constructive comments.

I would especially thank Drs. Bryan Baum and Aronne Merrelli for the fruitful discussion and generous support. I would thank Dr. Shaima Nasiri, who is kind, gracious, and a mentor beyond compare. I would also like to thank Drs. Binqi Yi, Chenxi Wang, Guanglin Tang, Chao Liu and other group members for their advice and help on my research and life.

Last, I am going to thank my family and friends, especially, my parents, Yunbai Ding and Lan Fu. They all kept me going and selfless dedicated to help me throughout all these years.

CONTRIBUTORS AND FUNDING SOURCES

Contributors

This work was supervised by a dissertation committee consisting of Professor Yang, Professor Dressler and Professor Bowman of the Department of Atmospheric Science and Professor Papovich of the Department of Physics.

All work conducted for the dissertation was completed by the student independently.

Funding Sources

This study was partly supported by a subcontract (Contract Number: 629K996) from the University of Wisconsin (the primary grant awarded to the University of Wisconsin: NASA Grant NNX14AP65A) and a NASA grant (NNX12AL90G).

NOMENCLATURE

τ	Optical Thickness
D_e	Particle Effective Diameter
Q_e	Extinction Efficiency
ρ	Density
σ	Cross Section
ε	Underlying Surface Emissivity
β	Ratios of Absorption Optical Depths
ω_o	Single Scattering Albedo
g	Asymmetry Factor

CKD	Correlated-K Distribution
CRF	Cloud Radiative Forcing
GCM	General Circulation Model
LBLRTM	Line-by-line radiative transfer model
LUT	Look-up Table
SRF	Spectral Response Function
RTM	Radiative Transfer Model
OLR	Outgoing Longwave Radiation
TC4	Tropical Composition, Cloud and Climate Coupling
TOA	Top of Atmosphere
VFRTM	VIIRS fast radiative transfer model

TABLE OF CONTENTS

Page

LIST OF FIGURES

Page

LIST OF TABLES

Page

1. INTRODUCTION

1.1. The role of cirrus clouds in climate

In daily life, cloud is one of the most common things, which could be seen nearly everywhere. Among all types of clouds, ice cloud, especially, thin ice cloud plays a major role in the earth's surface and atmosphere radiation budget (Herman et al., 1980; Hartmann and Short 1980). Cirrus is a genus of ice cloud generally characterized by thin, wispy strands. Cirrus clouds are thin ice cloud, usually above 6000m, that can hardly be seen with the naked eye, and cover more than 20% of the earth (Liou, 1986; Stubenrauch et al., 2006; Iwabuchi et al., 2014). They are scientifically interesting because they allow most incoming sunlight to pass through, but help to contain heat emitted from the surface, so cirrus clouds exert a warming influence on Earth's surface, and have a powerful effect on local and global climate (Baran, 2012; Yang et al., 2015). By reflecting the incoming sunlight back to space and reducing the outgoing longwave radiation (OLR), cirrus cloud has presented two opposing radiative effects, cooling and heating, on the earth, which depends on many factors, including cloud lifetime, cloud amount, cloud optical thickness, cloud top height, cloud effective particle size, and cloud particle habit, as well as the distribution of water content within the atmosphere and low-layer water clouds or aerosols (Ackerman et al., 1988; Hartmann et al., 2001). Antagonism of the cirrus cloud arises a complicated problem to give a straightforward answer to the question that cirrus has a positive or negative effects on the earth surface cooling process. Generally, the net high and thin cirrus cloud has a positive net cloud radiative forcing (CRF) at the top of

atmosphere (TOA) (McFarquhar et al., 2000), meanwhile the CRF of thick cloud anvils can be negative (Jensen et al., 1994). So that, it is a big challenge to accurately reproduce the cirrus cloud associated radiative transfer process in global climate models, and better quantified cirrus cloud optical properties are necessarily needed.

The formation and life time of cirrus cloud is determined by the distribution of water vapor and atmosphere dynamics (Newell et al., 1996), meanwhile cirrus cloud, in turn, has an effect on the re-distribution of atmosphere water vapor. Cirrus clouds are often observed near tropopause in tropics and over the water (Dessler and Yang, 2003), suggesting that cirrus cloud might be involved in the troposphere and stratosphere water vapor interaction (Hartmann et al., 2001). Overall, the influence of cloud on atmospheric radiation budget is still an unsolved puzzle, making it one of the hottest topics to measure the altitude and properties of cloud and to get information on the relationship between clouds and climate. To settle these problems, many observing satellites, like CloudSat and CALIPSO (Cloud-Aerosol Lidar and Infrared Pathfinder Satellite Observations) have been launched into the space. Besides, there are many scientific campaigns focusing on cirrus study, such as CRYSTAL- FACE (or, Cirrus Regional Study of Tropical Anvils and Cirrus Layers- Florida Area Cirrus Experiment, Jensen et al. 2004) and recent TC4 (Tropical Composition, Cloud and Climate Coupling) experiments. These *in-situ* measurements provided the theoretical basis of cloud modeling and remote sensing. However, the limitation of high price and limited spatial and temporal sampling makes it impossible to study continuous cloud global distribution and optical properties with *in-*

situ method. So that, satellite-based instruments become an absolutely necessary technique to study cloud.

1.2. The role of multi-layer clouds in climate

Apart from horizontally and vertically homogeneous cloud system, i.e. single-layer cloud system, which is the most idealized model in radiative transfer simulation, multi-layer clouds are of great importance as well. Like cirrus cloud, multi-layer cloud is another kind of cloud raises concerns. Inferred from global water vapor profile data, it suggests that over 40% of the global cloud systems involves multi-layer clouds (Poore et al., 1995; Wang et al., 2000). Cloud vertical structures also affect the global atmospheric circulation through direct heating/cooling and latent heating (Webster and Stephens, 1980; Wang and Rossow, 1998). What's more, cloud multi-layer structure also introduces a significant uncertainty in general circulation models (GCMs). Derivation of cloud properties is compromised when multi-layer clouds are presenting but single-layer clouds are assumed. For these compromised retrievals, i.e. treated as single-layer clouds, however, actually are multi-layer ones, the results usually lie between the layer properties: cloud heights lie lower than the upper layer and higher than the lower one; effective particle sizes are between water cloud droplets and ice cloud particles as well (Davis, et al., 2009). Considering the widely occurrences of multi-layer scenarios, it is of importance to derive an accurate representation of these clouds with the help of satellite-based observations.

1.3. Satellite based modeling and retrieving of clouds

Satellite data can provide consistent measurements to infer the global distribution of clouds, and scores of retrieval methods have been developed to obtain cloud optical properties such as optical thickness(τ) and ice particle effective diameter(D_e) based on various satellite instruments over the past several decades. In order to obtain reliable retrieval results of cloud properties from satellite observations, we have to have a good understanding of the instrument characteristics and capabilities. In addition to that, a good understanding of microphysical and scattering properties of ice particles is also required by traditional visible and near-infrared (VNIR) based technique, if not, large uncertatinties could be introduced because of the variability of ice cloud particle shapes (Cooper et al., 2006). Consistent thermal IR observations in both daytime and nighttime makes it not only possible to understand the complete cloud diurnal cycle, but also feasible to derive ice cloud optical properties because of the relatively insensitive to smooth or rough cloud particle surface and various ice particle shapes. Therefore, we are going to focus on using thermal IR measurements derive cloud properties.

1.3.1. Microphysical properties of ice clouds

Since properties of water cloud droplet can be perfectly reproduced by sphere model, here we will focus on ice cloud particles. From in situ aircraft observations, it has been determined that ice clouds are almost exclusively composed of nonspherical ice particles, including bullets, columns, and plates (Heymsfield and Platt, 1984). Therefore, the microphysical properties of ice clouds have to be understood before modeling the ice

cloud particles. Based on the assumption that cirrus clouds are plane-parallel and homogeneous. The geometric thickness of cirrus clouds is assumed to be thin enough to adapt to the needs of fast model; and the optical thickness cirrus clouds have to be thick enough to be detected by satellite instruments.

According to *in-situ* measurements, there can be a large range of different sizes of ice cloud particles within the same cloud, ranging from a few micrometers to millimeters (Auer and Veal 1970). However, it has been confirmed that the effective diameter (D_e) instead of exact cloud particle size distribution determines the radiative properties of clouds, such as extinction efficiency, asymmetry factor and so on (Hansen and Travis 1974). The effective diameter (D_e) of an ice particle distribution is defined as follows:

$$D_e = \frac{3}{2}\frac{V_{total}}{A_{total}}, \tag{1.1}$$

where V_{total} and A_{total} are the total volume and total projected area of ice particles within a certain volume of ice cloud. Expressed with particle size distribution format, the effective diameter (D_e) can be formulated as follows:

$$D_e = \frac{3}{2}\frac{\sum_{i=1}^{N} V_i}{\sum_{i=1}^{N} A_i}, \tag{1.2}$$

where V_i and A_i are the volume and projected area of different sizes of particles over the particle size distribution. In this study, the particles are assumed to a gamma distribution with a relative standard deviation of 0.1. Ice particle effective diameter (D_e) can also be described by two important quantities, ice wat content (*IWC*) and extinction coefficient (β_e), as well. That is:

$$D_e = \frac{3}{2}\frac{IWC\langle Q_e\rangle}{\rho_{ice}\beta_e}, \tag{1.3}$$

where $\langle Q_e\rangle$ is the averaged extinction efficiency and ρ_{ice} is the ice density. In order to better compare the optical thickness of ice cloud, we usually convert that to visible region (0.65 μm) optical thickness, which can be derived as follows:

$$\tau_\lambda = \tau_{\mathrm{vis}}\frac{\langle Q_\lambda\rangle}{\langle Q_{vis}\rangle}, \tag{1.4}$$

where $\langle Q_\lambda\rangle$ represents the averaged bulk extinction efficiency at wavelength λ and $\langle Q_{vis}\rangle$ is the averaged bulk visible region extinction efficiency, which is approximately a constant of 2. Both of $\langle Q_\lambda\rangle$ and $\langle Q_{vis}\rangle$ depend on the particle effective diameter D_e.

As mentioned before, ice cloud particles are composed of nonspherical shapes, such as bullets, columns, plates and so on. Ice cloud particle shapes play an important role in identify the effective diameter D_e of ice particles. Therefore, an unrepresentative shape of ice particle may result in consequential errors in cloud property retrieval. In this study, the Moderate Resolution Imaging Spectro-radiometer (MODIS) Collection 6 (MC06) ice cloud model (Platnick et al., 2017) is used, which adopts a single ice habit consisting of an aggregate of 8 hexagonal columns with severely roughened surfaces. The MC06 ice particle habit was chosen because it minimizes the differences in the τ retrievals between those from CALIPSO and the IR split-window method (Baum et al., 2014; Holz et al., 2015). It should be noted that the linear polarization properties of this habit do not match well with those from POLDER/PARASOL (Baum et al., 2014), and further that the CALIPSO comparisons were limited to $\tau < 3$ (Holz et al., 2015). Note that throughout this study, all optical thicknesses are related to a visible wavelength of 0.65 μm.

1.3.2. Bulk scattering properties of ice clouds

Bulk scattering properties, or volumetric scattering properties, describe the scattering behavior presented by sufficiently small volume containing many individual particles, which can be derived by averaging the optical properties of individual particles over the particle size distribution and spectral response function for instrument bands. For example, the bulk scattering cross section is:

$$\bar{\sigma}_{sca} = \frac{\int_{\lambda_1}^{\lambda_2}\int_{D_{max}}^{D_{min}} \sigma_{sca} n(D) F(\lambda) S(\lambda) dD d\lambda}{\int_{\lambda_1}^{\lambda_2}\int_{D_{max}}^{D_{min}} n(D) F(\lambda) S(\lambda) dD d\lambda}, \tag{1.5}$$

where D is the ice particle size, n(D) is the particle number density, $S(\lambda)$ is the spectral solar spectrum, and $F(\lambda)$ is the spectral response function (Baum et al., 2005).

1.3.3. Remote sensing of cloud properties from satellite-based instruments

So called "forward model" of satellite-based remote sensing, essentially, is a numerical solver of radiative transfer model:

$$Y = F(x)\ , \tag{1.6}$$

In Eq. (1.6), x is a vector represents the input parameters of the radiative transfer model, including the bulk scattering properties of cloud described before and the surrounding environment parameters, such as surface temperature, atmosphere profile, and so on. Y is the satellite-based instrument observed radiances or brightness temperature. Function F represents the radiative transfer process.

In contrast, the question of finding the best representation of the cloud bulk scattering properties or environment parameters given the observation is inverse problem (Rodgers, 2000). In radiative transfer field, remote sensing is used to solve this kind of "inverse problem":

$$x = F^{-1}(Y) \ , \tag{1.7}$$

In remote sensing problem, satellite measurements, *Y*, are given. From this point of view, an accurate radiative transfer model is the prerequisite of remote sensing problem, and remote sensing is one of the most important application of radiative transfer model.

To specify the numerical radiative transfer model, there are many different ones based on various theories, such as discrete-ordinate method (Chandrasekhar 1960; Stamnes et al. 1988; Liou 1973), the Monte Carlo method (Plass and Kattawar, 1968) and adding-doubling method (Hansen and Hovenier 1971; Irvine 1968; Lacis and Hansen 1974). Most of above mentioned methods are rigorous methods and have been implemented in either research or operational remote sensing program.

A large number of satellite-based instruments have been launched into the space to study the global distribution of cloud and earth-atmosphere system energy budget, such as the Moderate resolution Imaging Spectroradiometer (MODIS), the Polarization and Directionality of the Earth's Reflectances (POLDER), and the Visible Infrared Imager Radiometer Suite (VIIRS). In the past decades, many passive sensor based methods using imagers and sounders can be divided into the following categories: (1) infrared(IR) split-window methods using thermal infrared bands (Inoue, 1985, Parol et al., 1991); (2) solar-reflection-based retrieval algorithms using a pair of visible and shortwave-infrared

(VSWIR) wavelength channels (Nakajima and King, 1990); and (3) other IR band based methods (e.g., Minnis et al., 2011; Heidinger et al., 2015;). The bi-channel solar-reflection-based method uses VSWIR bands to derive cloud optical and microphysical properties only in daytime. Also, for thin ice clouds, such as cirrus, this VSWIR method may introduce large uncertainties because of the variability of ice cloud particle shapes (Cooper et al., 2006). Consistent IR observations in both daytime and nighttime makes it possible to understand the complete cloud diurnal cycle. In addition, the relatively insensitivity of split-window IR method to smooth or rough cloud particle surface and various ice particle shapes make it more feasible to derive ice cloud properties.

1.4. Previous work and new solutions

As previous sections mentioned, satellite-based remote sensing is capable to offer continuously spatial and temporal cloud global distribution and optical properties. Great achievement has been made with the help of recent advanced technologies, such as NASA's "A-Train" satellite project. It has provided unprecedented access to better understand clouds. The "A-Train" satellite project consists of six polar- orbiting satellites flying one after another within a short time delay (Stephens et al., 2002; Anderson et al. 2005). With the help of nearly simultaneous data from those satellites, comprehensive information concerning dust, aerosols, clouds, atmospheric profiles, and radiative field quantities can be obtained. Take this opportunity, many problems, like climate change, cloud feedback (Chepfer et al., 2008), and effects of aerosols (Yu et al., 2006), have been studied from an unprecedented perspective. During the time, a number of very useful

clear-sky fast radiative transfer models have been developed (Moncet et al. 2004; Liu et al. 2006). Meanwhile, to some degree, a little fewer fast radiative transfer models for cloudy-sky were available (Wei et al., 2004). It is the “A-Train” constellation that provides an unprecedented chance to compare nearly simultaneous retrievals with different instruments, like MODIS and POLDER.

Suomi National Polar-orbiting Partnership (Suomi NPP), which was originally named NPOESS Preparatory Project (NPP), is named after Verner E. Suomi, widely recognized as the "Father of Satellite Meteorology." It is the first next generation polar-orbiting satellite in the JPSS (The Joint Polar Satellite System) series, and is considered to be a part of future possible “J-Train” constellation, the successor of “A-Train” constellation. VIIRS onboard NPP has an even higher spatial resolution compared with MODIS, which is considered to have a potential to provide opportunities to improve our understanding of clouds.

1.5. Dissertation organization

This dissertation is organized as following three major sections. In section 2, we are going to present a VIIRS specialized fast radiative transfer model based on band average and correlated-k distribution (CKD) techniques. In section 3, we will discuss the simpler problem: optical properties of single-layer cirrus clouds with different retrieval methods. In section 4, we will take a step forward to talk about multi-layer clouds optical property retrieval. Then real case study will be analyzed as supporting evidence.

2. FAST INFRARED RADIATIVE TRANSFER MODEL BASED ON CORROLATED-K DISTRIBUTION METHOD FOR VIIRS BAND-AVERAGED SIMULATION

2.1. Background

At any point in time, on average, two thirds of the Earth experiences cloud cover, and with the inclusion of sub-visible cirrus clouds, this number increases to nearly 73% (Stubenrauch et al, 2013). Though globally distributed, clouds are more prevalent over ocean than land, with cirrus clouds, in particular, found at all latitudes with no regard to season or land cover (Fu and Liou, 1993). On a global scale, cirrus accounts for 20-30% of all cloud cover, but in the tropics where they are the most prevalent, that cloud cover percentage increases to at least 60-70% (Fu and Liou, 1993; Meyer, 2004; Baran, 2009). With cirrus clouds high in the troposphere and temperatures at the tropopause colder than -50°C, cirrus clouds are made up almost exclusively of nonspherical ice crystals of various shapes, sizes, and roughnesses. Baumgardner and Baran show via in-situ measurements that hexagonal columns, plates, and bullet-rosettes are the most common ice crystal habits found within cirrus clouds (Baumgardner et al., 2005; Baran, 2009).

Viewing cirrus clouds in the longwave (far) infrared (IR) portion of the electromagnetic spectrum may hold the key to understanding the radiative effects of cirrus clouds. The best method for understanding the radiative effects of cirrus clouds is to obtain and analyze the brightness temperatures (BT) or the measure of the amount of Top of Atmosphere (TOA) radiance in a given area. Formally, BT is “a descriptive measure of

radiation in terms of the temperature of a hypothetical blackbody emitting an identical amount of radiation at the same wavelength."

By simulating and analyzing BT and brightness temperature difference (BTD), dependencies on optical thickness (τ) and effective diameter size (D_e) arise and the accuracy of the RTM can be tested. Having an RTM that can be used for operational applications such as remote sensing data retrievals, cloud cover maps, or data assimilation is imperative. Zhang et al. showed the importance for an RTM to be computationally efficient and accurate, as well as applicable to a variety of conditions (Zhang et al., 2007). The fast infrared radiative transfer model (FIRTM-AD) used here was developed using the adding-doubling principle. Using a vertically inhomogeneous, multilayer, plane parallel atmosphere, the FIRTM-AD is a clear sky model that can also account for molecular absorption and an RTE solver that accounts for multiple scattering in cloud layers are developed. The development of a fast RTM (FRTM) by Wang et al., 2011 that uses parametrizations (such as CKD) to minimize computational effort for high-spectral radiance simulations, is helpful for operational needs. Liu et al. 2014 study develops an FRTM that uses CKD to minimize computation time for gaseous absorption and places an emphasis on simulating VIIRS data while allowing for application to other imagers. By creating a CKD model for each spectral channel associated with VIIRS, gaseous absorption could be calculated quickly for each channel. Transmissivities for the clear sky case were calculated using a US Standard Atmospheric Profile, along with MODIS Collection 6 cloud habit. Results are averaged over the spectrum using spectral response functions (SRF).

This study develops a specialized VIIRS IR band fast RTM for cloudy-sky, using correlated-k distribution theory based band-average and precomputed look-up table (LUT) techniques to reduce the computational burden. The atmospheric molecule transmissivity and cloud optical properties are key factors for the RTM, dealt with correlated-k distribution method and LUT technique, respectively. This work is mainly based on (Liu et al., 2015). Section 2.2 describes the approach of gaseous transmissivity, and section 2.3 discusses the cloud optical properties. Section 2.4 describes the simulator itself and validation of the RTM. comparison between simulated results and observations are described in section 2.5. Section 2.6 will summarize the study.

2.2. Approach of gaseous transmissivity

Compared with line-by-line rigorous calculation, like LBLRTM (Clough et al., 1992), the most distinguished advantage of CKD method is the hard-to-match high efficiency to compute the atmospheric molecule absorption. Instead of integration the gas transmissivity over highly variable spectral space, CKD method just calculates a counterpart of that over a less changed absorption coefficient space, shown in Figure 2.1. The spectral absorption coefficient (K) of gas versus wavenumber is plotted in Figure 2.1(a), which is highly variable. The accuracy of spectral absorption coefficient depends on the resolution of line-by-line calculation wavenumber grid. The finer the wavenumber grid is, the higher accuracy of spectral absorption coefficient will be. However, the sequence of the spectral absorption lines does not affect the effective transmissivity with a given spectral resolution, and thus, instead of integrating over the spectral space, spectral

absorption coefficient can be expressed as a function of cumulative probability(g), Figure 2.1(c) (Liu et al., 2015). The gaseous transmissivity (T_{gas}) is:

$$T_{gas} = \frac{1}{\Delta\nu}\int_{\Delta\nu} e^{-k(\nu)u}d\nu = \int_{k_{min}}^{k_{max}} e^{-k(\nu)u} f(k)dk, \tag{2.1}$$

where *k(v)* is the gas spectral absorption coefficient at wavenumber *v*, and *u* is the path length; *f(k)* is the normalized probability distribution function for *k(v)*. Define the cumulative probability function *g(k)* as:

$$g(k) = \int_{k_{min}}^{k} f(k')dk', \tag{2.2}$$

So that, combine (2.1) and (2.2),

$$T_{gas} = \int_0^1 e^{-k(g)u}dg, \tag{2.3}$$

Thus, the spectral absorption coefficient can be described by a function of *g*, instead of wavenumber *v*. This approximation process is called *k* distribution method, shown in Figure 2.1(c). Since this conclusion is based on the hypothesis of idealistic homogeneous atmosphere, implementation of CKD method for realistic inhomogeneous atmosphere requires that the order of absorption line strength is the same for all levels.

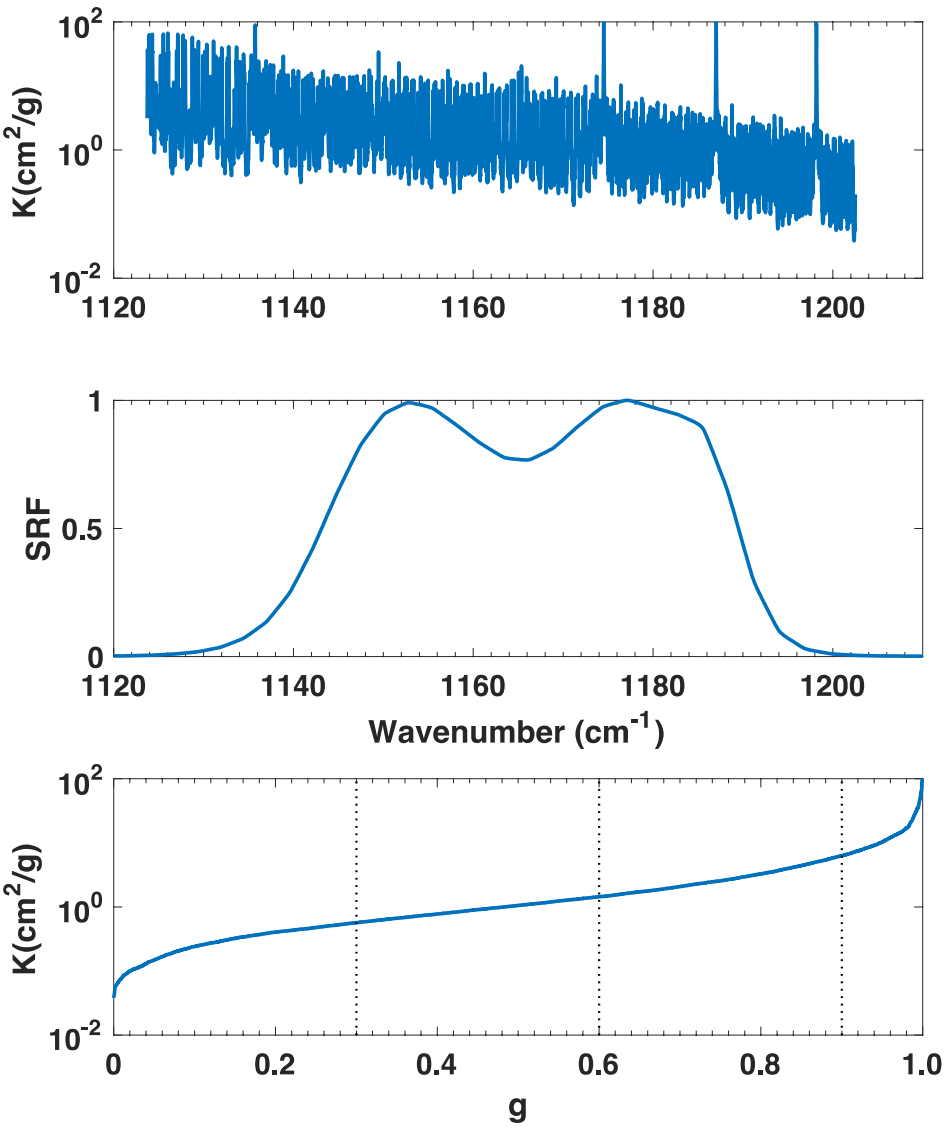

Figure 2.1 Example of the correlated-k process of mixed gas absorption lines for the VIIRS M14 (8.55μm) channel. (a) Absorption coefficient as a function of wavenumber (cm-1) for mixed gas of H_2O, O_3, and N_2O with the ratio of the three gases being 1:0.1:0.001. (b) Spectral response function. (c) Absorption coefficient as a function of cumulative probability (g) for the mixed gas with the spectral response function.

Figure 2.2 shows the performance of CKD method calculated VIIRS bands transmissivity and TOA brightness temperature bias compared with LBLRTM+DISORT results with 42 typical atmospheric profiles at wavelength 8.55 μm, 10.76 μm, 12.01 μm (M14, M15, and M16), provided by Atmospheric and Environmental Research (AER) Radiative Transfer Working Group. Figure 2.2 illustrates the accuracy of CKD results for clear-sky scenarios, indicating that the relative errors in transmissivity are less than 0.3% for the worst cases. Generally, large errors happen when profile has high content of low layer water vapor. In this validation process, all profiles are divided into 50 layers, 1 km thick respectively. The gas transmissivity computed by the CKD method will be used to simulate brightness temperatures under cloudy conditions.

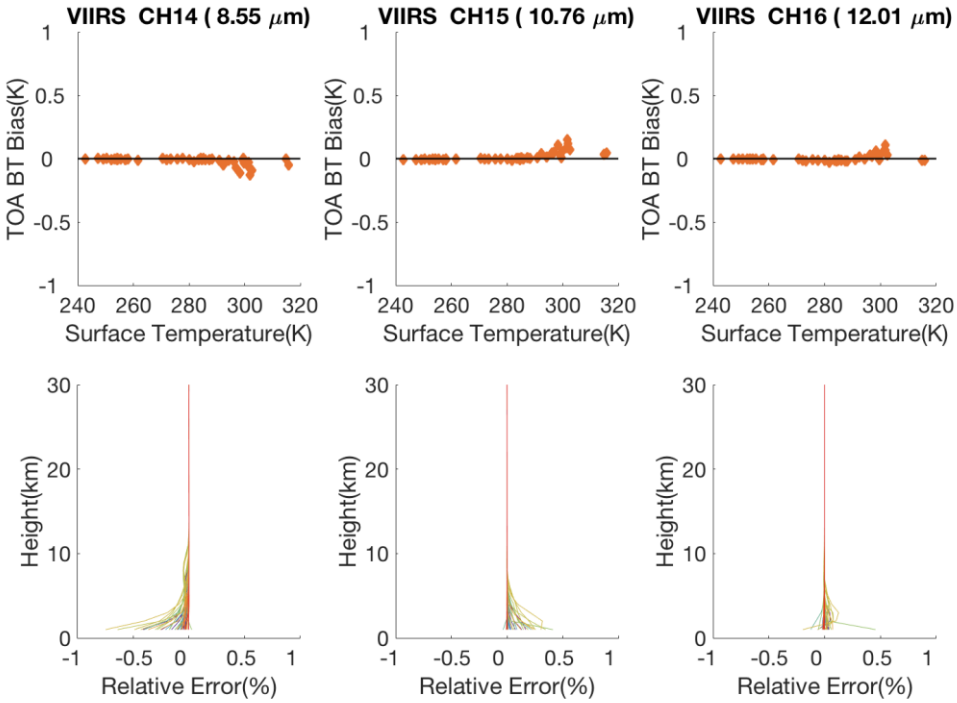

Figure 2.2 CKD models for VIIRS were validated using 42 typical profiles throughout the world provided by AER.com. The upper panels show the generally low bias between the rigorous LBLRTM +DISORT method results and fast CKD method results. The lower panels show that relative errors between the LBLRTM results and CKD method are also low.

2.3. Cloud optical properties

Clear-sky scenarios are the simplified models, while cloudy-sky cases, for both liquid and ice clouds, are required by simulations. A set of cloud particle single-scattering properties at individual sizes and wavelengths, or wavenumbers, has been averaged over the VIIRS channel SRFs and assumed particle size distributions.

For liquid cloud particles, the single-scattering properties are derived with Lorenz-Mie theory (Mie, 1908) with the size distribution assumed to be gamma distribution, and the effective variance equals to 0.1 (Hansen and Travis, 1974). For ice phase clouds, this study uses the Moderate Resolution Imaging Spectroradiometer (MODIS) Collection 6 (MC06) ice cloud model (Platnick et al., 2017), which adopts a single ice habit consisting of an aggregate of 8 hexagonal columns with severely roughened surfaces. The MC06 ice particle habit was chosen because it minimizes the differences in the τ retrievals between those from CALIPSO and the IR split-window method (Baum et al., 2014; Holz et al. 2015). It should be noted that the linear polarization properties of this habit do not match well with those from POLDER/PARASOL (Baum et al. 2014), and further that the CALIPSO comparisons were limited to $\tau < 3$ (Holz et al. 2015). Note that throughout this study, all optical thicknesses are related to a visible wavelength of 0.65 μm.

The effective diameter (D_e) of an ice particle distribution is defined as follows:

$$\mathrm{D_e} = \frac{3}{2}\frac{\sum_{i=1}^{N} \mathrm{V_i}}{\sum_{i=1}^{N} \mathrm{A_i}}, \tag{2.4}$$

where $\mathrm{V_i}$ and $\mathrm{A_i}$ are the volume and projected area of different sizes of particles over the particle size distribution. In this study, the particles are assumed to a gamma distribution with a relative standard deviation of 0.1.

2.4. VIIRS simulator and validation

This study will focus on VIIRS IR bands. Wang et al. 2011 and Wang et al. 2014 are the theoretical basis to simulate the TOA brightness temperature for this model. Similar to the FRTM developed by Wang, look-up tables of cloud properties with various

optical thickness and effective diameter pairs are pre-calculated to reduce the computation burden of cloud layer effects, including the reflectance, transmittance and emissivity. The CKD technique discussed in section 2.2 is used to calculate the atmospheric gas absorption. Generally, the TOA brightness temperature difference (BTDs) between fast model rigorous LBLRTM+DISORT method are smaller than 0.3K. As for the computational efficiency, fast model is about 3 orders of magnitude faster than the rigorous method with 32 streams.

Latest DISORT code (DISORT 2.0 beta) is used as control group rigorous method as well as the module to calculate the look-up tables for fast band-averaged optical properties. To validate the simulator at the IR channels, Figure 2.3 illustrates the brightness temperature differences (BTDs) given by the simulator and the LBLRTM+DISORT at three IR channels (M14, M15, and M16). The BTD is defined as:

$$\mathrm{BTD} = \mathrm{BT}_{\mathrm{Simulator}} - \mathrm{BT}_{\mathrm{LBLRTM+DISORT}}, \tag{2.5}$$

Figure 2.3 shows validation of CKD models for VIIRS using 42 typical profiles same as Figure 2.2. The upper panels show the TOA brightness temperatures between the rigorous LBLRTM +DISORT method results and fast CKD method results. The lower panels show the TOA brightness temperature differences between the LBLRTM results and CKD method. Different colors refer to different sets of optical thickness and effective diameter pairs. Each panel of Figure 2.3 is based on a surface albedo of 0.02 and viewing zenith of 20° under 42 typical profiles and 18 cloud optical properties pairs. The bias in the BTDs are smaller than 0.3 K and decrease to less than 0.1 K for optically thick clouds. With the spectral resolution being 0.1 cm-1, 32-stream DISORT simulations were carried

out for each VIIRS channel, and the simulator is approximately 20,000 times faster than the LBLRTM+DISORT. Need to mention that the validation results in Figure 2.3 are based on ice clouds. Water cloud scenarios indicate similar performance as ice ones which is not shown.

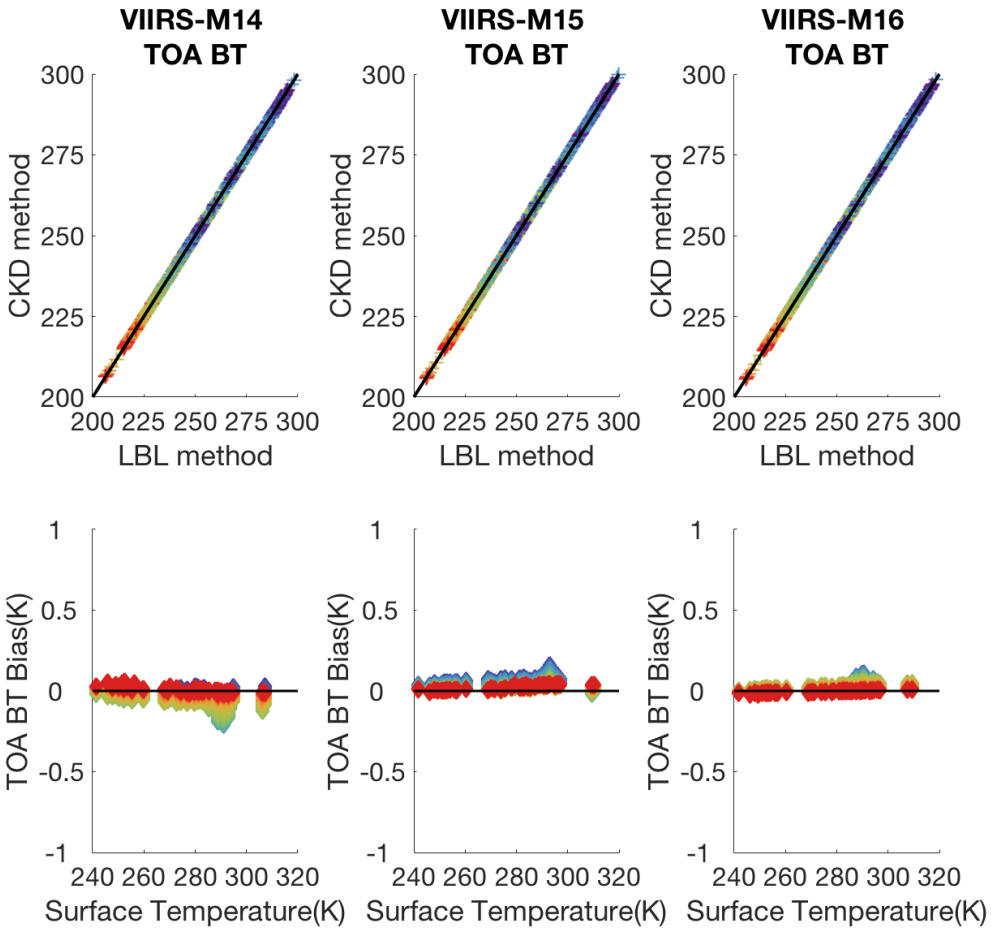

Figure 2.3 CKD models for VIIRS were validated using 42 typical profiles same as Figure 2.2. The upper panels show the TOA brightness temperatures between the rigorous LBLRTM +DISORT method results and fast CKD method results. The lower panels show the TOA brightness temperature differences between the LBLRTM results and CKD

method. Different colors refer to different sets of optical thickness and effective diameter pairs.

2.5. Comparison with VIIRS observations

VIIRS case study granule is selected over ocean to avoid land based biases. After looking at the GOES-West satellite IR imagery for clouds and convection, the frame of temporal reference was selected to be a nighttime granule on June 21, 2014. The exact temporal and spatial information for the areas being studied can be found in Figure 2.4.

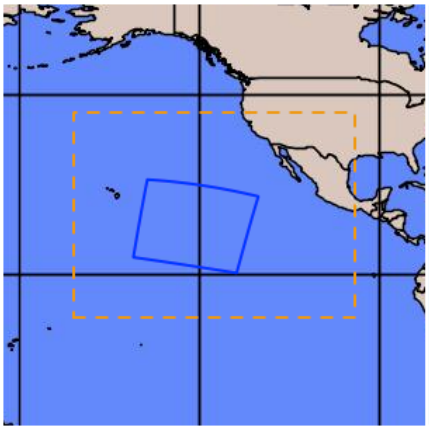

Temporal (Geographic Overlap):	
Start Date: 2014-06-21 10:38:57.000	**End Date:** 2014-06-21 10:44:37.000
Seconds: 340	**Direction:** Descending
Spatial (Geographic Overlap):	
1. NW Lat,Long: 23.76 , -147.78	**2. NE Lat,Long:** 19.54 , -120.03
3. SW Lat,Long: 4.29 , -151.28	**4. SE Lat,Long:** 0.37 , -125.45

Figure 2.4 Temporal and spatial information for granules (NOAA, cited 2016)

The Modern-Era Retrospective Analysis for Research and Applications (MERRA) is used to create atmospheric profiles as input for the RTMs. The grid is a reduced 1.25° x 1.25° horizontal spatial resolution with vertical pressure over 42 levels ranging from 1000 hPa to 0.1 hPa with data collected every three hours. The MERRA products used are air temperature, ozone mixing ratio, geopotential height, and specific humidity.

SNPP (Suomi National Polar-orbiting Partnership), the first mission for the Joint Polar Satellite System (JPSS), serves as the bridge between the old (i.e., Aqua and Terra) and new generations of NOAA and NASA satellite programs. VIIRS, onboard SNPP, is the largest instrument on SNPP and is categorized as a whiskbroom scanning radiometer that observes the Earth's surface in a cross-track direction

To make comparisons to observation, latitude, longitude, satellite viewing zenith angle, τ, D_e, and BTs are taken from VIIRS_SDR data sets, and COP and cloud top heights were collected from VIIRS_IPNG data sets. The data for surface temperature is taken from MERRA lowest layer air temperature. Fill values and NaN values are removed from the data sets so as not to cause erroneous results. Once the fill values are removed, the input can be used to simulate the BT values that VIIRS observed. Plots of the observed and simulated BT values are created for analysis. Comparing the simulated BTs to those observed by the VIIRS sensor provides a validation of the accuracy for the fast model. The comparison is shown in Figure 2.5.

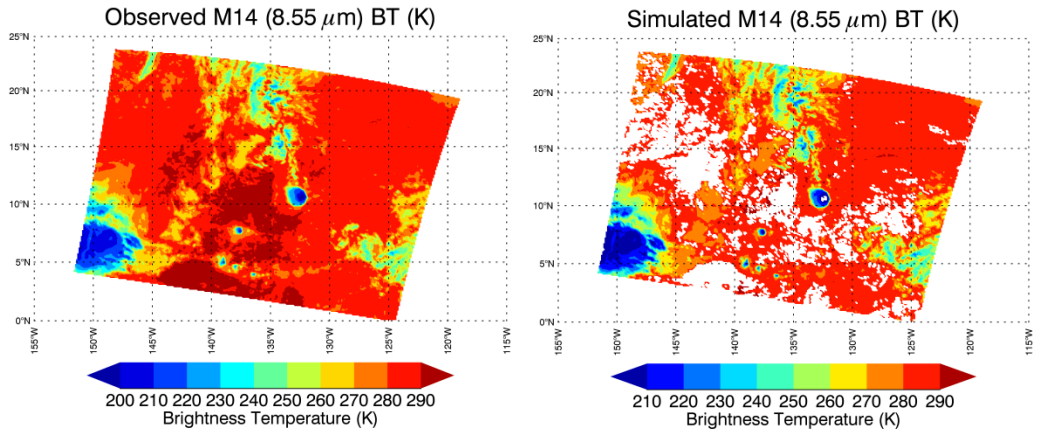

Figure 2.5 Comparison between observed (left) and simulated (right) brightness temperatures.

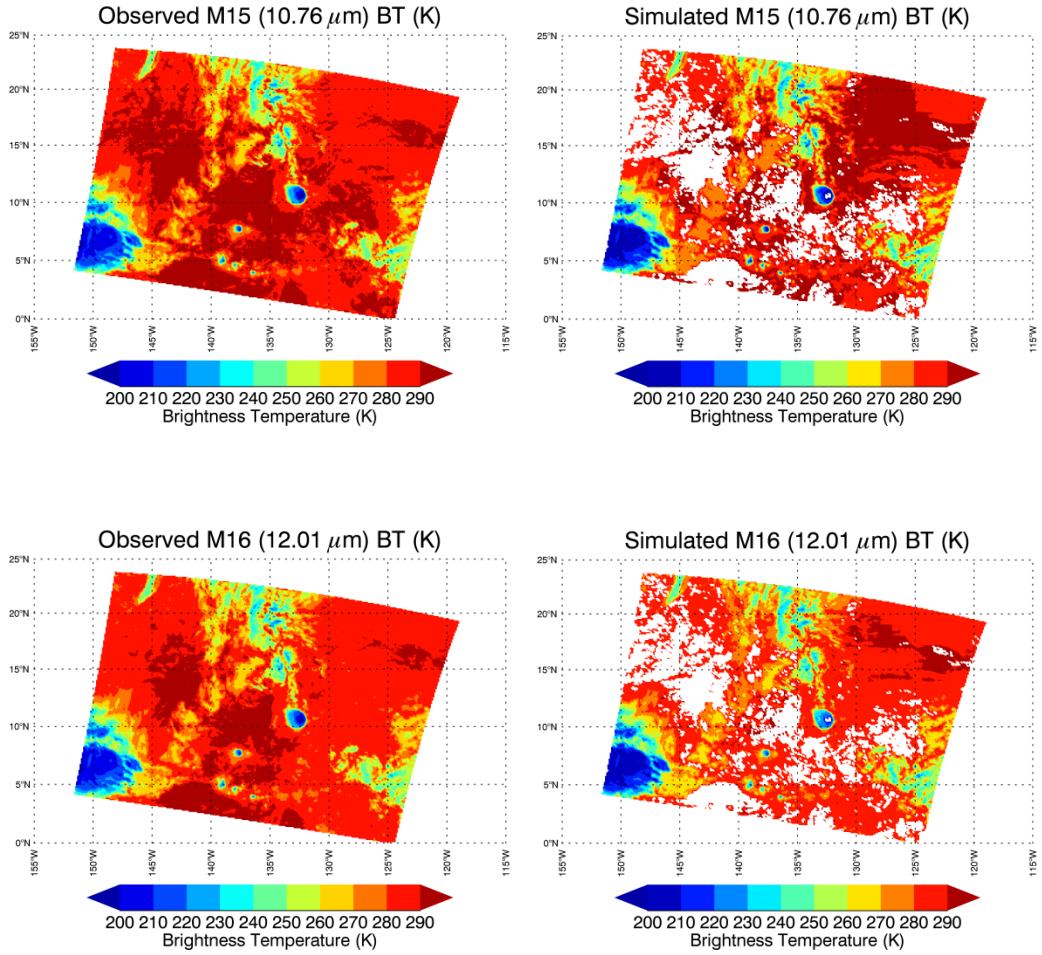

Figure 2.5 Continued.

The coldest values represent high cloud tops, where there may be thunderstorms or high cirrus clouds, and the warmest values represent lower cloud tops. The simulated BTs have good agreement with the observed BTs. The structure of storms is the same, and values are comparable. This result shows that not only is it possible to simulate BT at high resolutions on a large scale, but that the result is highly accurate. This could lead to strong improvements of global cloud retrieval and a better understanding of the effects of clouds

on the global energy budget as well as an improvement to their contribution in global climate models.

2.6. Conclusions

Clouds are an important part of the balance of the global energy budget. Cirrus clouds are not represented well within the breakdown of the global energy budget because so much is still unknown about their spatial and temporal distribution and their contribution of warming from the positive climate feedback. With a combination of remote sensing techniques and RTMs, BTs of clouds can be simulated, and cloud optical properties can be derived.

The rigorous LBLRTM + DISORT method simulation result is used to produce "benchmarks" to compare to those of the VFRTM to provide a measure of accuracy. Accuracy is well kept, which is proved by both idealized typical profile scenarios and real case study. Validation and case study show that error is a little higher for the clear sky cases than the cloudy sky cases. For the cloudy sky cases, error decreases when cloud optical thickness increases. BTD analysis is done for a pixel level comparison. This provides a test of accuracy at a much higher spatial resolution than MODIS products. All fill values from COP and BT data are removed prior to running the VFRTM. The results of the simulation are very good, showing high agreement between simulated and observed BT values. Overall, the VFRTM is found to be highly accurate and is validated for further use such as global cloud retrievals to help improve the global energy budget and global climate models.

3. SINGLE LAYER CLOUD PROPERTIES RETRIEVAL FROM VIIRS INFRARED MEASUREMENTS

3.1. Background

The intent of this study is to compare and assess three different methods to infer ice cloud optical thickness (τ) and effective diameter (D_e) from VIIRS solar and infrared (IR) measurements. Two of these methods are based on the statistical Bayesian and optimal estimation (OE) methods, developed specifically for use with the infrared (IR) window channels at 8.55 μm, 10.76 μm, and 12.01 μm, referred to as M14, M15, and M16, respectively. In general, the inference of τ and D_e from passive satellite-based imager measurements fall into the following categories: (1) infrared (IR) split-window methods using thermal IR bands (Inoue, 1985, Parol et al., 1991); (2) solar-reflection-based retrieval algorithms using a pair of visible and shortwave-infrared (VSWIR) wavelength channels (Nakajima and King, 1990); and (3) other IR-based methods (e.g., Minnis et al., 2011; Heidinger et al., 2015;). The bispectral solar-channel method uses VSWIR bands to simultaneously derive cloud optical and microphysical properties. One of the limitations of this approach is that, for optically thin ice clouds, large uncertainties may be introduced for several reasons: (a) the single-scattering properties depend on the overall particle habits (or shapes), surface texture (i.e., the degree of surface roughness), and other morphological characteristics (e.g., fractures, bubbles, scalloping, and impurities), (b) the bulk single-scattering properties require knowledge of the particle size distribution and the vertical structure of cloud microphysical properties (e.g., Stephens et al., 2002; Cooper et al., 2006; Garrett et al., 2009;), and (c) the sensitivity of the relevant radiative transfer

processes to surface temperature, spectral emissivity and albedo. Since consistent ice cloud properties are desired from the retrieval process regardless of solar illumination, increasing attention has been given to use of IR observations (e.g., Garrett et al., 2009, Heidinger et al., 2010, Holz et al., 2015). The theoretical basis of this method is that within the IR bands, the brightness temperatures (BTs) and brightness temperature differences (DBTs) between two wavelengths are primarily determined by both τ and D_e. Another benefit of IR measurements is that the higher amount of particle absorption, relative to the visible and SWIR wavelengths, decreases sensitivity to the degree of surface roughness as well as habit. However, the range of possible τ retrievals is more limited for IR measurements than for solar reflectance channels (Chiriaco et al., 2004).

The split-window method has been implemented to produce retrievals of thin ice cloud properties in operational products from the Visible Infrared Imaging Radiometer Suite (VIIRS) satellite sensor (JPSS, 2014a). However, the IR split-window method has its own inherent shortcomings as well. The top-of-atmosphere (TOA) BT depends on (a) the underlying surface temperature even if an optically thin cloud is present in the vertical column, (b) the cloud macrophysical properties (cloud top height/pressure/temperature, multiple-layer or single-layer cloud configuration), (c) the atmospheric profiles of temperature and humidity, and (d) atmospheric trace gas concentrations. These factors must be known *a priori* to successfully simulate the radiation field.

In this paper, VIIRS products used are from NOAA VIIRS Intermediate Products (IPs) (JPSS, 2014a; JPSS, 2014b). BTs in three VIIRS moderate resolution bands at 8.55, 10.76 and 12.01μm are used to derive τ and D_e based on the cloud mask and cloud top

heights, in addition to atmospheric profiles and surface temperatures from the Modern-Era Retrospective Analysis for Research and Applications (MERRA) dataset, which combines both numerical model results and observational data (Rienecker et al, 2011). The Bayesian and OE methods are applied using the same datasets and radiative transfer model. Retrievals are performed for ice cloud pixels meeting two requirements: (1) cloud top height greater than 6 km in the VIIRS IP cloud-top-property product (IVCTP) (JPSS, 2012), and (2) single-layer ice cloud in the VIIRS IP cloud-mask product (IVCMO) (JPSS, 2014a).

This chapter provides nighttime solutions to supplement the daytime-only retrieval product and subsequently investigates the advantages and disadvantages of three retrieval methods. Section 3.2 describes the basic forward model approach, section 3.3 discusses details of the retrieval methods, section 3.4 analyzes a case study including comparisons of the retrievals, and section 3.5 summarizes our findings.

3.2. VIIRS fast radiative transfer model (VFRTM)

The VIIRS Fast Radiative Transfer Model (VFRTM; Liu et al., 2015) is used to simulate the TOA (top of the atmosphere) IR radiances and brightness temperatures. The VFRTM assumes that clouds are plane-parallel, but can simulate both single- and multiple-layer clouds in a given column. VFRTM minimizes the computational burden with a channel-averaging technique (Liu et al., 2015) and computes the gas transmissivities using a correlated-k distribution technique (Fu and Liou, 1992). The ice cloud emissivity, transmissivity and reflectance functions are provided from pre-

calculated look-up tables (LUTs) that include these properties over a range of viewing angles, cloud heights, τ, and D_e values (Wang et al., 2011). Computations assume that the microphysical and optical properties of each pixel are homogeneous, while the cloud layer temperature decreases linearly with height. Rayleigh scattering is neglected at these IR wavelengths.

Figure 3.1 summarizes the methodology of the correlated-k distribution approach for computing background atmospheric gas transmissivities in VIIRS band M14 (8.55μm). The gas spectral absorption coefficients of a mixture of H_2O, N_2O, and O_3 are shown in Figure 3.1a, where the mixture mass density ratios of H_2O, O_3, and N_2O are 1:0.1:0.001, respectively. Subsequently, the absorption coefficient of the mixed gas is weighted by the M14 normalized spectral response function (SRF) in Figure 3.1b. Figure 3.1c presents the sorted effective absorption coefficient as a function of the cumulative probability function (g), which ranges from 0 to 1. In cumulative probability function (g) space, the band-averaged absorption coefficient becomes a smooth function instead of the previous serrated pattern, and can be approximated by 4 to 16 piecewise linear functions to obtain as much accuracy as the original serrated line with about 1000 or more coefficient values.

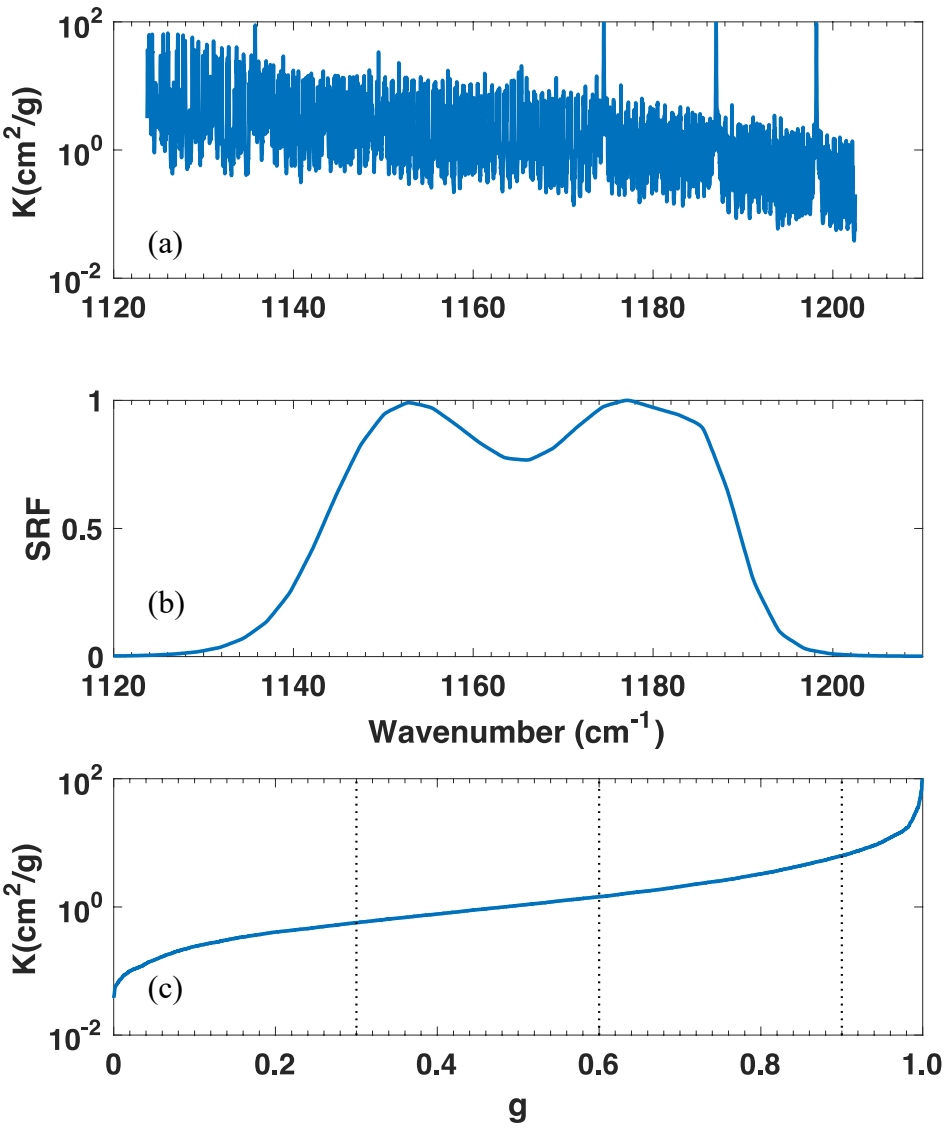

Figure 3.1 Example of the correlated-k process of mixed gas absorption lines for the VIIRS M14 (8.55μm) channel. (a) Absorption coefficient as a function of wavenumber (cm-1) for mixed gas of H2O, O3, and N2O with the ratio of the three gases being 1:0.1:0.001. (b) Spectral response function. (c) Absorption coefficient as a function of cumulative probability (g) for the mixed gas with the spectral response function.

This study uses the Moderate Resolution Imaging Spectroradiometer (MODIS) Collection 6 (MC06) ice cloud model (Platnick et al., 2017), which adopts a single ice habit consisting of an aggregate of 8 hexagonal columns with severely roughened surfaces. The MC06 ice particle habit was chosen because it minimizes the differences in the τ retrievals between those from CALIPSO and the IR split-window method (Baum et al., 2014; Holz et al. 2015). It should be noted that the linear polarization properties of this habit do not match well with those from POLDER/PARASOL (Baum et al. 2014), and further that the CALIPSO comparisons were limited to $\tau < 3$ (Holz et al. 2015). Note that throughout this study, all optical thicknesses are related to a visible wavelength of 0.65 μm.

The effective diameter (D_e) of an ice particle distribution is defined as follows:

$$D_e = \frac{3}{2}\frac{\sum_{i=1}^{N} V_i}{\sum_{i=1}^{N} A_i}, \tag{3.1}$$

where V_i and A_i are the volume and projected area of different sizes of particles over the particle size distribution. In this study, the particles are assumed to a gamma distribution with a relative standard deviation of 0.1.

Figure 3.2 is an example showing how the extinction efficiency, Q_e, varies with D_e in the M14, M15, and M16 VIIRS bands. The spectral average in any channel is obtained by weighting the SRF over the bandwidth. Generally, Q_e has the smallest values in VIIRS band M15 relative to the other two bands, and for M15 and M16, Q_e displays a monotonic relationship with D_e.

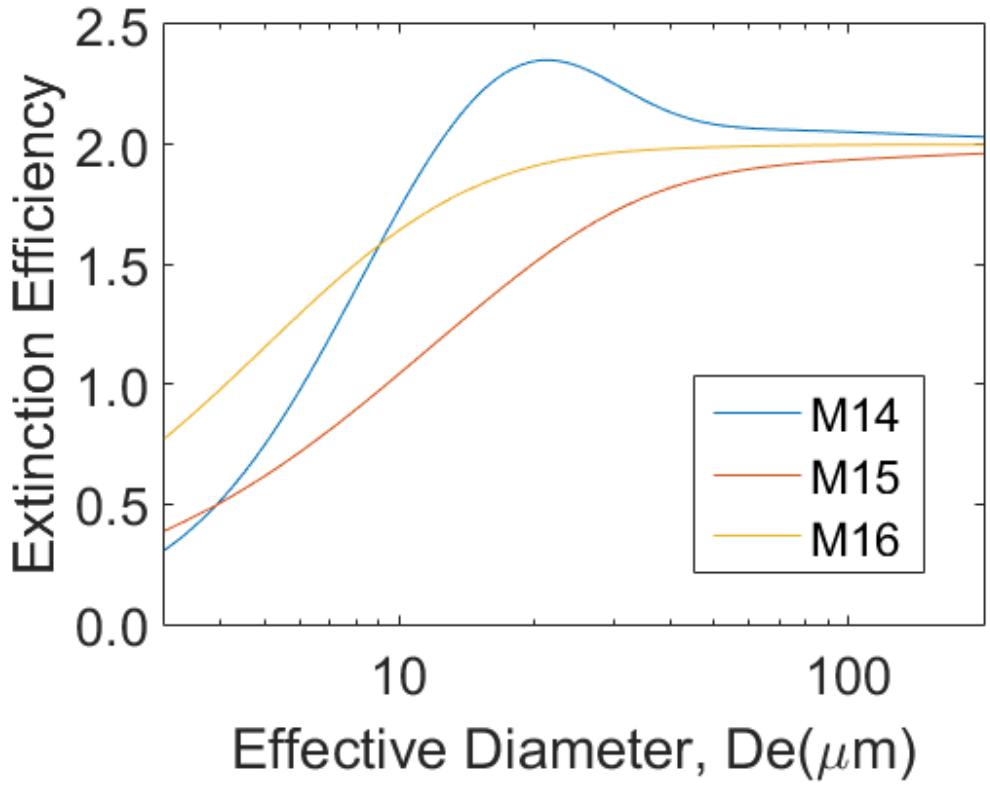

Figure 3.2 Extinction efficiency(Q_e) of ice particles as a function of effective particle diameter for VIIRS bands M14, M15, and M16 centered at 8.55, 10.56, and 12.01μm, respectively. Each effective diameter is computed as the average for a simulated cloud pixel with the stated mean effective particle diameter and a relative standard deviation of 0.1.

We now evaluate the feasibility of ice cloud retrievals of τ and D_e using the VFRTM through a sensitivity study based on a range of assumed ice cloud optical and microphysical properties. A U.S. standard atmosphere (Sissenwine et al., 1962) is assumed, with a surface and cloud-top temperature of 300 K and 240 K, respectively. The satellite viewing zenith angle is set to 10°, and the surface albedo is assumed to be 0.02 to represent

an ocean surface. Figure 3.3 shows simulated TOA BT and DBT values with changing τ and D_e pairs. Each of the five colored solid lines represents specific D_e value ranging from 10 µm to 100 µm. For each D_e, the optical thickness increases from 0 to 50. Figure 3.3 shows that TOA BTDs are highly sensitive to relatively small particle sizes (D_e <70µm) and over an optical thickness range from 0.2 to 6. In general, BTs vary from approximately 250K to 300 K when τ decreases from 6 to 0, whereas the DBT ranges are limited to only several K even when D_e changes from 10 µm to 100 µm, which is a more limited dynamic range. Therefore, the retrieved τ is more accurate than the retrieved D_e under these conditions.

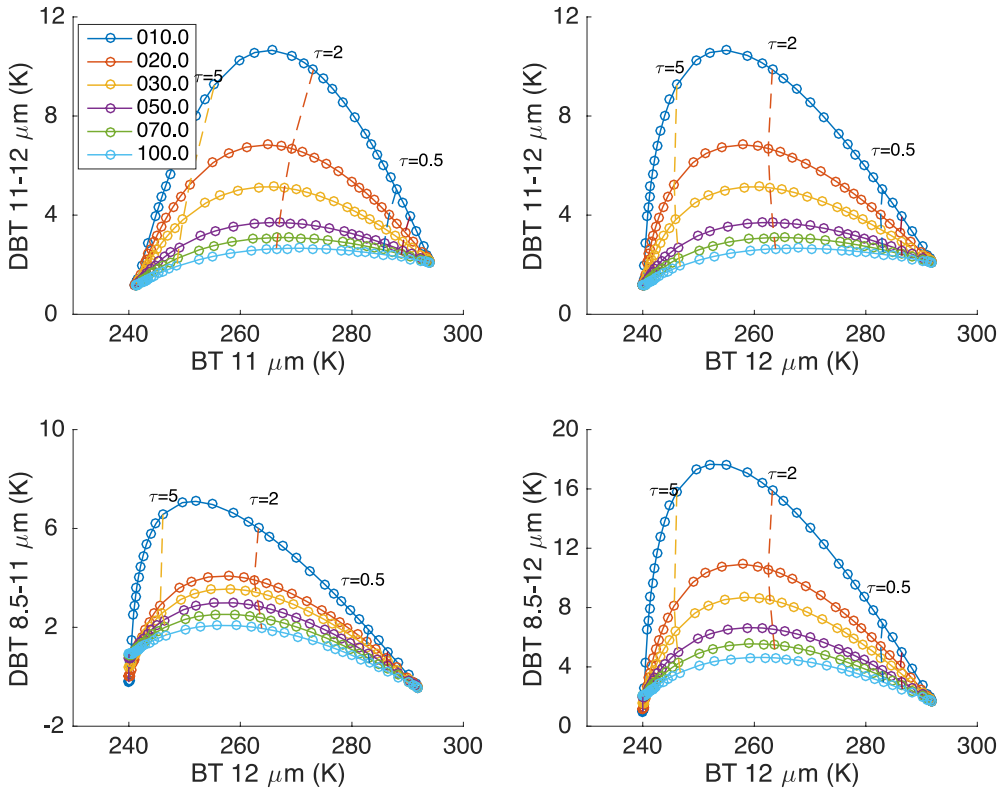

Figure 3.3 IR split-window brightness temperature differences, for an ice cloud which cloud-top temperature = 240K, surface temperature = 300K, view zenith = 10°, in the U.S. Standard atmosphere, unit of De (solid lines) is micrometer.

3.3. Retrieval methods

3.3.1. Bayesian retrieval algorithm

The Bayesian retrieval algorithm used in this study was designed originally to derive cloud ice water path (IWP) with the Submillimeter-Wave Cloud Ice Radiometer (SWCIR). This sensor was developed by the Jet Propulsion Laboratory (JPL) to fly on the NASA DC-8 aircraft (Evans et al., 2002). However, this algorithm can be used to derive the properties of interest to this study, i.e., τ and D_e. The Bayesian retrieval method uses a set of pre-determined τ and D_e pairs, and then computes the BTs in real-time for the relevant LUTs along with atmospheric profile and cloud geometric information. Finally, by integrating over the points in the LUT with Bayes theorem, cloud optical properties can be derived. Bayes theorem can be stated mathematically as follows:

$$p_{post}(x|\mathrm{T}) = \frac{p_f(\mathrm{T}|x)p_p(x)}{\int p_f(\mathrm{T}|x)p_p(x)\mathrm{d}x} \quad , \tag{3.2}$$

where x is the cloud property vector (here, the vector elements are pairs of τ and D_e used to simulate TOA BT); T is the vector of 3 TOA BT measurements in the VIIRS M14, M15, and M16 bands; $p_p(x)$ is the prior probability density function of cloud property x; $p_f(\mathrm{T}|x)$ is the conditional probability of BT given the cloud property vector x; and $p_{post}(x|\mathrm{T})$ is the posterior probability density function of the cloud property given the TOA BT measurements. The prior probability density function $p_p(x)$ is based on previous research of cirrus cloud property retrievals. The uncertainty of the cloud spatial and temporal distribution is normalized to 1.

The retrieved cloud property vector x_{ret} is calculated by integrating over the entire x space to find the weighted average value:

$$x_{ret} = \int x p_{post}(x|T) dx. \tag{3.3}$$

In practice, this integral process is replaced by summing over the defined x vector:

$$x_{ret} = \sum x_i p_{post}(x_i|T) \, . \tag{3.4}$$

The conditional probability density function $\mathrm{p}_f(\mathrm{T}|x)$ is the probability density of the TOA BT vector given defined cloud properties; i.e., the probability of a TOA BT measurement (T) given forward RTM simulations (R) of the atmospheric and cloud parameters. We assume a normal distribution function to represent the probability of each observed BT value:

$$p_f(T|x) = \prod_{j=1}^{M} \frac{1}{\sqrt{2\pi\sigma_j^2}} \exp\left(-\frac{\left(T_j - R_j(x)\right)^2}{2\sigma_j^2}\right) , \tag{3.5}$$

where T_j is the BT vector for band j (here, VIIRS band M14, M15, or M16); $R_j(x)$ is the VFRTM simulated result for band j; and σ_j is the standard deviation for band j. We assume that the uncertainty σ_j is due entirely to measurement errors. The measurement errors are assumed to be unbiased and the range of calibration errors is on the order of 0.3 K or less (Moeller et al., 2013). The measurement errors are assumed to be 0.3 K for all three bands and are independent of each other. Given this formulation, the conditional

distribution probability, $p(T|x)$, approaches zero when the BT vector value is far from the simulated values. Within the cloud property space, the Bayesian algorithm interpolates between the given points that agree approximately with the measurements. By combining (1) and (3), x_{ret} may be simplified to

$$x_{ret} = \frac{\sum x_i p_f(T|x_i)}{\sum p_f(T|x_i)} \ . \tag{3.6}$$

The x_i values are distributed according to the pre-determined τ and D_e provided in a LUT.

3.3.2. Optimal estimation (OE) algorithm

The OE method is an efficient inversion method (Rodgers, 2000; Iwabuchi et al., 2014) with the ultimate goal of deriving an optimized solution from observations given certain constraints. Similar to the Bayesian method, the TOA BTs for VIIRS channels M14, M15, and M16 are the input variables for retrievals of optical properties τ and D_e. The cloud property vector x, the measurement vector y, and the model parameter vector p are defined as follows:

$$x = [\tau, D_e] \tag{3.7a}$$

$$y = [T_{14}, T_{15}, T_{16}] \tag{3.7b}$$

$$p = [vzn, \epsilon, T_{surf}, H_{cloud}] \tag{3.7c}$$

The cloud property vector x is exactly the same as vector x in the Bayesian method; the measurement vector y corresponds to the vector T, which is renamed to be consistent with common statistics notation. The model parameter vector p includes the satellite viewing zenith angle (vzn), underlying surface emissivity (ϵ), surface temperature (T_{surf}) and cloud top height (H_{cloud}). The problem may be formulated in the form

$$y = F(x,p) + e\ , \tag{3.8}$$

where F is the forward radiative transfer model (RTM) and e is the system error from all sources, including measurements, forward RTM and model parameters.

The optimized solution is given by minimizing a cost function J:

$$J = [y - F(x,p)]^T S_y^{-1}[y - F(x,p)] + (x - x_a)^T S_a^{-1}(x - x_a)\ , \tag{3.9}$$

where x_a is the a priori vector, and S_a and S_y are the error covariance matrices of the a priori and the whole system, respectively. For cloud property retrievals, J is assumed to be dominated by the system error term since prior uncertainties may be very large. The goal is to minimize the S_y term. Minimization of this cost function is a nonlinear least squares fitting problem; the Levenberg-Marquardt iteration method (Levenberg, 1944; Marquardt, 1963) is chosen for use in this study. Our testing indicates that 6 iterations of the simulation results and the Jacobian matrices are sufficient to obtain convergence.

The system error S_y in Eq. (3.9) comes primarily from three different sources: the uncertainty in measurements, uncertainty in the forward RTM, and the uncertainty in model parameters. These three components are formulated as follows:

$$S_y = S_{y,m} + S_{y,fwd} + S_{y,p}\ . \tag{3.10}$$

The three terms $S_{y,m}$, $S_{y,fwd}$, and $S_{y,p}$ are the error covariances of the measurements, forward RTM, and model parameters, respectively. The range of calibration bias is assumed to be on the order of 0.3 K or less (Moeller et al., 2013), and as with the Bayesian formulation, the measurement errors are set to 0.3 K for all three bands and are assumed to be independent of each other. Gaussian distributed random noise is added to the model parameters.

Forward RTM and parameter errors ($S_{y,fwd}$ and $S_{y,p}$) are derived from a large number of VFRTM simulations in conjunction with the line-by-line radiative transfer model (LBLRTM) and the discrete ordinate radiative transfer model (DISORT) simulations for 42 typical atmospheric profiles, different τ and D_e pairs, and a range of viewing angles. From the simulations, the model parameter RMS error is within the range of 0.2 K to 0.9 K for both clear-sky and cloudy-sky scenarios that were derived assuming the U.S. standard atmospheric profile. The τ ranges from 0.01-20, and D_e ranges from 10-100μm. Generally, the RMS error decreases with increasing optical thickness and is not very sensitive to D_e. By comparing each contribution in Eq. (3.10), $S_{y,fwd}$ contributes the least to total S_y, while $S_{y,p}$ is the largest error component for all three VIIRS bands. Figure 3.4 shows the contribution proportion of the three different errors to the final S_y. Here, the measurement error diagonal matrices ($S_{y,m}$), indicating the covariance of the measuring error, is defined as follows:

$$S_{y,m} = \begin{bmatrix} \sigma_1^2 & 0 & 0 \\ 0 & \sigma_2^2 & 0 \\ 0 & 0 & \sigma_3^2 \end{bmatrix}, \tag{3.11}$$

where σ_j values are the standard deviations for the VIIRS bands. $S_{y,fwd}$ and $S_{y,p}$ are derived in the same way. Specifically, $S_{y,p}$ consists of four components: viewing zenith angle uncertainty, surface emissivity uncertainty, surface temperature uncertainty, and cloud position uncertainty:

$$S_{y,p} = S_{y,vzn} + S_{y,eps} + S_{y,ST} + S_{y,CH} \tag{3.12}$$

In Figure 3.4, the largest component is model parameter error for all the three bands, and the uncertainty of band M16 is the largest. $S_{y,fwd}$ is essentially negligible. The contributions from measurements and the forward RTM are relatively small compared with model parameters.

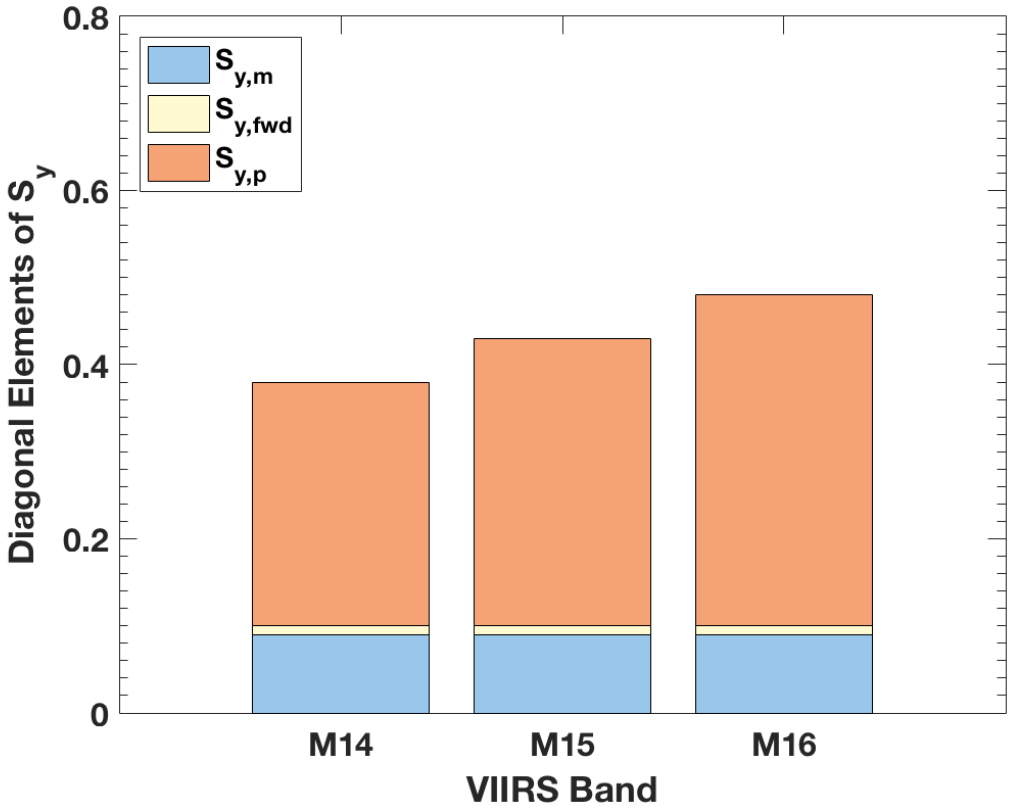

Figure 3.4 Fractions of the components of measurement-model errors in $\boldsymbol{S_y}$.

3.3.3. Control group method based on solar channel retrievals and IR algorithms

As stated before, the dual-channel method is one of the classic retrieval methods (Inoue, 1985; Nakajima and King, 1990; Liou et al, 1990). The JPSS approach uses

combinations of radiances of the VIIRS 3.7, 8.55, 10.76 and 12.01μm channels to infer cloud temperature and IR emissivity (JPSS, 2013b; JPSS, 2014b). Based on the cloud macrophysical properties, τ and D_e are inferred. The specific scheme used in the NOAA products depends on whether the target granule is considered day or night, and whether the pixel is of ice or liquid water phase. Here, VIIRS Cloud Optical Properties (IVCOP) is used as control group result.

3.4. Case study

A granule over the Pacific Ocean that consists of primarily ice clouds is chosen for detailed analysis (see Figure 3.5). Figure 3.6 shows the false color image of this granule composed of VIIRS bands M14 (8.55μm in red, component increases with decreasing signal), M16 (12.01μm in green, component increases with decreasing signal), and M14-M15 (8.55-μm BT minus10.76-μm BT in blue). Bright yellow pixels indicate regions completely covered by cirrus clouds. Greyish-green pixels show partial cirrus cover and dark pixels indicate little or no ice cloud. Figure 3.7 shows the cloud mask and cloud phase from the VIIRS IP dataset, IICMO, which shows that about one third of the granule is occupied by ice clouds.

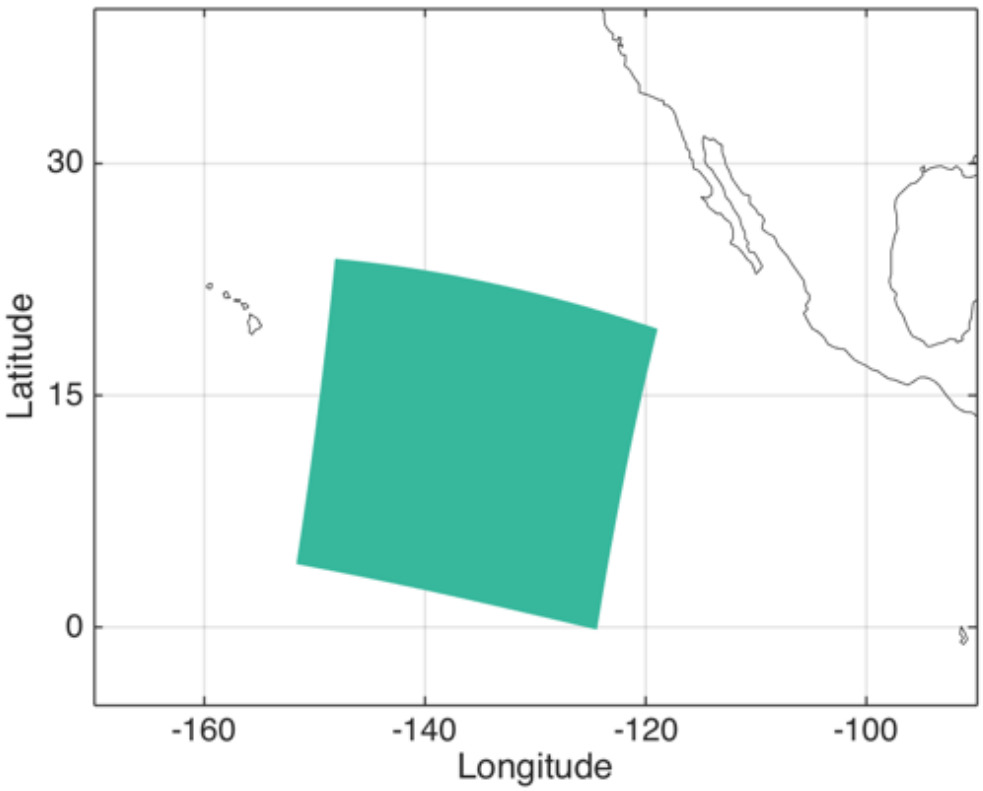

Figure 3.5 Case study granule geographic overlap.

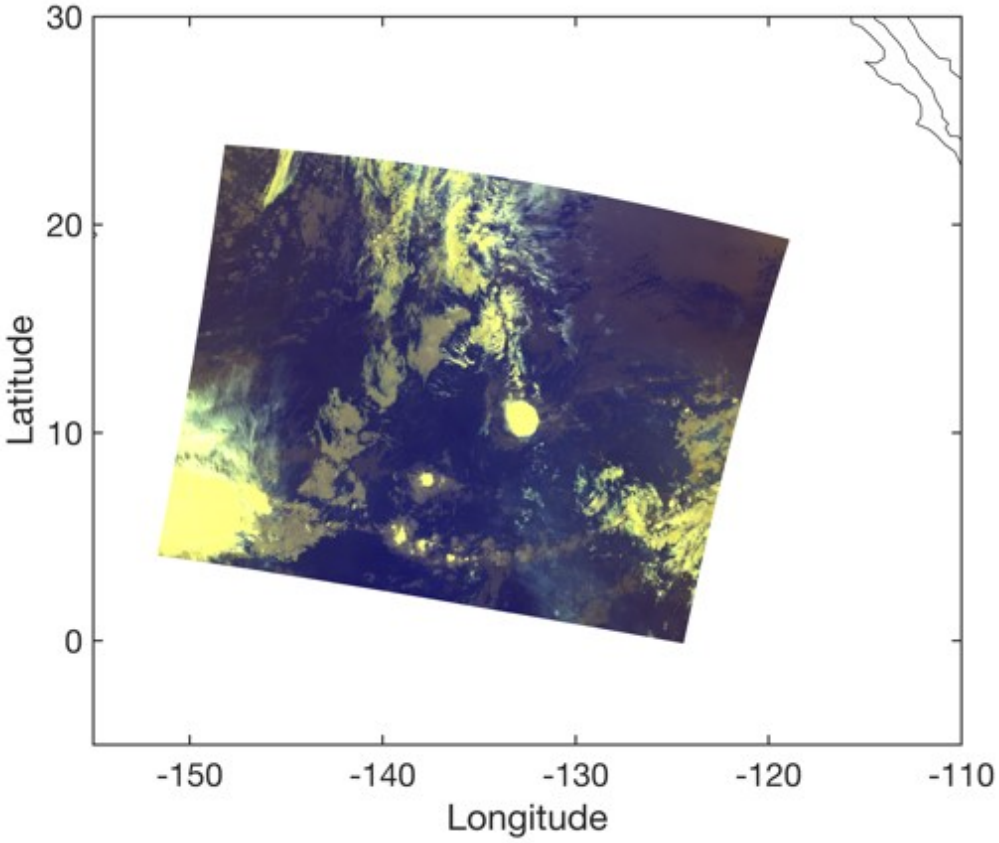

Figure 3.6 False color image composed of VIIRS bands M14 flipped brightness temperature (8.55μm in red, component increases with decreasing signal), M16 flipped brightness temperature (12.01μm in green, component increases with decreasing signal), and M14 minus M15(10.76μm) DBT (in blue).

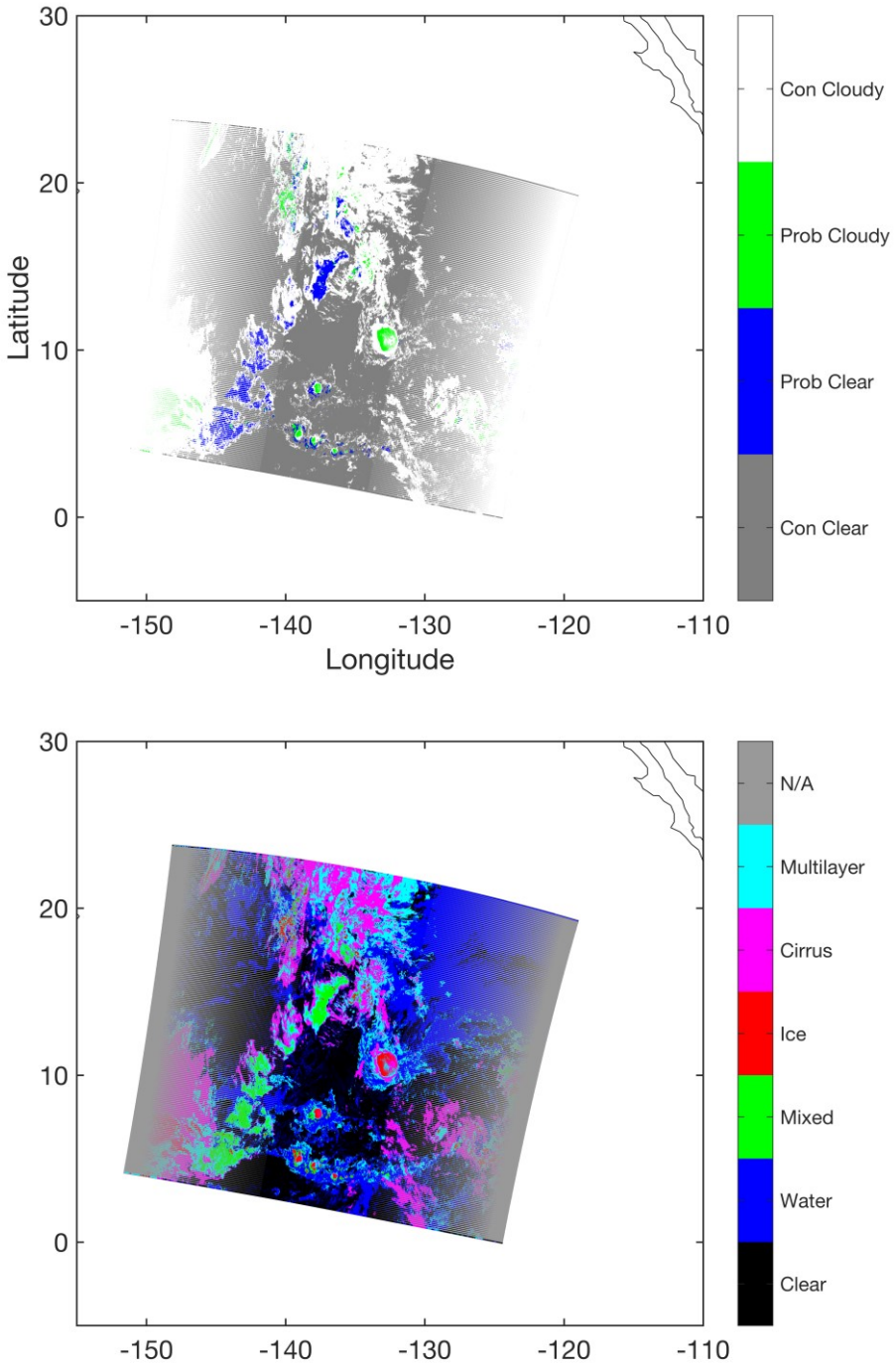

Figure 3.7 Cloud mask and cloud phase from the VIIRS IPs (IICMO). (top) Cloud mask. (bot) Cloud phase.

The VIIRS JPSS SDR products provide the level 1B data, including BTs in bands M14, M15, and M16 (JPSS, 2013a). Table 3.1 shows the location of the granule. The VIIRS datasets also provide TOA brightness temperatures, cloud mask, and other pertinent information such as the viewing geometry. Cloud top temperatures and heights at a horizontal resolution of 750m are obtained from the VIIRS IP dataset (IVCTP). As noted earlier, the NOAA cloud products in the control group are available for comparison.

Table 3.1 Case study granule geographic information

Temporal(Geographic Overlap)	
Start Date: 2014-06-21 10:38:57	End Date: 2014-06-21 10:44:37
Seconds: 340	Direction: Descending
Spatial(Geographic Overlap)	
Lower-left: 4.10, -151.64	Upper-right: 19.30, -118.93

Based on the OE method (Section 3.3.2), cloud top heights are inferred for the ice phase pixels and are assumed to be plane-parallel so that the VFRTM can be used to simulate the cloudy radiances. MERRA data provide atmospheric profiles and surface temperatures at a spatial resolution of 1.25°, and temporal resolution of 3 hours. The sea surface temperature is derived from the MERRA surface air temperature using a linear interpolation technique. The IR sea surface emissivity is assumed to be constant at 0.02

over the ocean. The ice cloud properties are retrieved for all pixels deemed to be ice according to the VIIRS cloud phase. Any pixel with a missing value in measurement is discarded. A pixel is accepted for further analysis if it then satisfies the following three conditions: (1) cloud top height higher than 6 km in the VIIRS IP dataset, IVCOP; (2) single-layer cloud pixel determined in VIIRS IP dataset, IVCMO; (3) DBT for (M14 minus M16) greater than 0.5K.

The control group cloud optical thickness and effective size are shown in Figure 8 for comparison. Inspection of Figure 3.8 indicates that optically thin ice clouds are widely distributed over the granule. The results obtained with the Bayesian method (Section 3.3.1) and OE method (Section 3.3.2) are shown in Figure 3.9. Based on the results in Figs. 3.8 and 3.9, it may be seen that all three methods are able to infer cloud properties for optically thin clouds, i.e. τ<1.0. Some minor differences may be due to the presence of mixed-phase or multi-layer clouds.

Figure 3.10 shows comparisons of control group simulations with the Bayesian and OE retrieval results and observed VIIRS M14 (8.55μm) BTs. The simulated and retrieved BTs closely agree. Moreover, Figure 3.10 shows that, apart from the convective area, the brightness temperature differences between reproduced BTs and observations are slightly different, with the values generally less than 0.5K. Channels M15(10.76) and M16(12.01μm) show similar or even better performance than the M14 channel. These results demonstrate the consistency of the retrievals.

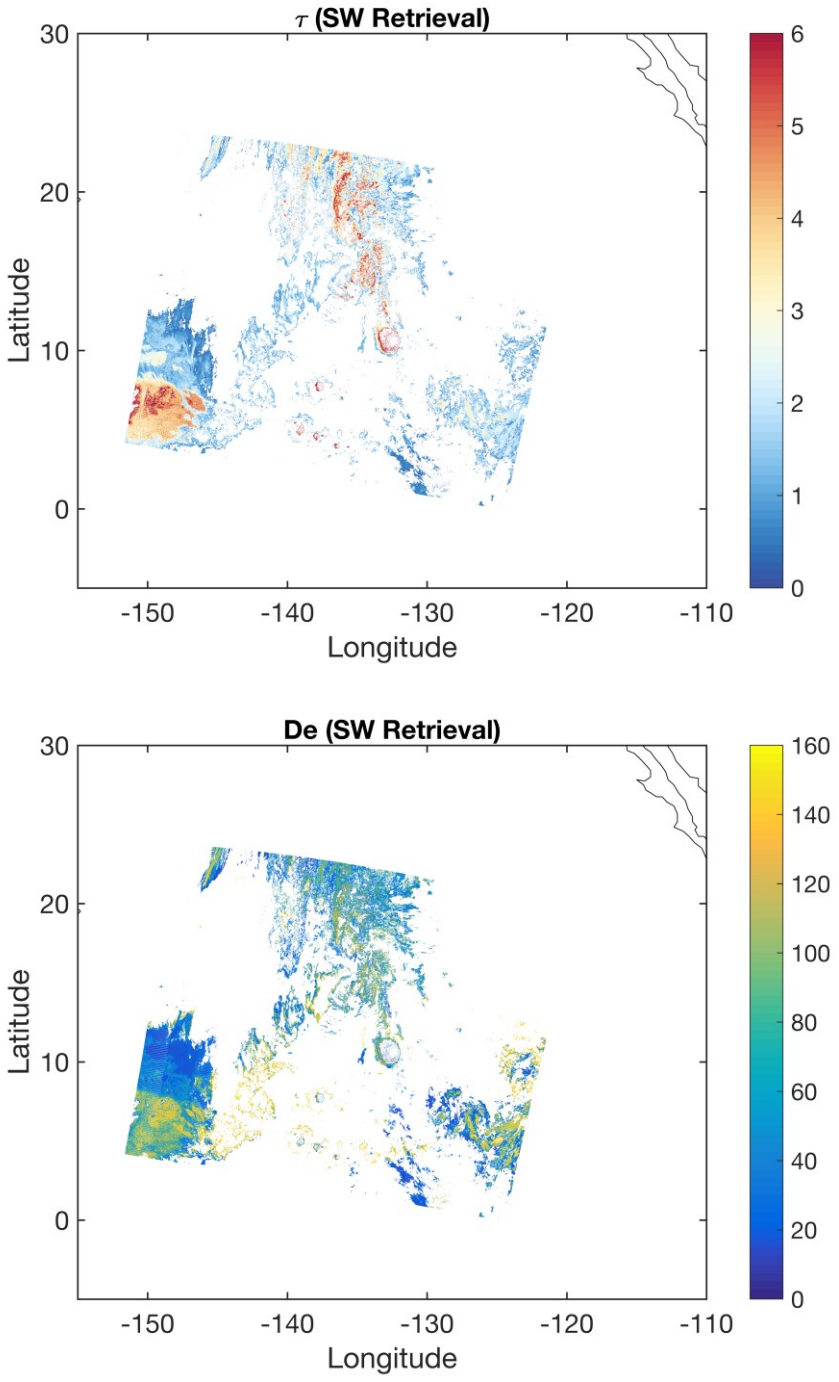

Figure 3.8 Control group retrieved (top) cloud optical thickness (τ) and (bot) effective particle diameter (D_e).

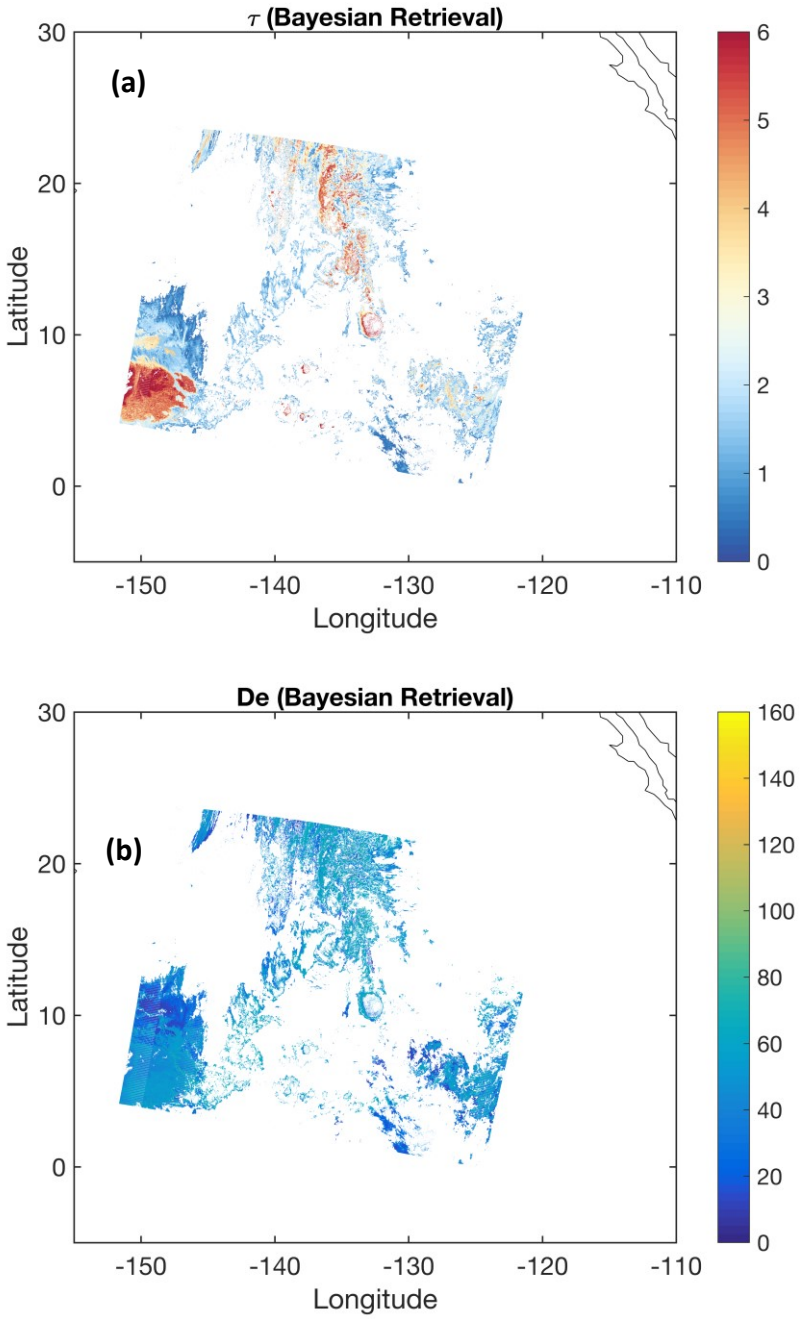

Figure 3.9 Retrievals performed with (a,b) the Bayesian method and (c,d) the OE method (a,c) cloud optical thickness (**τ**) and (b,d) effective particle diameter (D_e), respectively.

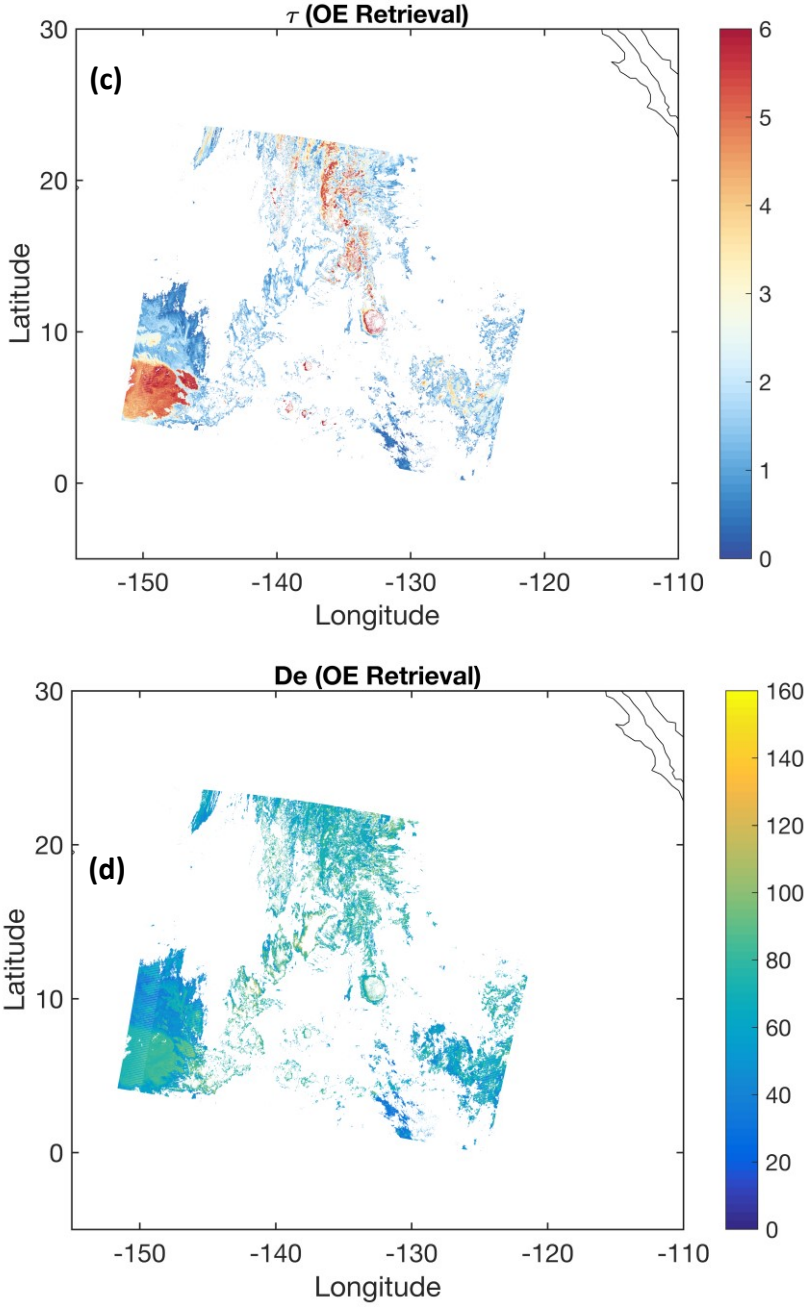

Figure 3.9 Continued.

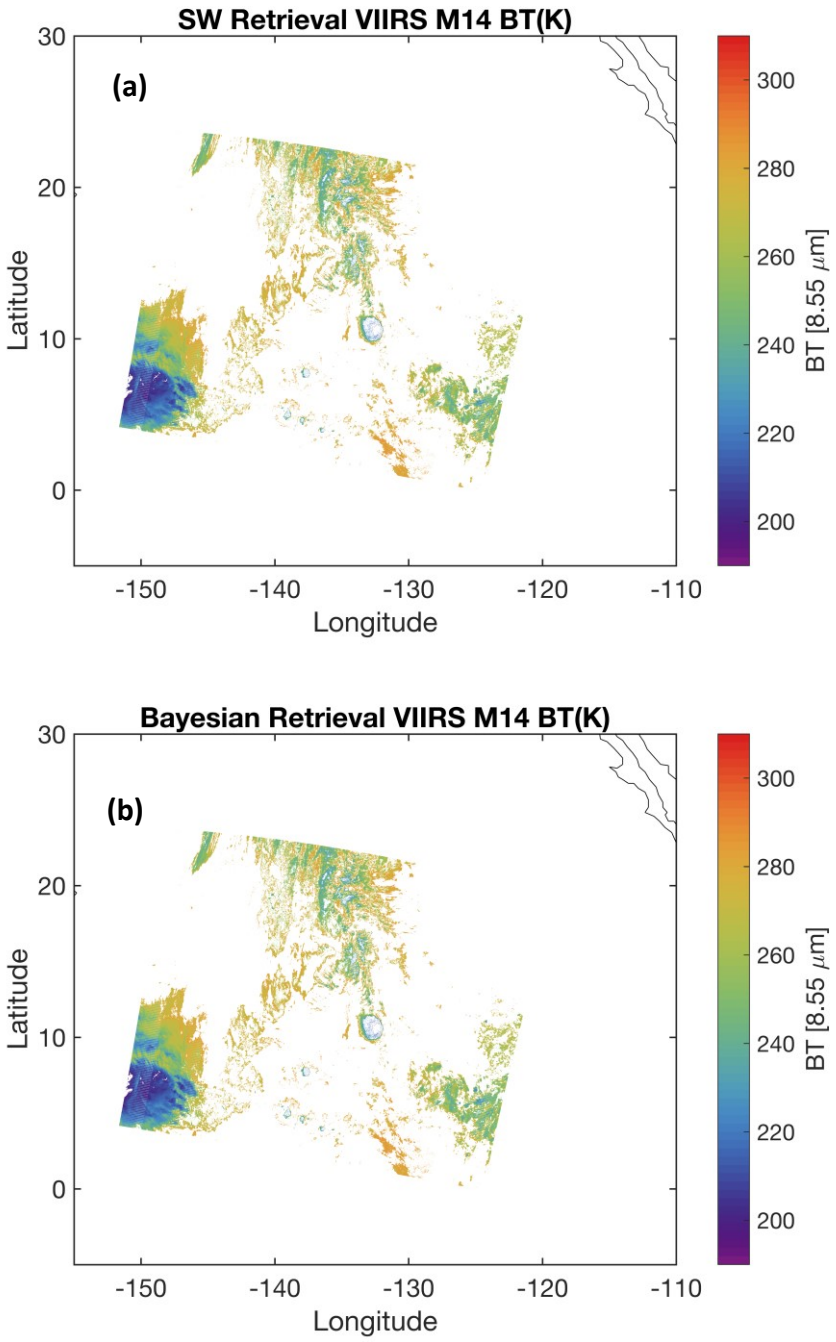

Figure 3.10 Comparison between the (d) observed and (a-c) simulated brightness temperatures at the VIIRS M14 (8.55μm) channel. (a) Control group; (b) Bayesian method; (c) OE method.

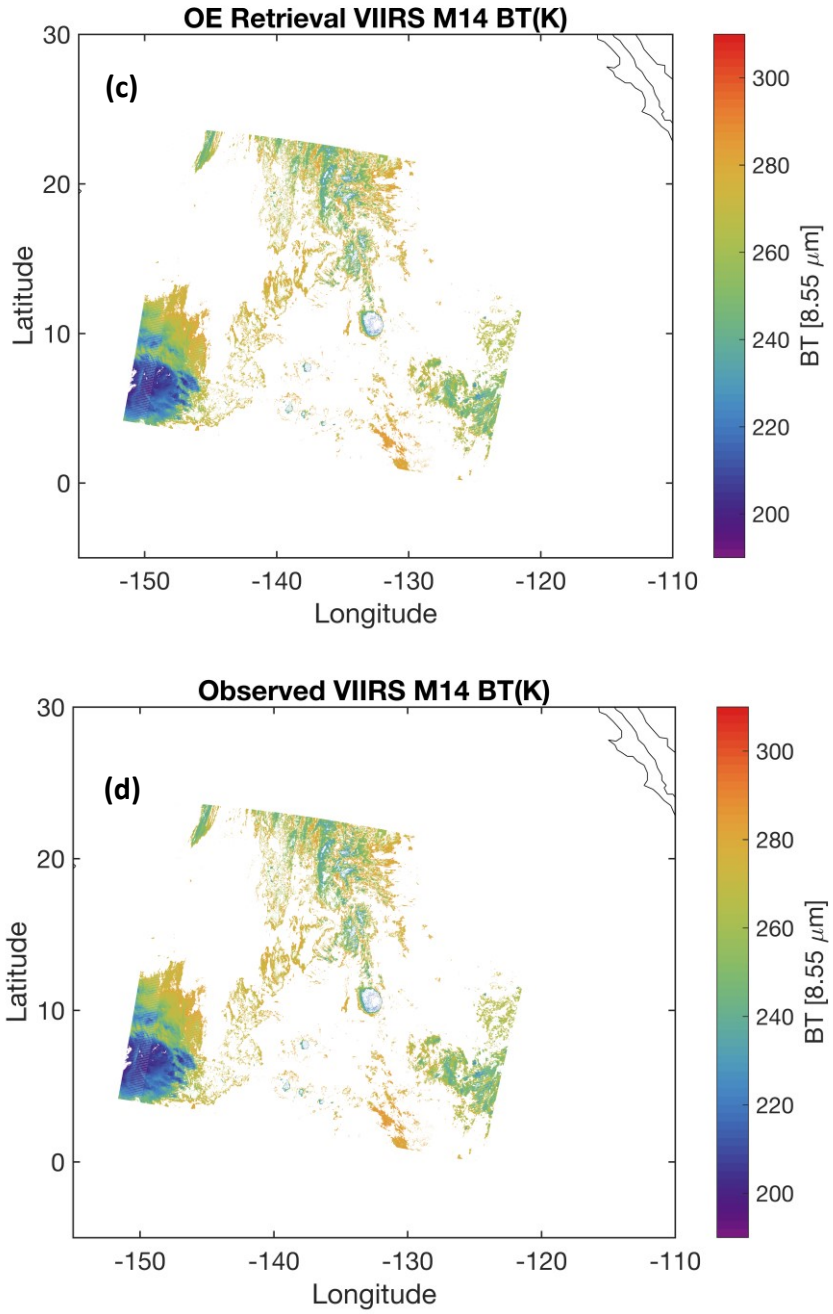

Figure 3.10 Continued.

A more quantitative evaluation of the pixel level cloud property comparisons is shown in Figure 3.11, which shows joint histograms of the control group retrieval (VSWIR) with the Bayesian or OE retrievals for the ice cloud pixels with $\tau < 4$. The derived τ has a correlation coefficient of 0.94 for the Bayesian method and 0.92 for the OE method. For the D_e retrieval, the correlation between each test group and the control group is much weaker, with correlation coefficients of 0.64 for the Bayesian method and 0.32 for the OE method. To better understand the retrieved D_e distribution, probability density functions, or PDFs, of D_e are shown in Figure 3.12. The figure indicates that the OE method infers larger values of D_e than those from the Bayesian method. The Bayesian method De distribution is highly concentrated around 50μm, while the OE distribution of D_e has a larger variation. Neither method closely matches the control group D_e distribution. The error source associated with the OE method leads to potentially large uncertainties into the retrieval. Moreover, the Bayesian method deals with only measurement error, while the OE method incorporates a more comprehensive consideration of error sources, including RTM and model parameter errors. As a result, the OE method does not perform as well as the Bayesian method. When we eliminate the effects of the two additional error sources from the OE method, retrieval results similar to the Bayesian counterparts can be derived as shown in Figure 3.13.

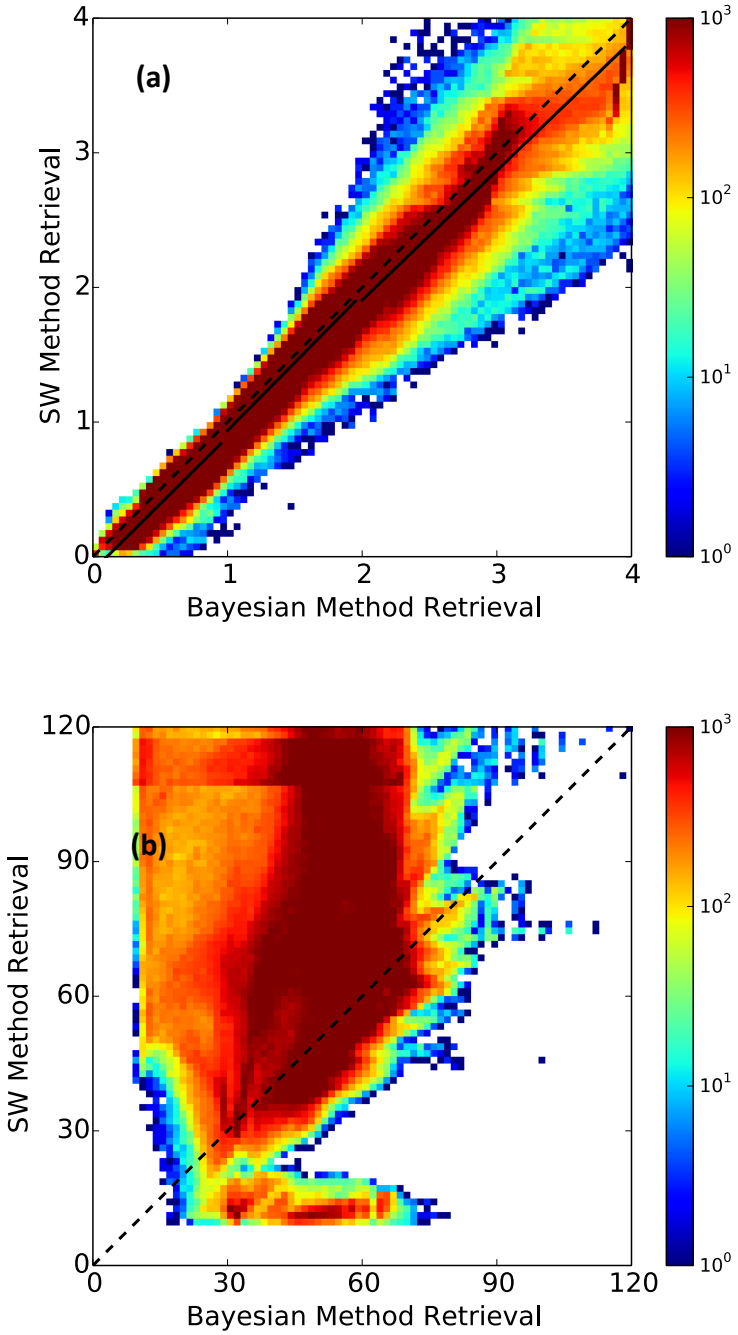

Figure 3.11 Joint histograms of the control group and test groups retrievals for the case: (a, c) optical thickness, (b,d) cloud particle effective diameter.

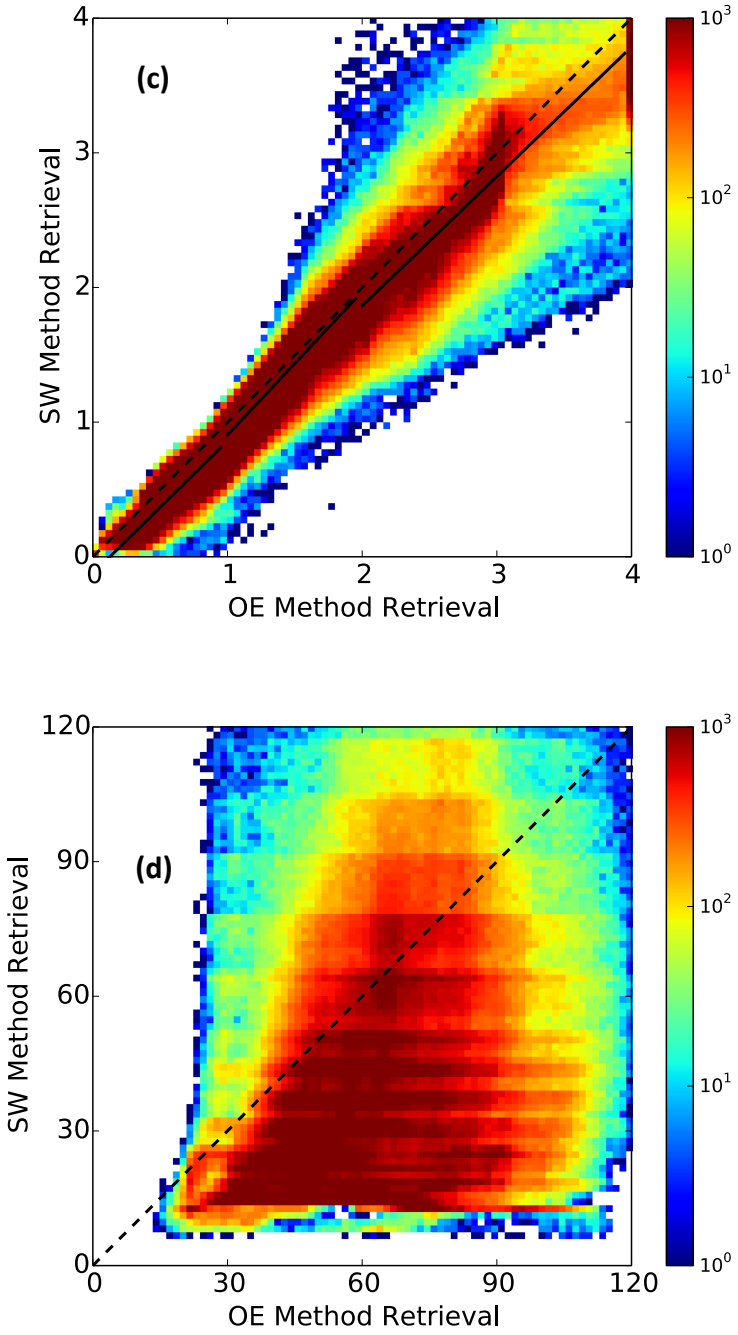

Figure 3.11 Continued.

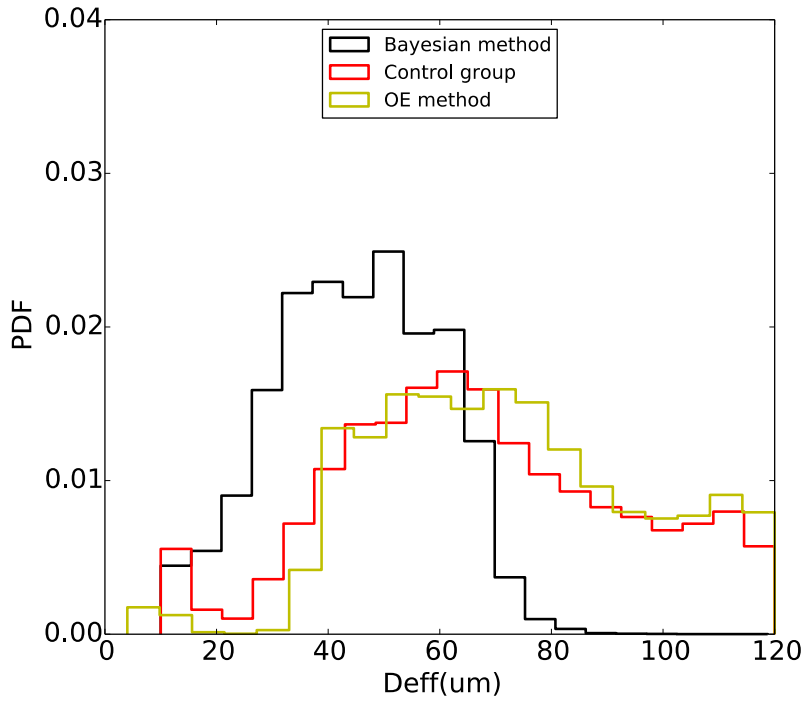

Figure 3.12 Probability distribution function of the control group (red) and test groups retrievals for the case: (black) Bayesian method, (yellow) OE method.

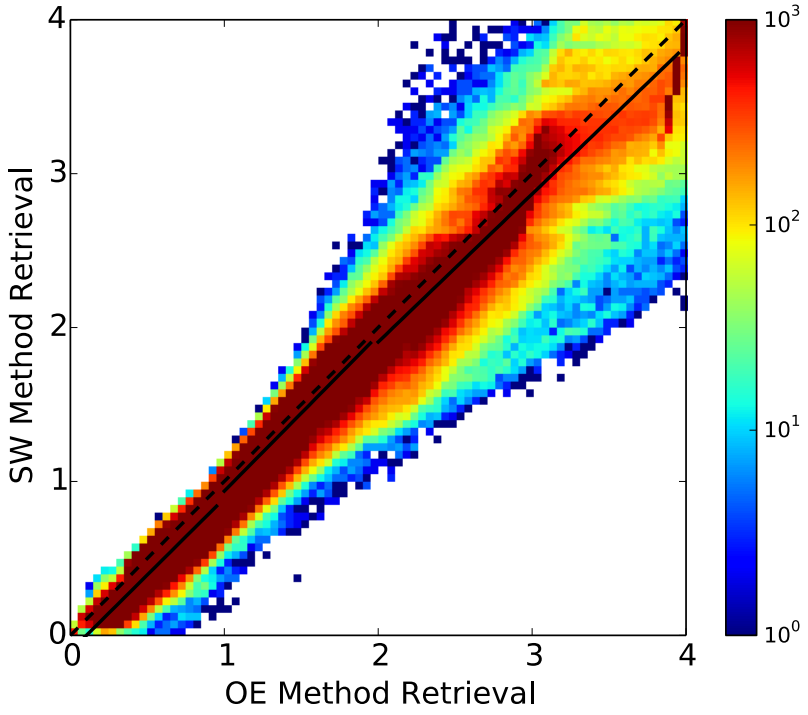

Figure 3.13 Joint histograms of the control group and OE method retrievals for optical thickness with measurement error only.

3.5. Conclusions

A Bayesian method and an OE method based on VIIRS IR bands (M14, M15, and M16, or 8.55 μm, 10.76 μm, and 12.01 μm, respectively) are compared to the classic solar wavelength bispectral method to derive the optical and microphysical properties of optically thin ice cloud (optical thickness, τ, and ice particle effective diameter, D_e). Prior conditions about cloud height, atmospheric profile and underlying surface temperatures are provided by ancillary data sources, including VIIRS IP datasets and MERRA. The ice cloud scattering properties used in this study are based on the severely roughened aggregate of solid columns ice particle, the same as that adopted for the MODIS Collection 6 ice cloud product (Platnick et al., 2017). The VIIRS Fast Radiative Transfer Model (VFRTM) is uses a correlated-k distribution method for atmospheric absorption and a pre-calculated LUT of the ice cloud transmission and scattering properties as a function of optical thickness, cloud height, and effective particle size.

The VFRTM error contributes very little to the final uncertainty. The uncertainty of the model parameters (including errors in cloud top height, surface emissivity, and temperature) has the greatest contribution to cloud property retrieval errors. Among those factors, we find that the accuracy of the cloud height and the underlying surface temperature heavily influences the associated error in the retrieval of τ and D_e. Generally, τ retrievals have a much higher correlation with the control group retrieval, while much lower correlations are found with D_e retrievals.

Our conclusions are as follows. First, both the OE and Bayesian methods are useful for inferring cloud optical thickness based on split-window IR measurements. We note

that the Bayesian method is approximately two times more efficient computationally than the OE method retrieval. An advantage of the OE method is that it provides more information useful for quality control because it produces several diagnostics related to retrieval quality (Iwabuchi et al., 2014). The Bayesian and OE methods have a significant advantage relative to the bispectral VSWIR LUT method that they can potentially be adapted to higher degrees of freedom, specifically, inadequate model assumption scenarios such as multilayer clouds or water-phase clouds. A subsequent paper will present a multilayer cloud derivation using the Bayesian and OE retrieval methods using multiband IR observations.

4. MULTI-LAYER CLOUD PROPERTIES RETRIEVAL FROM VIIRS INFRARED MEASUREMENTS

4.1. Background

Clouds are of significant effects on global climate patterns as a result of a complicated interaction with solar and terrestrial radiation process (Herman, et al., 1980; Hartmann and Short, 1980) (Poore et al., 1995). Horizontally and vertically homogeneous cloud system, i.e. single-layer cloud system, is the most idealized model in radiative transfer simulation. Derivation of cloud properties is compromised when multi-layer clouds are presenting but single-layer clouds are assumed. For these compromised retrievals, i.e. treated as single-layer clouds, however, actually are multi-layer ones, the results usually lie between the layer properties: cloud heights lie lower than the upper layer and higher than the lower one; effective particle sizes are between water cloud droplets and ice cloud particles as well (Davis et al., 2009). Inferences from global water vapor profile data suggest that 40% of all global cloud systems involve multi-layer clouds (Poore et al., 1995; Wang et al., 2000). Considering the widely occurrences of multi-layer scenarios, it is of importance to derive an accurate representation of these clouds with the help of satellite-based observations.

Detection and microphysical property retrieval are two respects of remote sensing of multi-layer clouds. Much work has been conducted on cloud detection. By calculating differences or ratios of visible, near-infrared(NIR), and thermal infrared (IR), characteristic signals can be isolated to detect the presence of multi-layer or multi-phase clouds (Nasiri and Baum, 2004; Joiner et al., 2010; Wind et al., 2010). With the help of

the absorption characteristics of 0.94μm atmospheric water vapor channel, which is very sensitive to upper layers of cloud, along with CO_2 bands, it is possible to derive two above-cloud precipitable water retrievals, the difference of which, in conjunction with additional tests, provides a map of where multilayered clouds might potentially exist (Wind et al., 2010). Moderate Resolution Imaging Spectroradiometer (MODIS) bands, 1.38- and 1.65-μm near-infrared bands, can also be used to detect overlapped cloud systems (Pavolonis and Heidinger, 2004). Both of aforementioned algorithms can be applied at pixel level. Some other methods based on statistics theory require clear-sky or single-layer cloud measurement accessible as auxiliary quantities (Nasiri and Baum, 2004). The retrieval of multi-layer cloud properties is not axiomatic, even for confirmed multi-layer scenarios, because multi-layer cloud properties are greatly dependent on the relative characteristics of the layers. A thick upper layer will tend to cover the signal from a lower layer. Therefore, the main objective of current algorithms is to detect multilayered cloud scenes that are optically thin ice cloud overlying a lower-level water cloud. Meanwhile, errors that retrieval results turn out to be abnormally large water droplets also arise if it fails to detect multilayer cloud when upper cloud is too thin to dominate the upwelling radiance (Wind et al., 2010). In terms of mentioned earlier, cloud detection is of great importance in remote sensing of multi-layer clouds.

Cloud detection has attracted much attention as described above. In this paper, I will focus on multi-layer cloud microphysical property retrieval, especially two-layer cloud cases. It is based on an optimal estimation (OE) method and a Bayesian method. In principle, I will apply near-infrared and thermal infrared measurements, i.e. M13

(4.05μm), M14(8.55μm), M15 (10.76μm) and M16 (12.01μm) bands, from Visible Infrared Imaging Radiometer Suite (VIIRS) into aforementioned retrieval algorithms. Cloud essential microphysical properties, cloud optical thickness (τ) and effective particle diameter (D_e), will be derived simultaneously. The OE method output, let alone cloud properties mentioned before, is the cost function *J*, a measure of to what degree the retrieval results fit to the actual observations. Just like the discussion in my previous paper (Ding et al, 2017), both OE method and Bayesian method could be applied to single-layer cloud retrieval. The main difference between single-layer cloud retrieval and multi-layer cloud one is that homogeneous single-layer clouds, generally, has lower uncertainty in property retrieval, while multi-layer clouds trend to have higher uncertainty, i.e. greater *J* value for OE method.

As we known that, errors from model parameter have a great effect on the retrieval (Ding et al, 2017). It is important to ensure the accuracy of model parameter vector *p*, including the satellite viewing zenith angle(vzn), underlying surface emissivity(ϵ), surface temperature(T_{surf}), cloud top height(H_{cloud}), and atmospheric profiles. We use the measurements from VIIRS moderate resolution bands as inversion basis. The Cloud–Aerosol Lidar and Infrared Path- finder Satellite Observation (CALIPSO) satellite equipped with the Cloud–Aerosol Lidar with Orthogonal Polarization (CALIOP) provides H_{cloud}. The Modern-Era Retrospective Analysis for Research and Applications (MERRA) data are used for atmospheric profiles. The interested pixels are limited to the CALIOP–VIIRS collocated pixels. In order to better simulating the surface emission, instead of constant surface emissivity for all bands, we use the Fresnel reflectance to derive the ocean

surface emissivity, which is based on the assumption that the ocean water refractive indices are dependent on sea surface temperature (Newman et al., 2005).

This study provides infrared band measurements based solutions to investigates the advantages and disadvantages of two retrieval methods, OE method and Bayesian method. The optical thickness and effective particle diameters are retrieved from the brightness temperatures in VIIRS IR bands at center wavelengths of 3.70, 4.05, 8.55, 10.76, and 12.01μm. Because the resolution of VIIRS moderate band measurements is 750 m by 750 m, it is required to make the retrieval algorithm efficient enough to rapidly process data with acceptable, well-quantified uncertainties.

This chapter is organized as following sections. Section 4.2 describes the basic forward model approach and improvement compared with previous paper, section 4.3 discusses theoretical basis and details of the retrieval methods, section 4.4 is a sensitivity study based on synthetic measurements simulated with specified perturbed model parameters, section 4.5 evaluates the pixel level retrieval results by comparing with collocated CALIPSO retrievals, and section 4.6 summarizes our findings.

4.2. VIIRS fast radiative transfer model (VFRTM)

As my previous chapter mentioned, VFRTM is a one dimensional, single-/multi- layer cloud supported Radiative Transfer Model (RTM) specialized for simulating VIIRS observations. Channel-averaged technique is implemented in the model to minimize the computational burden. Besides, the correlated-k distribution (CKD) technique (Fu and Liou, 1992) is adopted to compute the background atmospheric gases transmissivities; The

microphysical and optical property of the whole cloud layer has assumed to be homogeneous, while the cloud layer temperature decreases linearly with height. And the Rayleigh scattering is neglected at these IR wavelengths.

The Moderate Resolution Imaging Spectro-radiometer(MODIS) Collection 6 (MC06) ice cloud products (Platnick et al., 2017) are used as the ice particle model, which adopts a single ice habit consisting of an aggregate of 8 hexagonal columns with severely roughened surfaces. The MC6 ice particle habit was chosen because it minimizes the differences in the τ retrievals between those from CALIPSO and the IR split-window method (Baum et al., 2014; Holz et al. 2015). Note that throughout this study, all optical thicknesses are related to a visible wavelength of 0.65 μm. The effective diameter (D_e) of an ice particle distribution is defined as follows:

$$D_e = \frac{3}{2}\frac{\sum_{i=1}^{N} V_i}{\sum_{i=1}^{N} A_i}, \tag{4.1}$$

where V_i and A_i are the volume and projected area of different sizes of particles over the particle size distribution.

Liquid water droplet model adopts water sphere with refractive index follows Segelstein, D., 1981 (Segelstein, 1981). In this study, both liquid water and ice particles are assumed to a gamma distribution with a relative standard deviation of 0.1. Figure 4.1 and Figure 4.2 are showing ice cloud particle and liquid water droplet single scattering properties. Figure 4.1 shows the extinction efficiency of cloud partcles vary with particle effective diameters. We can see that, generally, ice cloud extinction efficiency(Q_e) is lowest at VIIRS band M15 and almost unaffected with size changes, while water cloud Q_e

in M15 band changes a lot depending on the effective diameter and has good relevance to particle size. And, according to Figure 4.2, for both ice and liquid clouds, single-scattering albedo is relatively high at band M13 compared with other three bands at the small size area, which reveals that scattering is of importance at mid-wavelength infrared (MWIR). The same for M14 band at middle size region.

In order to better simulate the process of underlying surface, we use temperature-dependent sea surface albedo instead of constant surface albedo (Newman et al., 2005; Ding et al., 2017). In this way, the sea surface albedo is calculated from the Fresnel reflectance of a flat ocean surface, assuming that the seawater refractive index depends only on the temperature. This is because that the effect of dissolved salts has been proved to be negligible compared with temperature (Newman et al., 2005).

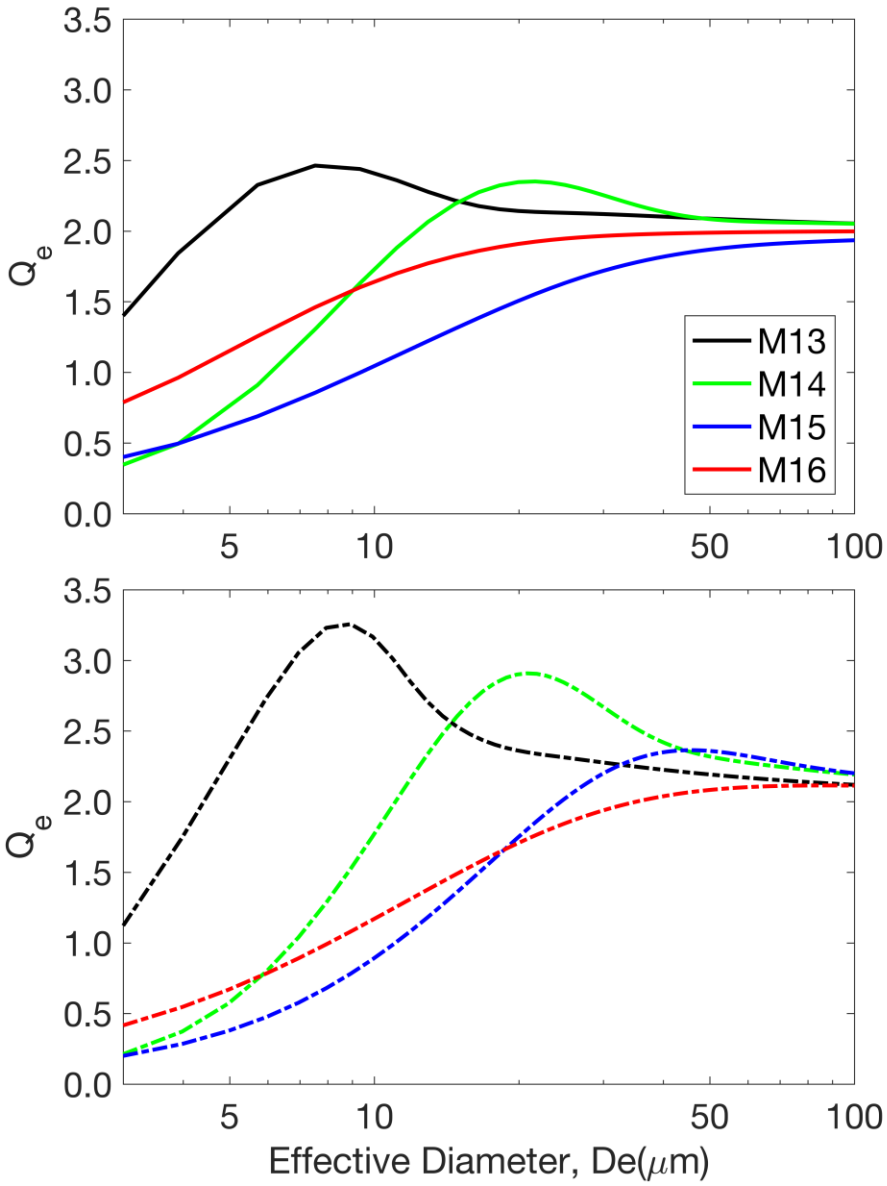

Figure 4.1 Extinction efficiency (Q_e) of ice(upper) and water(lower) particles as a function of effective particle diameter for VIIRS bands M13, M14, M15, and M16 centered at 4.05, 8.55, 10.56, and 12.01μm, respectively. Each effective diameter is computed as the average for a simulated cloud pixel with the stated mean effective particle diameter and a relative standard deviation of 0.1.

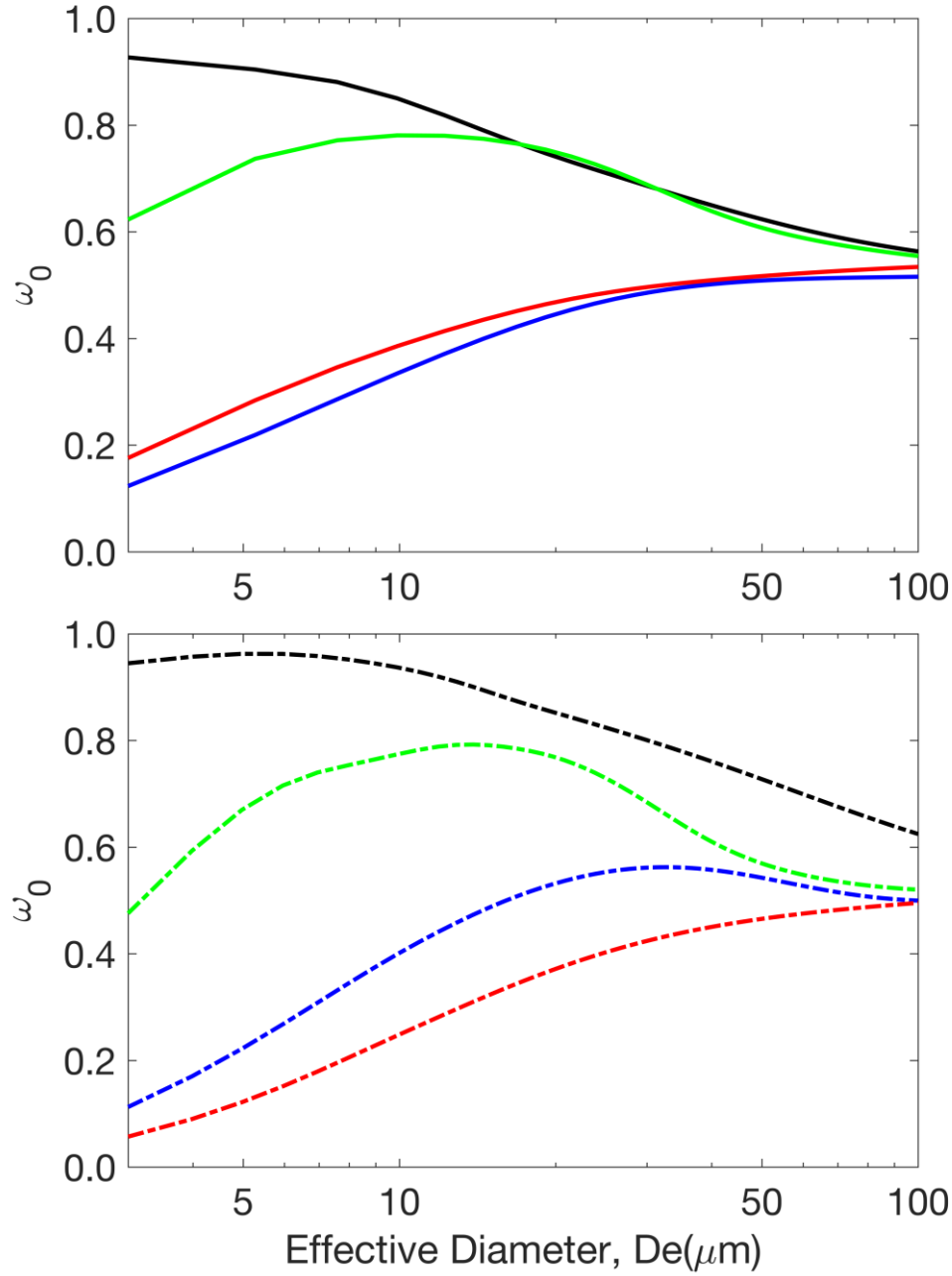

Figure 4.2 Similar to Figure 4.1, Single-scattering albedo (ω_o) of ice (upper) and water (lower) particles as a function of effective particle diameter.

4.3. Retrieval methods

This section provides the theoretical basis of multi-layer retrieval. Firstly, general principles and method feasibility will be presented; and then, specific implementation steps will be explained.

4.3.1. Ratios of absorption optical depths (β)

According to previous studies, ratios of absorption optical depths (β) between two different spectral bands(x, y) could be calculated with cloud emissivity (e_c) from different bands (Paro et al., 1991; Heidinger et al., 2015). Then, the β value can be expressed as follows:

$$\beta = \frac{\ln(1-e_{c,y})}{\ln(1-e_{c,x})}, \tag{4.2}$$

Generally, β values can be approximately expressed by single scattering properties of single scattering albedo (ω_o), the asymmetry factor (g) of the phase function, and the extinction efficiency (Q_e). Then we can use bulk scattering properties, which are integrated over MC6 size distribution with single scattering properties for both ice and water cloud, to compare the behavior of different wavelength and different phases. This approximation is very accurate, and the relationship is shown as follows:

$$\beta = \frac{Q_{e,y}(1-\omega_{o,y}g_y)}{Q_{e,x}(1-\omega_{o,x}g_x)}, \tag{4.3}$$

The spectral variation of the scattering properties for MC6 ice cloud and water cloud models at VIIRS M13 (4.05μm), M14 (8.55μm), M15 (10.76μm) and M16

(12.01μm) is shown in Figure 4.3. The β values shown in Figure 4.3 are the ratios of absorption optical depth with reference to 11μm, and the effective diameter is 40μm ice particle. The shaded areas are spectral response functions of M13, M14, M15, and M16, respectively. Solid lines show the scattering properties of ice cloud particles, while those dash lines represent water droplets.

We can see that, extinction efficiency of ice particle generally smaller than water droplets for all bands, except M16. The difference is smallest at MWIR, and greatest at M15 area. As for β values, ice particles and water droplets perform opposite patterns for MWIR and thermal IR regions, which shows great feasibility to distinguish, even derive the optical properties of multi-layer clouds.

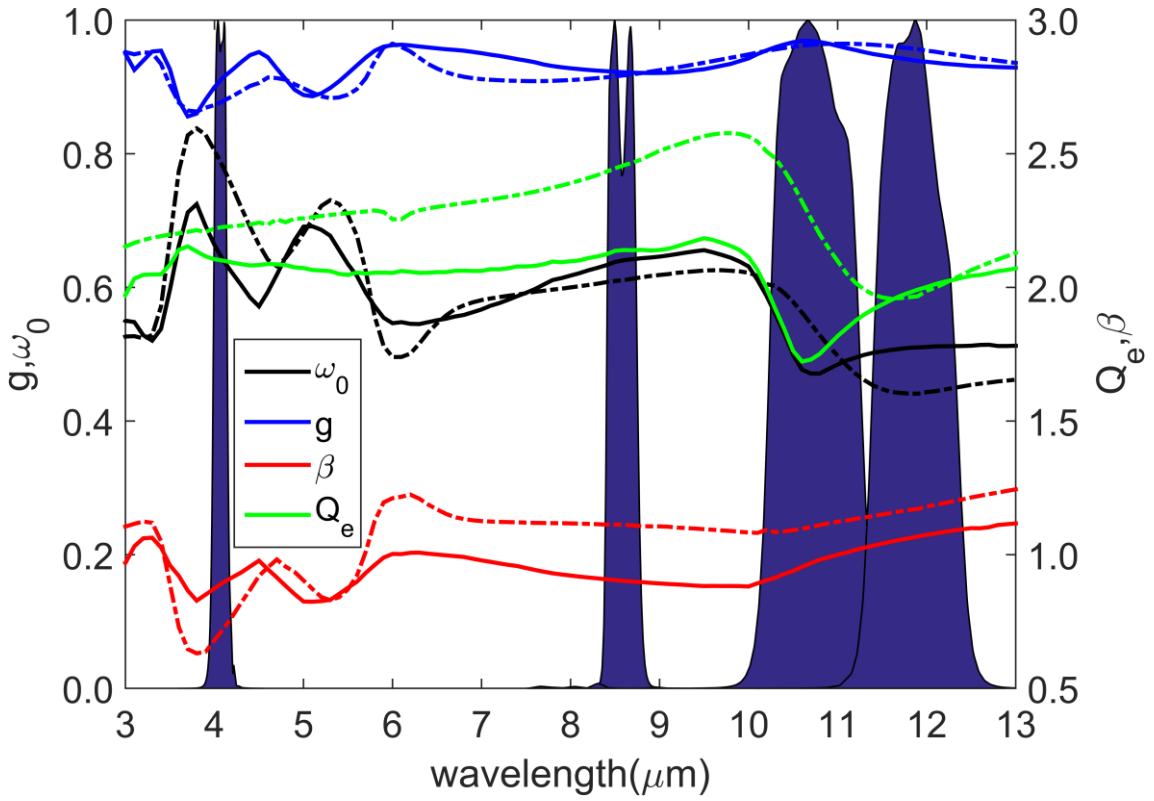

Figure 4.3 Spectral variation of the single scattering properties for ice (solid line) and water (dash line) particles over the spectral range of VIIRS bands M13-16, assuming an effective particle size of 40 μm. The shaded regions show the spectral response functions for bands M13-16.

Figure 4.4 shows the variation of β values vary with effective size between band M14 and M15. Figure 4.5 shows the same plot for M15 and M16, and Figure 4.6 for M13 and M15.

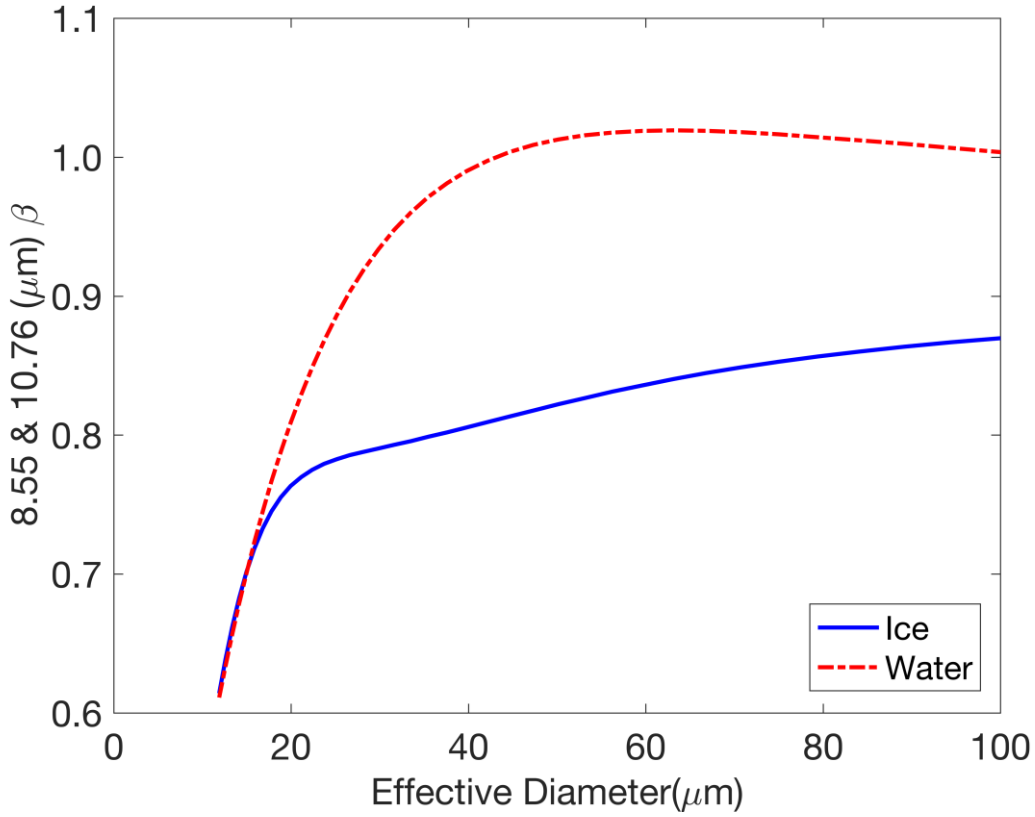

Figure 4.4 Variation of β computed using the VIIRS 10.76 μm and 8.55 μm channels as a function of effective diameter for cloud particles.

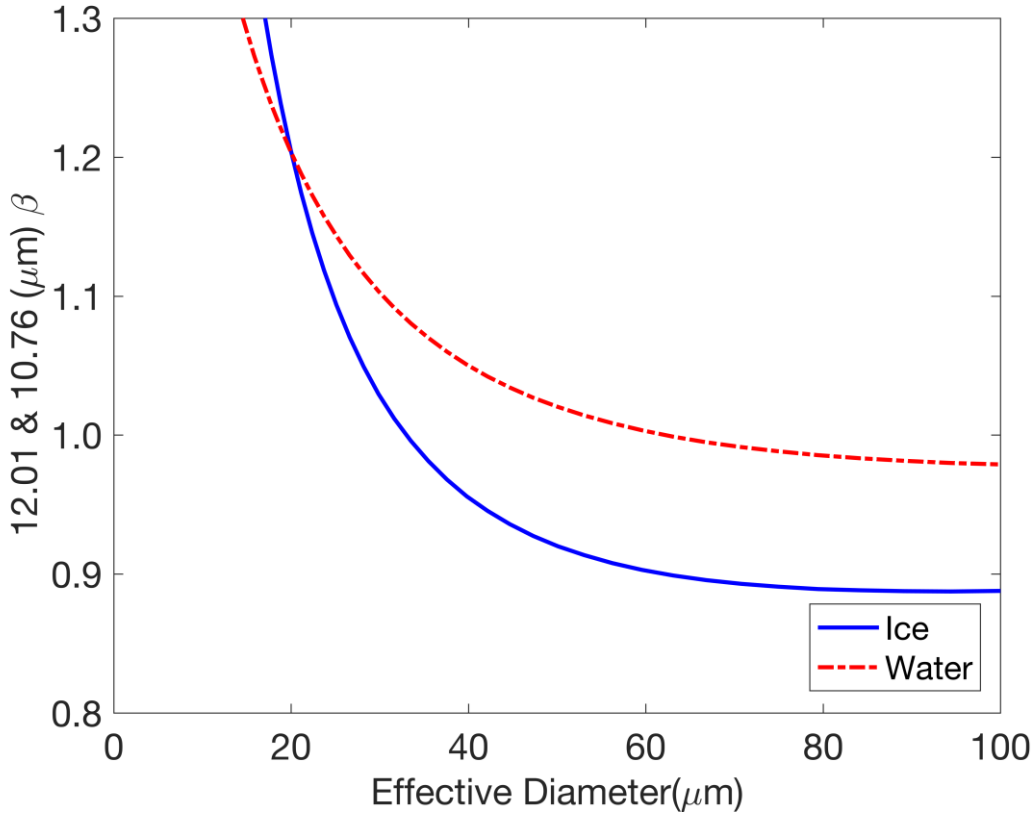

Figure 4.5 Variation of β computed using the VIIRS 10.76 μm and 12.01 μm channels as a function of effective diameter for cloud particles.

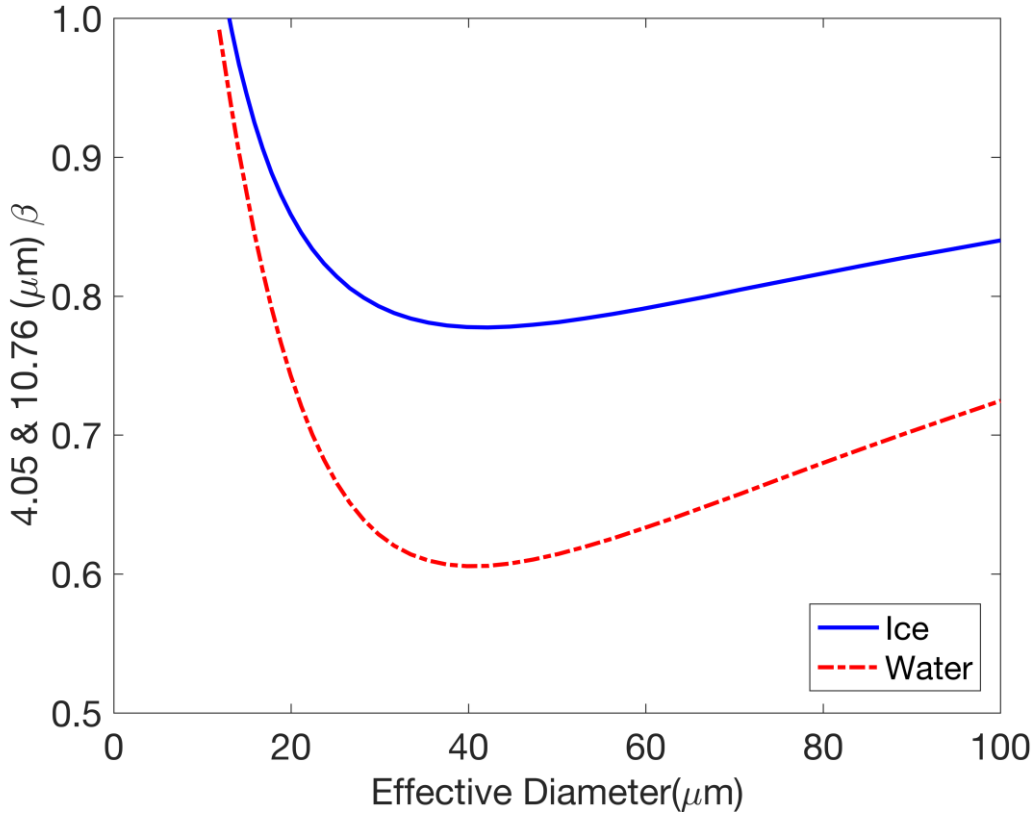

Figure 4.6 Variation of β computed using the VIIRS 10.76 μm and 4.05 μm channels as a function of effective diameter for cloud particles.

According to the β values, the retrieval of ice and water cloud particles is feasible. As Figures 4.4-4.6 show, we find that the relationship between β values and particle effective diameters is monotonic. Based on these sensitivity test results, it can be asserted that ice and water cloud coexist scenarios can be retrieved, in other words, multi-layer and multi-phase cloud property retrievals can be derived with VIIRS multi-band measurements.

4.3.2. Bayesian retrieval algorithm

The Bayesian retrieval method (Evans et al., 2002) uses a set of pre-determined ice and water cloud τ and D_e pairs, and then calculates various bands BTs in real time for the relevant LUTs with the help of corresponding atmospheric profile and cloud geometric information. Finally, by integrating over the points in the LUT with Bayes theorem, cloud optical properties can be derived. Bayes theorem can be stated mathematically as following:

$$p_{post}(x|T) = \frac{p_f(T|x)p_p(x)}{\int p_f(T|x)p_p(x)dx}, \tag{4.4}$$

where x is the cloud property vector (here, vector elements are pairs of ice and water cloud τ and D_e used to simulate TOA brightness temperature); T is the vector of TOA brightness temperature measurements in the VIIRS bands; $p_p(x)$ is the prior probability density function of cloud property x; $p_f(T|x)$ is the conditional probability of BT given the cloud property vector x; and $p_{post}(x|T)$ is the posterior probability density function of the cloud property given the TOA BT measurements. The prior probability density function $p_p(x)$ is based on previous research of cirrus cloud property retrievals. The uncertainty of the cloud spatial and temporal distribution is normalized to 1.

The retrieved cloud property vector x_{ret} is calculated by integrating over the entire x space to find the weighted average value:

$$x_{ret} = \int x p_{post}(x|T)dx, \tag{4.5}$$

In practice, this integral process is replaced by summing over the defined x vector:

$$x_{ret} = \sum x_i p_{post}(x_i|T), \tag{4.6}$$

The conditional probability density function $p_f(T|x)$ is the probability density of the TOA BT vector given defined cloud properties; i.e., the probability of a TOA BT measurement (T) given forward RTM simulations (R) of the atmospheric and cloud parameters. We assume a normal distribution function to represent the probability of each observed BT value:

$$p_f(T|x) = \prod_{j=1}^{M} \frac{1}{\sqrt{2\pi\sigma_j^2}} \exp\left(-\frac{\left(T_j - R_j(x)\right)^2}{2\sigma_j^2}\right), \tag{4.7}$$

where T_j is the BT vector for band j (here, VIIRS band M14, M15, or M16); $R_j(x)$ is the VFRTM simulated result for band j; and σ_j is the standard deviation for band j. We assume that the uncertainty σ_j is due entirely to measurement errors. The measurement errors are assumed to be unbiased and the range of calibration errors is on the order of 0.3 K or less (Moeller et al., 2013). The measurement errors are assumed to be 0.3 K for all three bands and are independent of each other.

4.3.3. Optimal estimation (OE) algorithm

The OE method is an efficient inversion method (Rodgers, 2000; Iwabuchi et al., 2014) with the ultimate goal of deriving an optimized solution from observations given certain constraints. Generally, OE method retrieval uses the same technique as previous paper stated (Ding et al., 2017), the major difference is to include MWIR bands to derive ice-water multi-layer cloud properties.

4.4. Retrieval algorithm evaluation

To evaluate the performance of aforementioned retrieval algorithms, Bayesian and OE method, a sensitivity study based on synthetic measurements simulated with specified perturbed model parameters is conducted. The simulation process uses a set of cloud properties as control parameters, including τ, D_e, and H_{cloud} for two layers (listed in Table 4.1). The geometric thickness of each cloud is assumed to be thin enough within one layer as fast model requires. A standard mid-latitude summer profile (McClatchey et al., 1972) are assumed, the surface albedo is assumed to be constant to 0.02 and surface temperature is 298K. The synthetic measurements are perturbed 10,000 times by adding Gaussian distributed bias for 4 VIIRS bands, and the standard deviation is 0.3K. Other model parameters such as atmosphere temperature, surface temperature, water vapor content and other absorbing gas amount obey the Gaussian distribution as well. Standard deviations of those model parameter bias are shown in Table 4.1. All kinds of variable errors are assumed to be independent of each other. In order to better compare these two retrieval methods, only measurement error was considered for OE method, so that we can eliminate the effect of errors sourced from simulator and model parameters.

Table 4.1 Reference cloud properties of synthetic retrieval analysis

	Variable Names	Values
Reference cloud properties	Cloud optical thickness	0.1, 0.3, 0.5, 0.75, 1, 1.5, 2, 3, 5, 10
	Effective diameter (μm)	10, 15, 20, 25, 30, 40, 50, 60, 80, 100
	Cloud top height (km)	5 (water), 10 (ice)
Model parameters(errors)	Surface temperature (K)	298K (0.5K)
	Surface emissivity	0.98 (0.01)
	Temperature profile	Mid-latitude profile (1K)
	Water vapor profile	Mid-latitude profile (15%)

Figure 4.7-4.11 are showing retrieval results and uncertainties for two different methods. The cross point of each solid cross marks the averaged retrievals with 10,000 synthetic measurements. Different colors represent different effective diameters. The bars of solid cross are error bars, indicating the standard deviations of retrievals. The horizontal bars are standard deviations of tau, while the vertical bars are standard deviations of De, respectively. Reference cloud properties are shown as dashed line intersections. Figure 4.7-4.10 are showing ice cloud property retrieval performance. Thin water cloud scenarios (τ_w = 0.3, D_{ew} = 30μm), shown in Figure 4.7, have a relatively poor performance under thin ice cloud conditions, especially for τ_i smaller than 0.5. There is an interesting feature that Bayesian method retrieval trends to have greater optical thickness uncertainty and smaller cloud particle size uncertainty compared with OE method retrieval at thin water cloud scenarios. Figure 8 shows the averaged retrieval results, which highlight the retrieval

result pattern. Figure 9-10 are showing ice cloud property retrieval performance under thick water cloud scenarios ($\tau_w = 5.0$, $D_{ew} = 80\mu m$). We can see that, overall, both methods have a much better performance compared with previous thin water cloud conditions. Figure 4.11 is showing averaged optical thickness retrieval results for both ice and water cloud. The horizontal bars are standard deviations of ice cloud optical thickness, while the vertical bars are standard deviations of water cloud one, respectively. Generally, for the range of moderate thin clouds, i.e. tau from 0.5 to 5.0, bias of retrievals is negligible for both thin and thick water cloud scenarios. However, retrieval biases appear at very thin water cloud conditions, tau smaller than 0.3, and very thick, tau greater than 5, scenarios. And we can find that, for both methods, thick ice cloud will lead to a greater water cloud retrieval bias, while thick water cloud usually have a positive effect on ice cloud retrieval. Above mentioned retrieval performance illustrates that the sensitivity of IR observations to ice cloud optical thickness derivation decreases rapidly if the water cloud becomes optically thin, leading to a larger retrieval uncertainty. In addition to this, thicker ice cloud also obstructs the retrieval of lower water cloud.

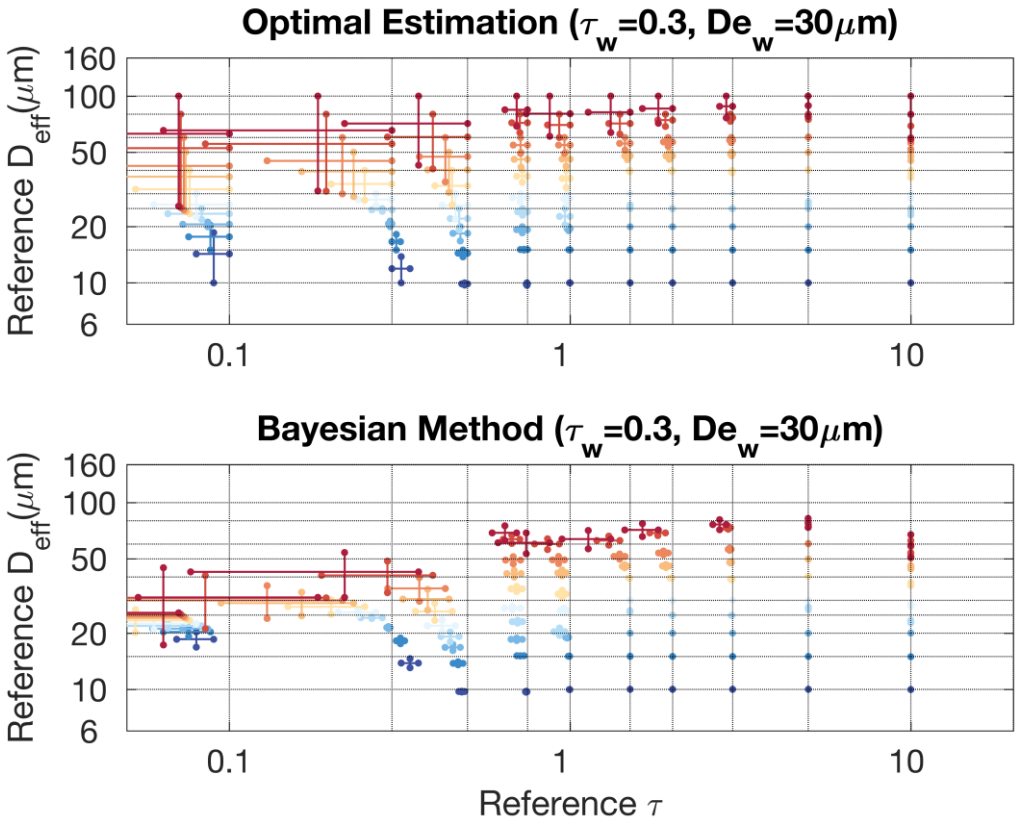

Figure 4.7 Averaged ice cloud properties and corresponding uncertainties inferred from synthetic observations. The different colors indicate different reference De values. The solid vertical and horizontal bars indicate the averaged De and τ retrieval uncertainties, respectively. The averaged retrievals are located at the intersections of the solid bars. The reference cloud properties are located at the intersections of the dashed horizontal and vertical lines. The underlying cloud is thin water cloud, D_e = 30μm and τ = 0.3. (top) OE method (bottom) Bayesian method.

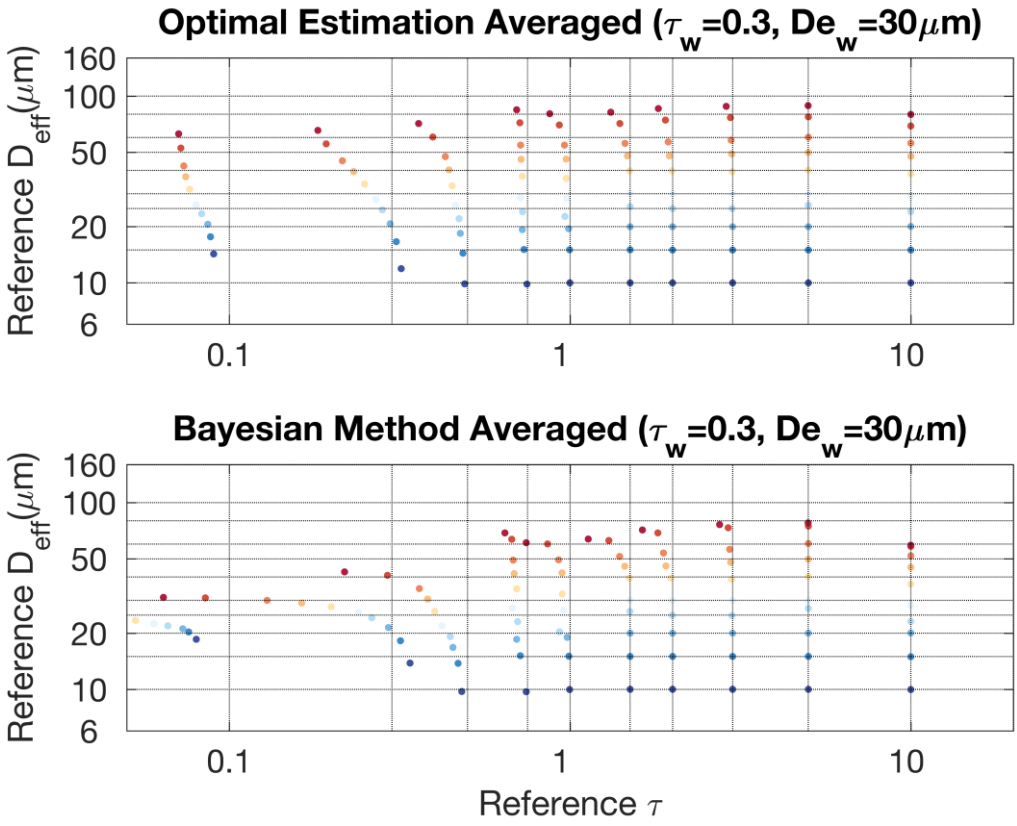

Figure 4.8 Same as Figure 4.7, averaged retrieval results.

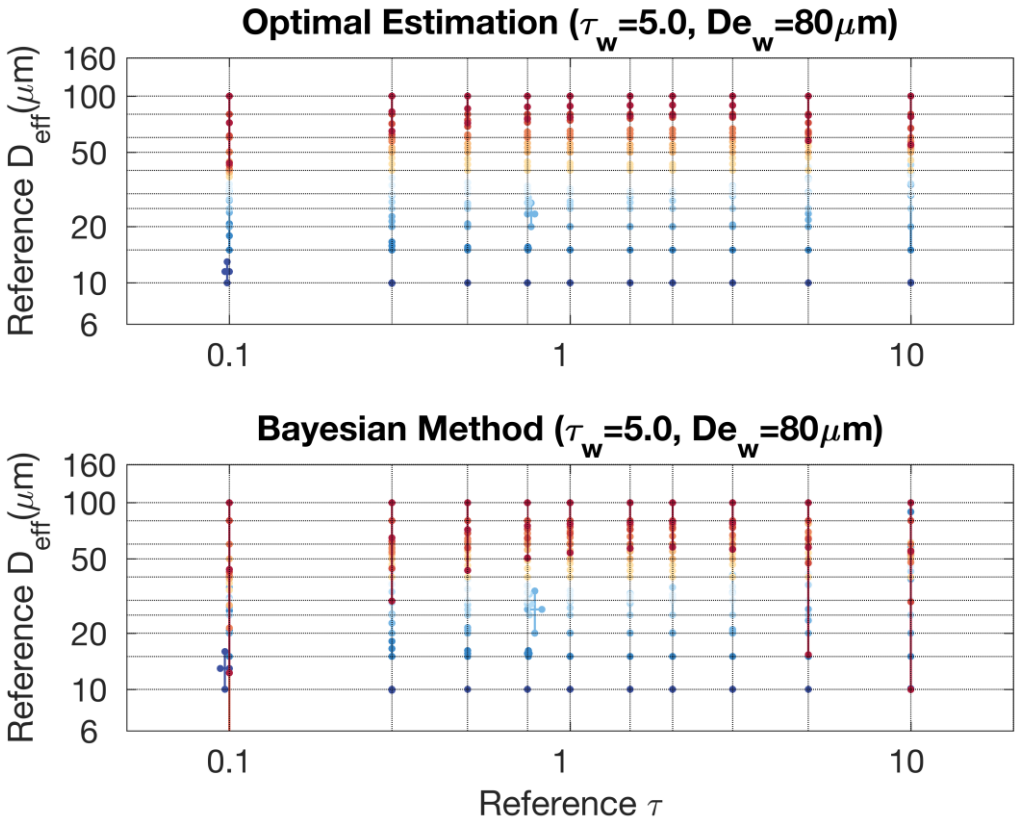

Figure 4.9 Similar to Figure 4.7, the underlying cloud is thick water cloud, D_e = 80μm and τ = 5.0.

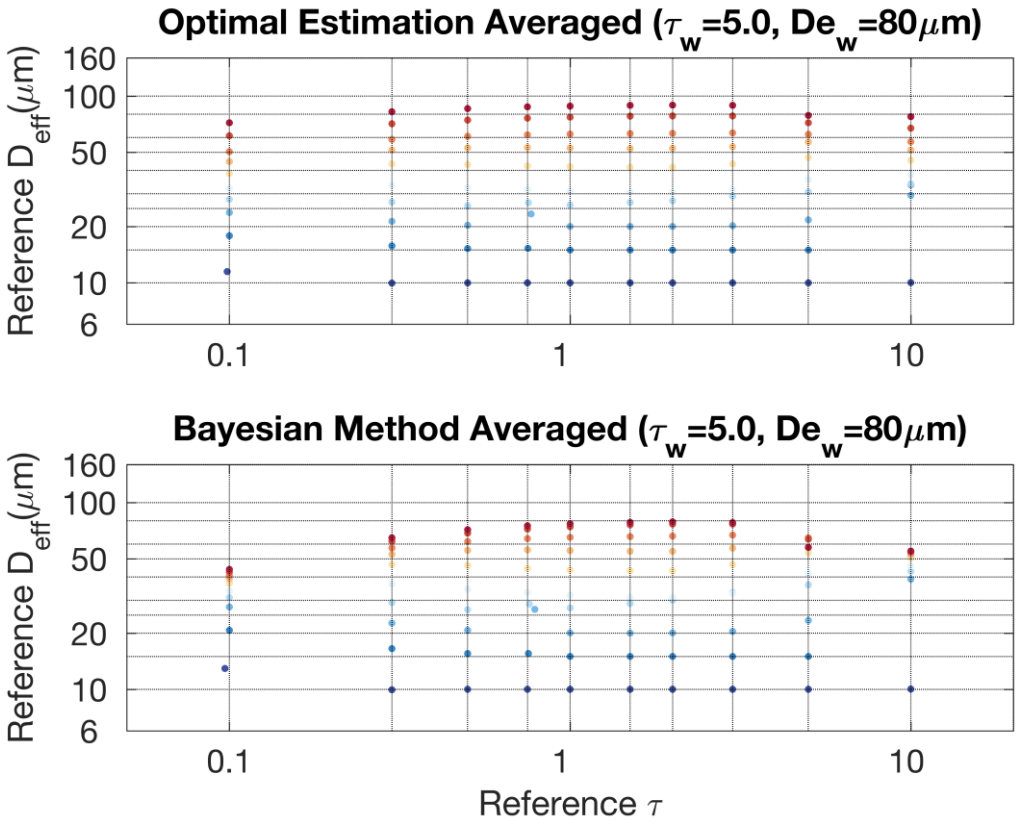

Figure 4.10 Same as Figure 4.9, averaged retrieval results.

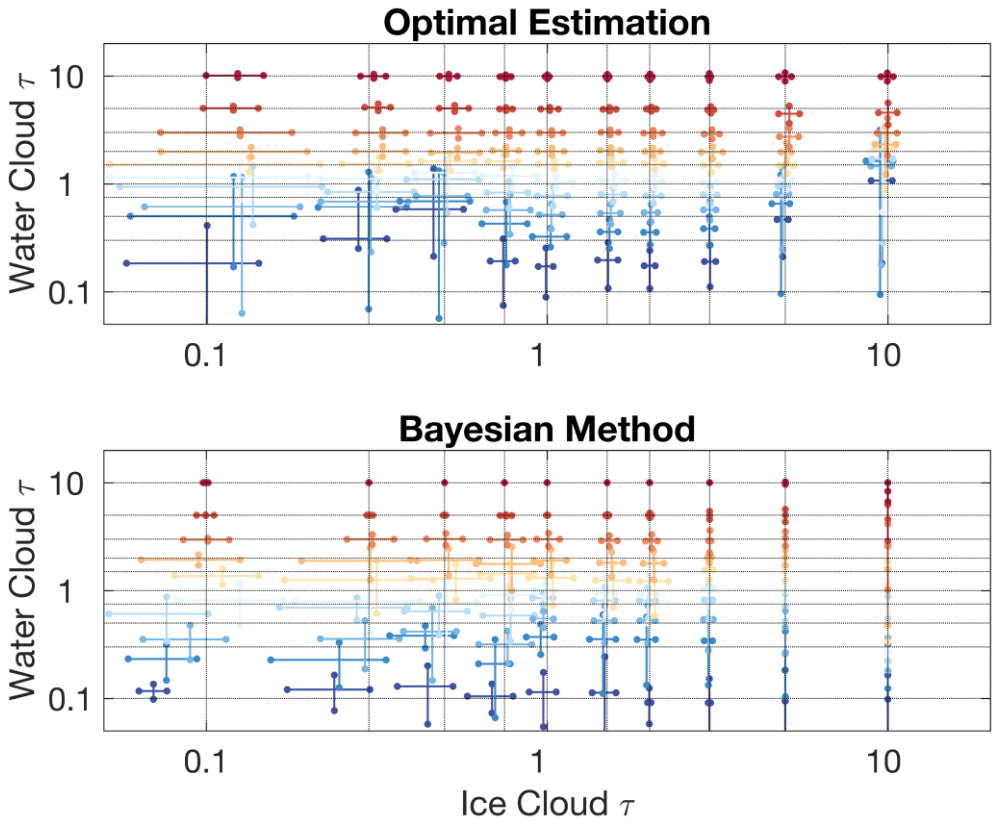

Figure 4.11 Averaged optical thickness retrieval results for both ice and water cloud.

4.5. Case study

The first dataset used are VIIRS JPSS SDR products, which provide level 1B data, including brightness temperatures(BTs) in all bands. The measurement errors are assumed to be unbiased and the equivalent range of calibration BT errors is on the order of 0.3 K or less (Moeller et al., 2013). The measurement errors are assumed to be 0.3 K for all bands and are independent of each other. Modern Era Retrospective Analysis for Research and Applications (MERRA) data provide atmospheric profiles and surface temperatures at a spatial resolution of 1.25°, and temporal resolution of 3 hours. The ocean surface

temperature is derived from the MERRA surface air temperature using a linear interpolation technique. The ocean surface albedo is computed with the Fresnel reflectance based on a surface temperature dependent flat ocean surface (Newman et al., 2005). The Cloud-Aerosol Lidar with Orthogonal Polarization (CALIOP) is onboard the platform named Cloud-Aerosol Lidar and Infrared Pathfinder Satellite Observations (CALIPSO). CALIOP can receive 532 and 1064 nm backscatter signals. Since CALIOP is very sensitive to thin scattering media, such as thin ice cloud and aerosols, it can be used as a reliable reference. In this study, the CALIPSO/CALIOP 5km spatial resolution level-2 cloud-layer products, "CAL_LID_L2_05kmCLAY" (version 3.30), are selected to provide comprehensive cloud information, such as the cloud altitude, and to select high and low clouds coexist pixels. To be specific, only geometrically ice clouds over water clouds are selected. Partly cloudy pixels and mixed phased cloud pixels reported in the "CAL_LID_L2_05kmCLAY" datasets are not considered. In this study, collocated LIDAR retrieval products from CALIPSO for whole year 2015 are used as evaluation. Figure 4.12 shows on example of collocated CALIPSO and VIIRS image. The grayscale granule image is the VIIRS M05 reflectance image and the red line indicates the overtake CALIPSO track. The CALIPSO 532 nm total attenuated backscatter image is showing cloud-atmosphere vertical structure in Figure 4.13. Figure 4.14-4.15 are showing feature type and cloud phase along the CALIPSO ground track shown in Figure 4.13.

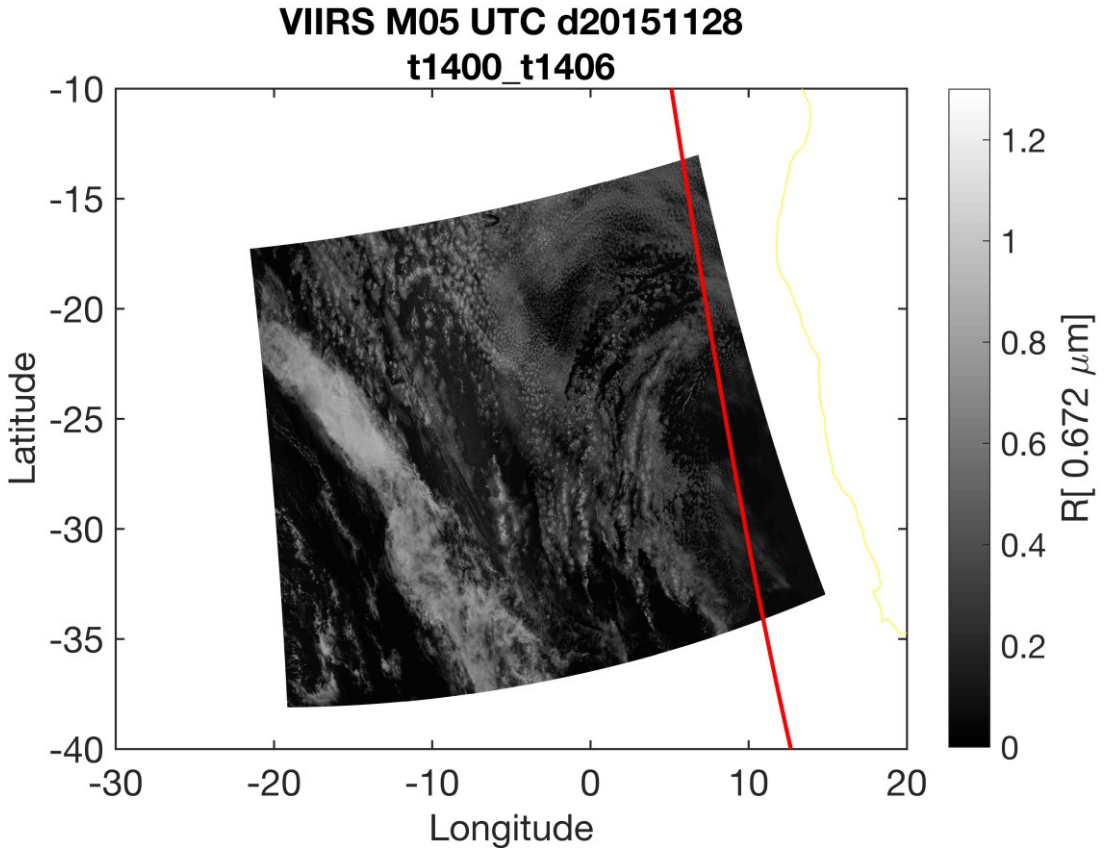

Figure 4.12 The 0.672µm reflectance for a VIIRS granule at 1400 UTC 20151128. The red line indicates the associated CALIPSO/CALIOP ground track.

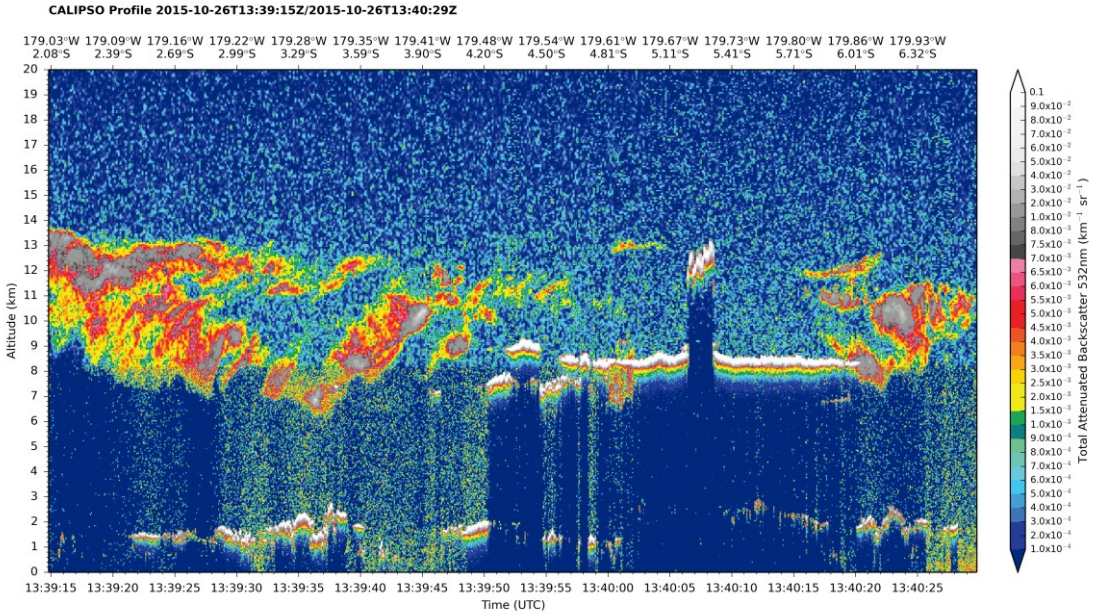

Figure 4.13 The CALIPSO 532nm total attenuated backscatter along the ground track line. The white lines indicate the eligible profiles.

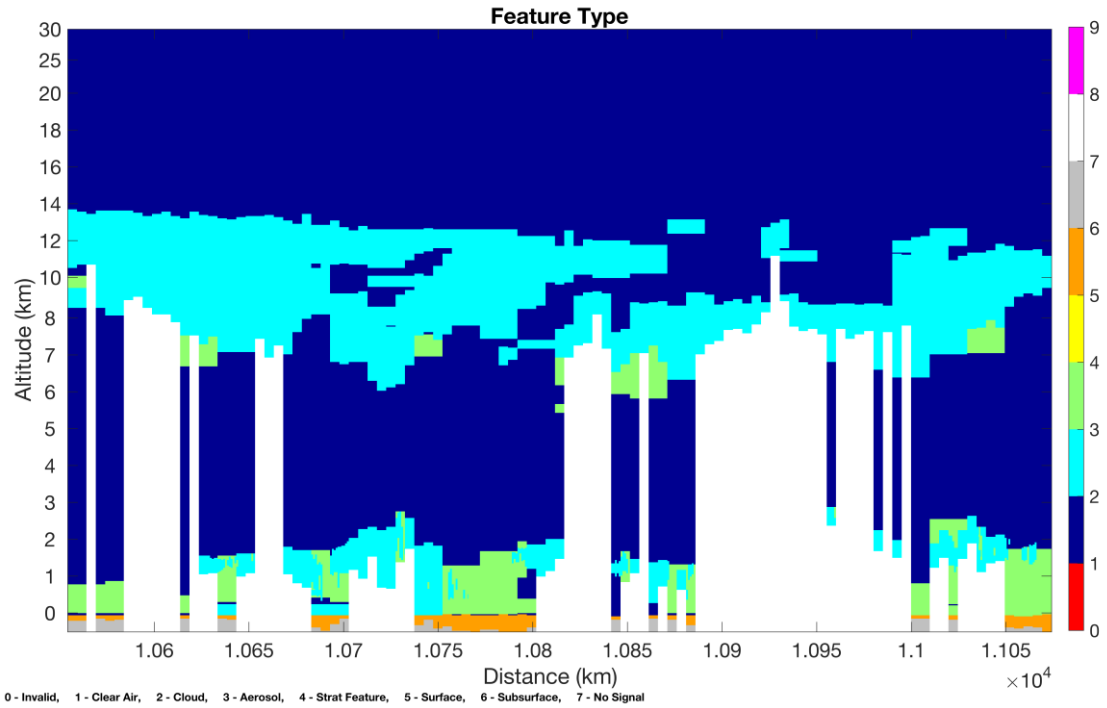

Figure 4.14 Feature type along the CALIPSO ground track shown in Figure 4.13.

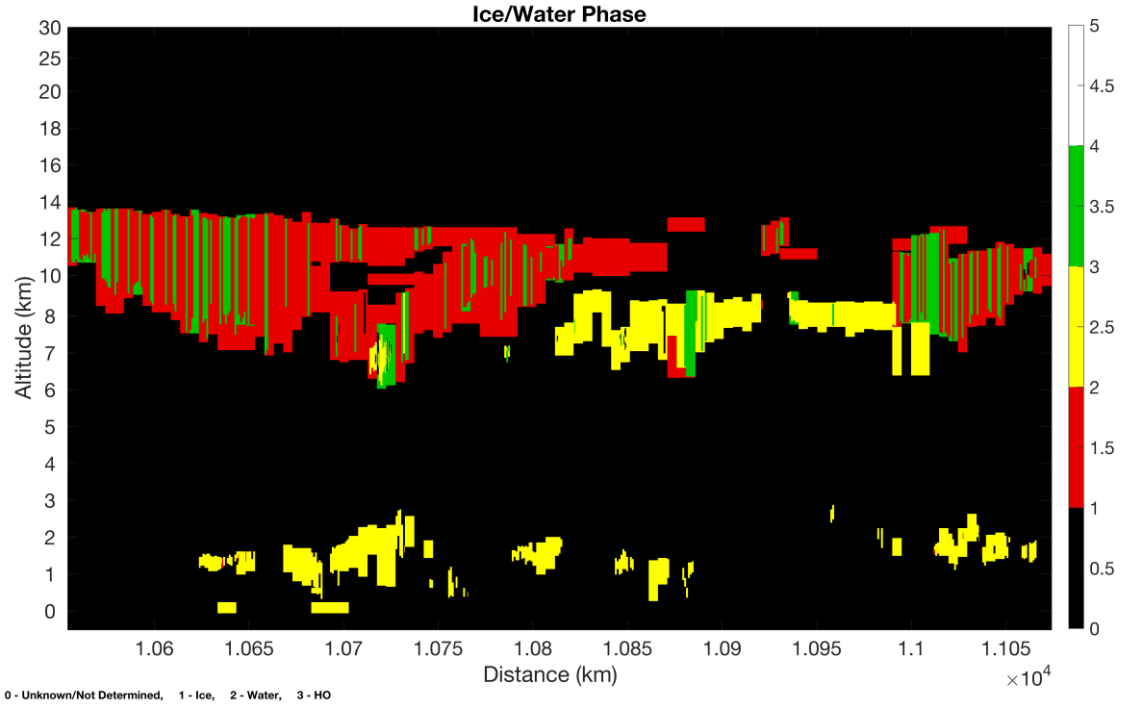

Figure 4.15 Cloud phase along the CALIPSO ground track shown in Figure 4.13.

As previously stated, MWIR channels are used to derive optical properties, therefore, we use nighttime granules only to eliminate the influence from solar reflectance. The scatterplots in Figure 4.16 compare the CALIPSO retrieved cloud properties and aforementioned two methods with VIIRS M13-M16 bands retrieval results. Generally, MWIR-thermal IR retrieved cloud optical thickness values are systematically greater than CALIPSO counterpart ones, no matter ice cloud or water cloud, OE method or Bayesian method. There are approximately 90% of the ice cloud optical thickness values are smaller than 4.0, and the percentage of water cloud ones is about 60%. Besides, grid-like pattern appears on Bayesian method retrieved results. Figure 4.17 and 4.18 show the retrieval results with different VIIRS measurements. In Figure 4.17, there are M12 and M14-16,

while, for Figure 4.18, they are M12-M16, five bands. They all show similar patterns as Figure 4.16. The quantified retrieval performance details are shown in Table 4.2. By comparing the relative bias of all three measurement combinations, we find that, the combination consists of M12 and M14-16 is the best one to derive the multi-layer cloud properties. And, Figure 4.19 shows the distributions of both methods and CALIPSO retrieved cloud optical thickness. We can see that OE method retrieval result is highly correlated with CALIPSO retrieval, and the major difference is the amplitude of optical thickness normalized frequency, while Bayesian method leans to smaller optical thickness for both ice and water clouds. In this way, we can say that OE method is superior to Bayesian method in deriving multi-layer cloud properties.

Table 4.2 Comparison of OE retrievals with Bayesian method retrievals

Method	Band	RMSD(wat)	R(wat)	RMSD(ice)	R(ice)
OE method	M12 & M14-16	0.8753	0.7226	0.1853	0.7908
	M13-16	0.8423	0.5546	0.4098	0.7297
	M12-16	0.8613	0.6155	0.2820	0.6917
Bayesian method	M12 & M14-16	1.8023	0.3175	0.2304	0.5526
	M13-16	1.1420	0.2462	0.5304	0.5769
	M12-16	1.7973	0.2833	0.2986	0.6107

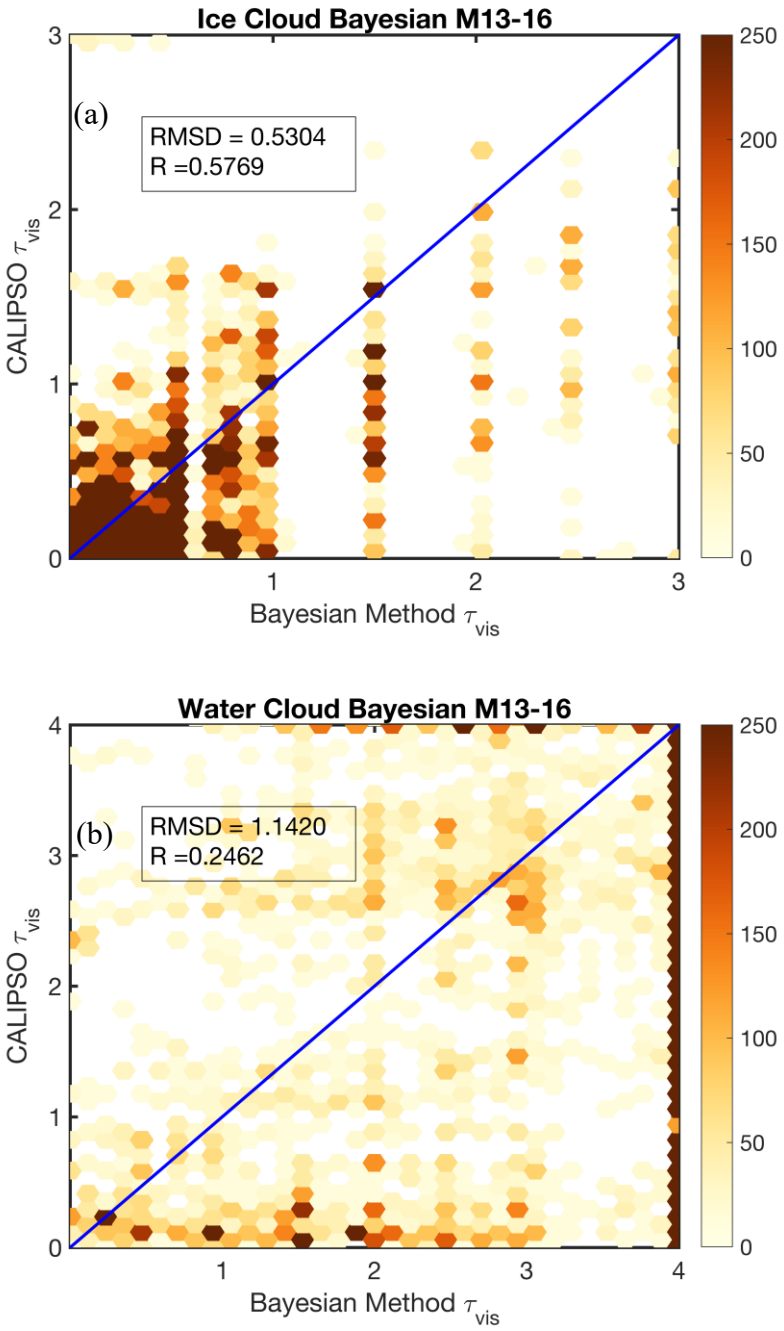

Figure 4.16 A joint histogram of the IR retrievals and CALIPSO products using VIIRS M13-16 bands for eligible pixels in 2015: (a) Bayesian method ice cloud, (b) Bayesian method water cloud, (c) OE method ice cloud and (d) OE method water cloud. The correlation coefficient (R) and the RMS difference (RMSD) are also shown in text box.

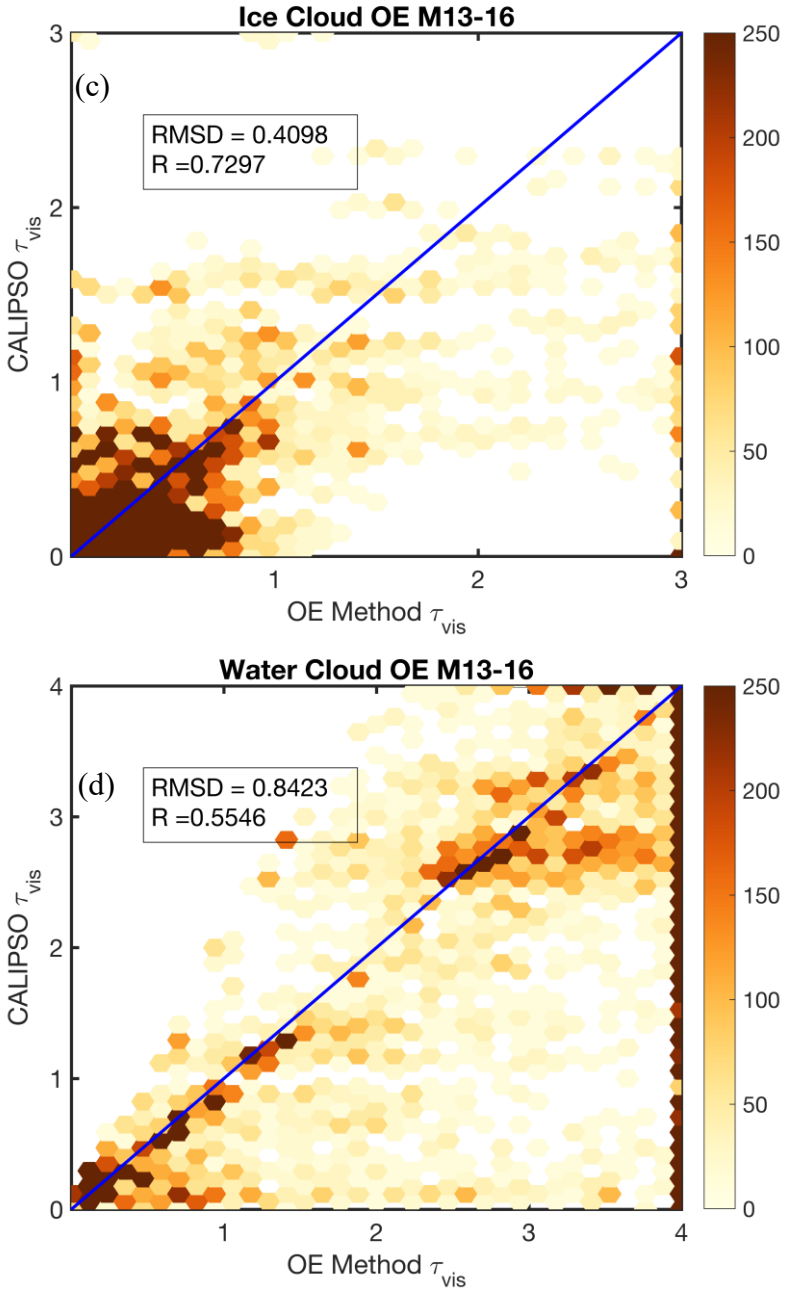

Figure 4.16 Continued.

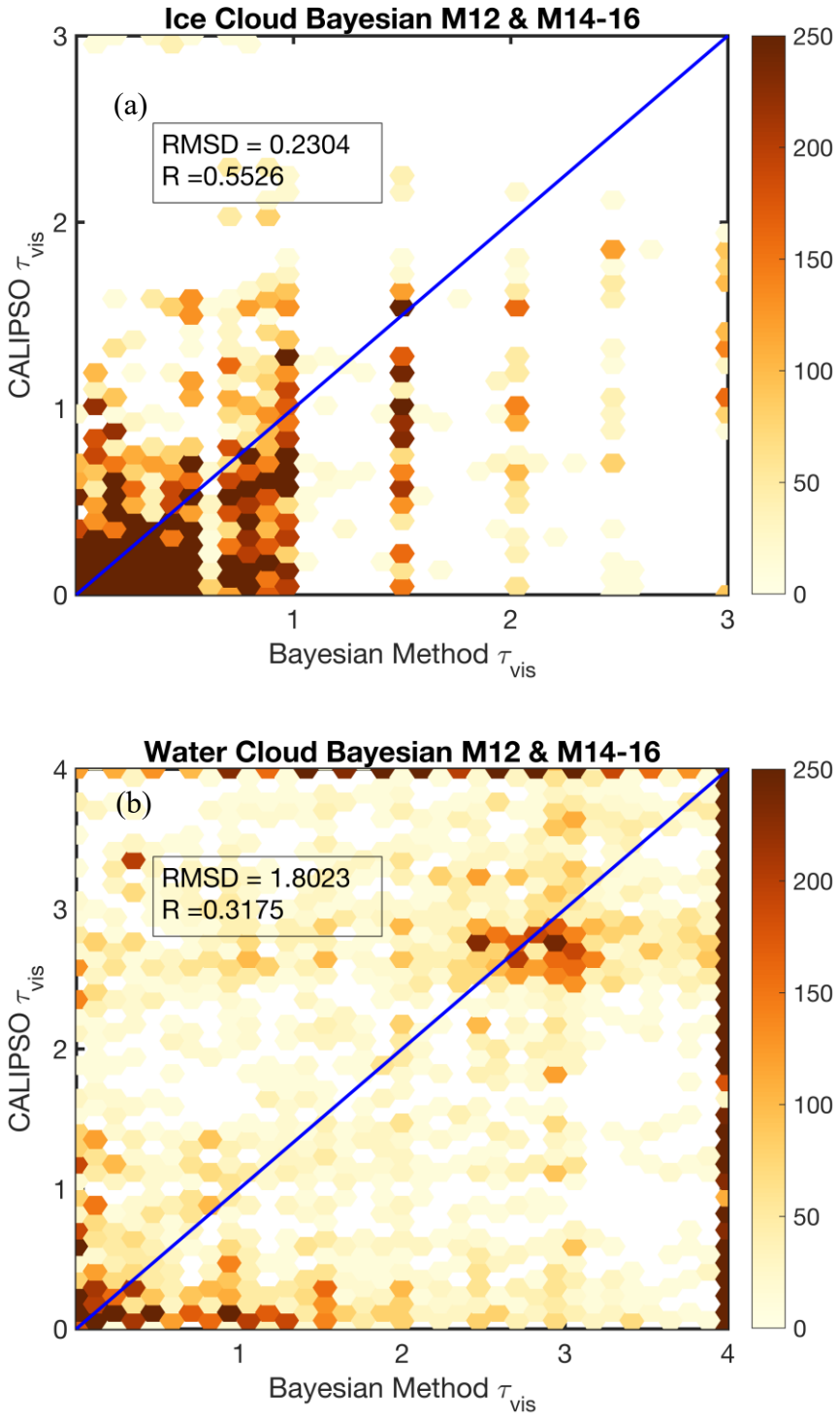

Figure 4.17 Similar joint histogram as Figure 4.16 using VIIRS M12-16 bands.

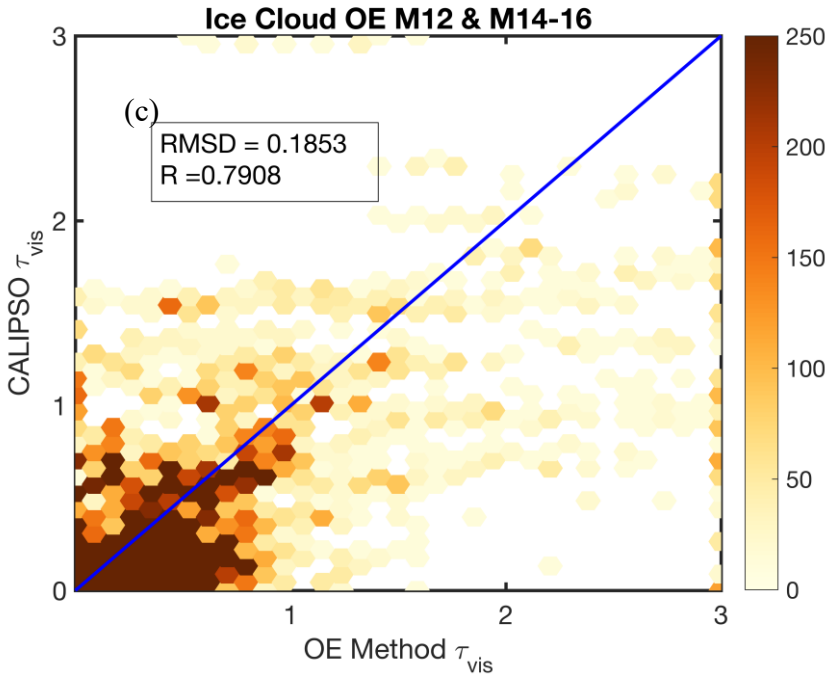

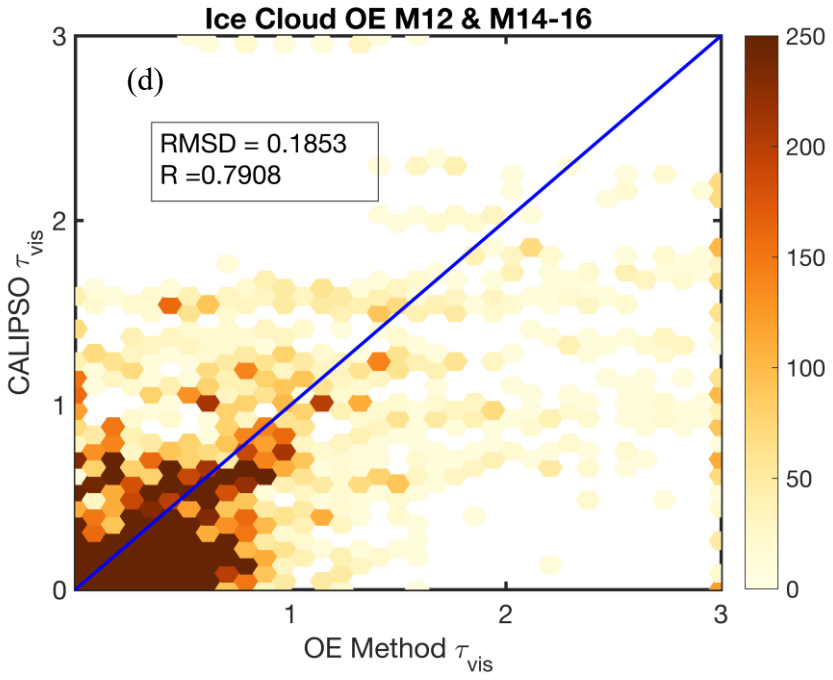

Figure 4.17 Continued.

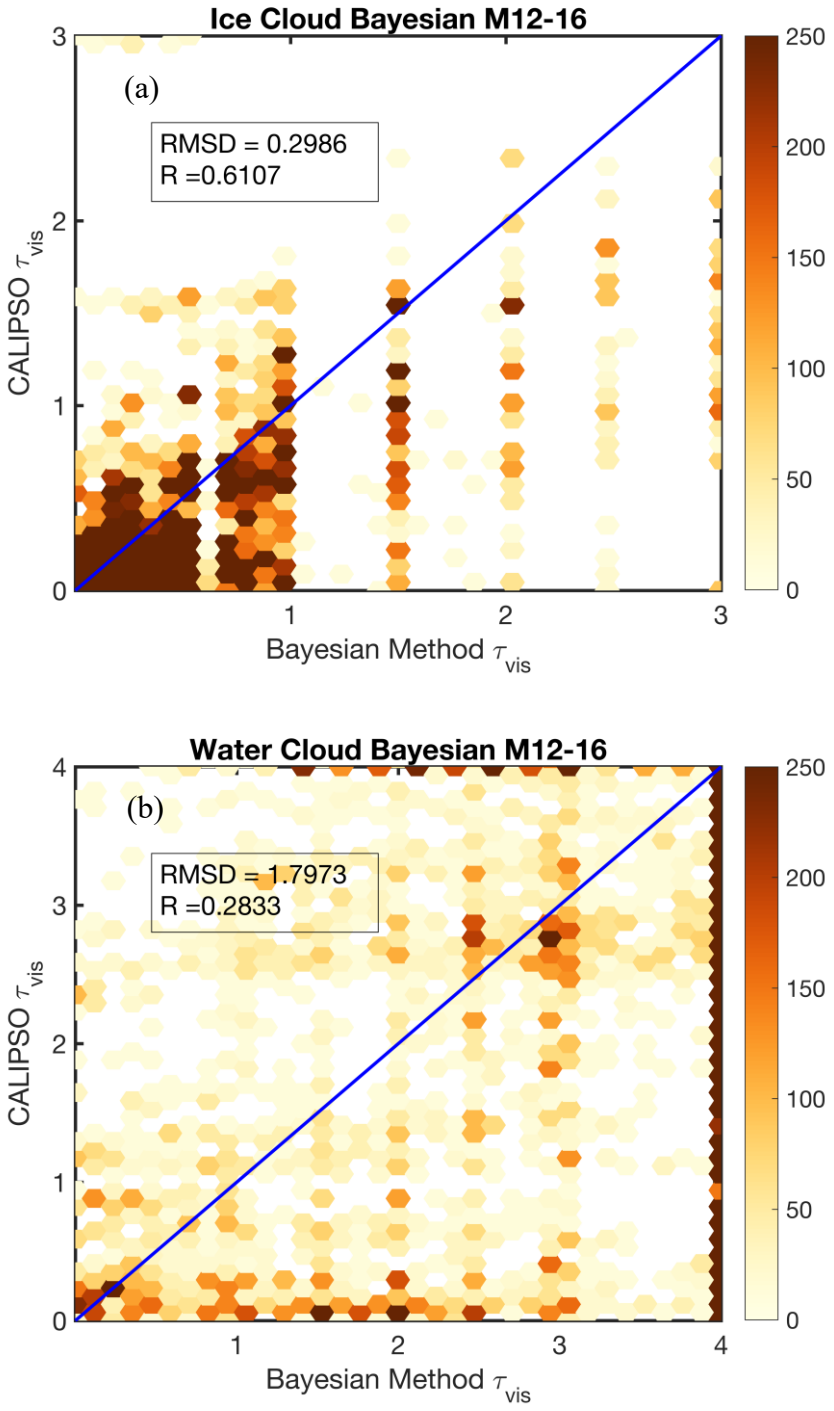

Figure 4.18 Similar joint histogram as Figure 4.16 using VIIRS M12-16 bands.

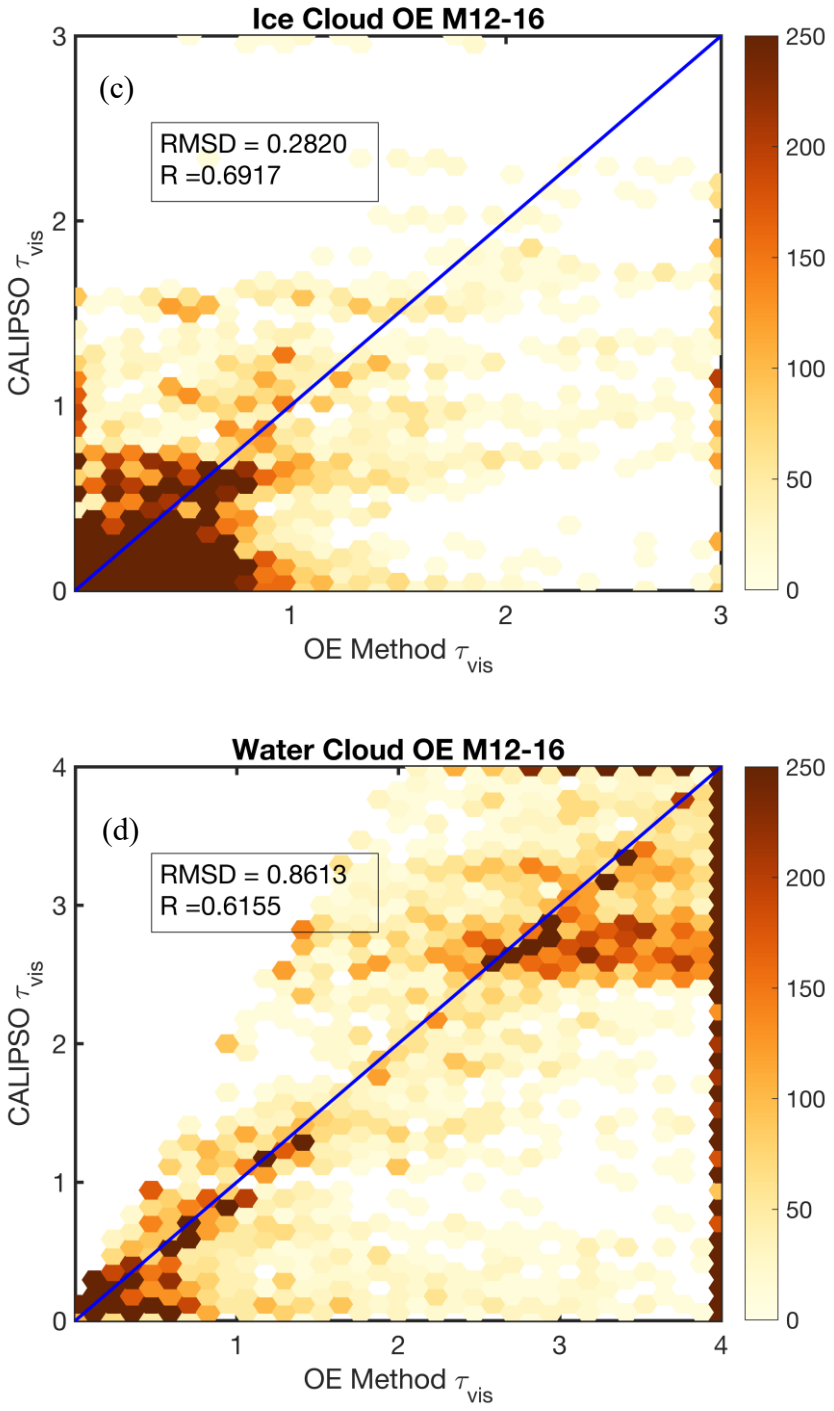

Figure 4.18 Continued.

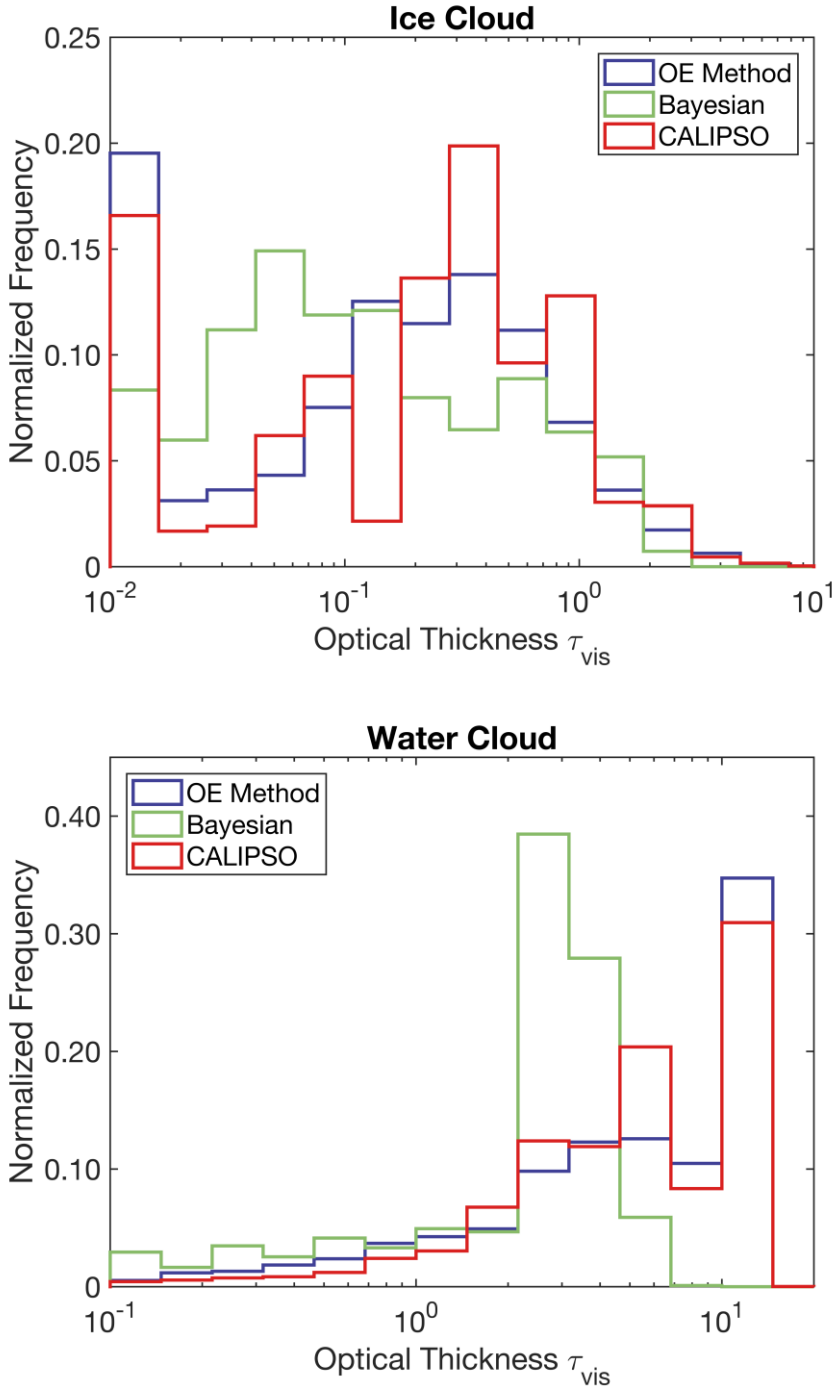

Figure 4.19 Cloud optical thickness distribution given by the IR retrieval results and CALIPSO products. (top) ice cloud (bottom) water cloud.

Besides, since multi-layer cloud property retrieval is a high degree of freedom problem, it is usually a time-consuming process to solve this kind of problem. Therefore, we will have to take computational efficiency into consideration. Because of the theoretical basis of Bayesian method, it is required to traverse the pre-defined cloud property LUT, which results in an exponential computational burden increasing when the number of variables need to be solved linear increases. Meanwhile, OE method is relatively insensitive to the increasing number of variables. Thus, OE method is more suitable to solve this kind of high degree of freedom problem. For this case, OE method is about 20 times faster than Bayesian method.

4.6. Conclusion

Our study compares two multi-layer cloud property retrieval algorithms using VIIRS M-bands centered at wavelengths 3.7, 4.05, 8.55, 10.76 and 12.01μm. Cloud top height, atmospheric profiles and underlying surface information are obtained from MERRA dataset and CALIPSO L2 products as priori. The single-scattering properties of cloud particles and size distributions are the same as MC06. The fast RTM, VFRTM, is based on the CKD technique, which is very computationally efficient to support real-time IR brightness temperature calculations. Based on appropriate model parameters, including spectral surface emissivity, cloud top heights, surface temperature, and atmospheric profiles, both aforementioned MW-/thermal- IR methods can derive the multi-layer cloud optical thickness. A significant positive correlation can be recognized from both OE method and Bayesian, meanwhile, the root-mean-square deviation (RMSD) is limited to

a small value. Therefore, the four-band, M12 and M14-16, OE method is the most suitable method to derive cloud optical thickness under multi-layer scenarios, where the RMSD is generally less than 30%.

By yearly case study, we find that the OE-IR method can be applied to multi-layer cloud optical thickness retrieval. Collocated comparison has demonstrated that the derived optical thickness from OE-IR method and that from CALIPSO product are significantly correlated. The retrieved results from OE-IR are slightly lean to larger values compared with CALIPSO products. Besides, OE-IR method has an advantage for the spatial distribution. Not like CALIPSO ground track pixels, OE-IR method can provide global cloud property retrieval. An advantage of the OE method compared with Bayesian method is that it is more computational efficient. Besides, OE method results are more continuous distributed, while Bayesian method results perform a grid-like pattern.

5. SUMMARY

In section 2, by using correlated-k distribution, band averaged cloud property, and pre-calculated cloud property look-up table techniques, we developed a fast radiative transfer model specialized for VIIRS IR bands based on the rigorous LBLRTM+DISORT method to simulate the forward radiative transfer processing involved in cloud remote sensing for cloudy-sky scenarios. Thanks to the techniques mentioned above, the computational efficiency associated with the line-by-line process is substantially increased. Compared with rigorous method, fast VIIRS RTM (VFRTM) is much faster with a high accuracy, thus, it is feasible to apply VFRTM to cloud remote sensing. Let alone the portability to apply this method to other narrow band satellite instruments.

With the help of VFRTM, we can efficiently derive the cloud properties given ancillary environment information. In section 3, we did the case study to retrieve cloud properties and analyze error sources with Bayesian method and Optimal Estimation method using VFRTM. We found that the VFRTM error contributes very little to the final uncertainty. The uncertainty of the model parameters (including errors in cloud top height, surface emissivity, and temperature) has the greatest contribution to cloud property retrieval errors. Among those factors, we find that the accuracy of the cloud height and the underlying surface temperature heavily influences the associated error in the retrieval of τ and D_e. Generally, τ retrievals have a much higher correlation with the control group retrieval, while much lower correlations are found with D_e retrievals. As for cloud property retrieval, firstly, both the OE and Bayesian methods are useful for inferring cloud optical thickness based on split-window IR measurements. We note that the Bayesian method is

approximately two times more efficient computationally than the OE method retrieval. An advantage of the OE method is that it provides more information useful for quality control because it produces several diagnostics related to retrieval quality (Iwabuchi et al., 2014).

In section 4, we have tested the possibility of applying aforementioned method to multi-layer cloud retrieval. We used VIIRS M-bands centered at wavelengths 3.7, 4.05, 8.55, 10.76 and 12.01μm, along with ancillary data, including Ccoud top height, atmospheric profiles and underlying surface information from MERRA dataset. Based on appropriate model parameters, including spectral surface emissivity, cloud top heights, surface temperature, and atmospheric profiles, both aforementioned MW-/thermal- IR methods can derive the multi-layer cloud optical thickness. A significant positive correlation can be recognized from both OE method and Bayesian, meanwhile, the root-mean-square deviation (RMSD) is limited to a small value. Therefore, the four-band, M12 and M14-16, OE method is the most suitable method to derive cloud optical thickness under multi-layer scenarios, where the RMSD is generally less than 30%. By yearly case study, we find that the OE-IR method can be applied to multi-layer cloud optical thickness retrieval. Collocated comparison has demonstrated that the derived optical thickness from OE-IR method and that from CALIPSO product are significantly correlated. The retrieved results from OE-IR are slightly lean to larger values compared with CALIPSO products. Besides, OE-IR method has an advantage for the spatial distribution. Not like CALIPSO ground track pixels, OE-IR method can provide global cloud property retrieval.

REFERENCES

Anderson, T.L. and Coauthors, 2005. An "A-Train" strategy for quantifying direct climate forcing by anthropogenic aerosols. *Bull. Amer. Meteor. Soc.*, **86(12)**, 1795-1809.

Auer, A. H. and D. L. Veal, 1970: The dimension of ice crystals in natural clouds. *J. Atmos. Sci.*, **6,** 919–926.

Ackerman, T. P., K.-N. Liou, F. P. J. Valero, and L. Pfister, 1988: Heating rates in tropical anvils. *J. Atmos. Sci.*, **45,** 1606-1623.

Baran, A. J., 2012. From the single-scattering properties of ice crystals to climate prediction: A way forward. *Atmos. Res.*, **112**, 45-69.

Baum, B.A., P. Yang, A.J. Heymsfield, A. Bansemer, B. H. Cole, A. Merrelli, C. Schmitt, and C. Wang, 2014. Ice cloud single-scattering property models with the full phase matrix at wavelengths from 0.2 to 100μm. *J. Quant. Spectrosc. Radiat. Transfer*, **146**, 123-139.

Baum, B.A., P. Yang, A.J. Heymsfield, S. Platnick, M.D. King, Y.X. Hu, and S.T. Bedka, 2005. Bulk scattering properties for the remote sensing of ice clouds. Part II: Narrowband models. *J. Appl. Meteor.*, **44(12)**, 1896-1911.

Baumgardner, D., H. Chepfer, G.B. Raga, and G.L. Kok, 2005: The shapes of very small cirrus particles derived from in situ measurements. *Geophys. Res. Lett.*, **32**, 1–4.

Chandrasekhar, S., 1960: *Radiative Transfer*. Courier Dover Publications.

Chepfer, H., S. Bony, D. Winker, M. Chiriaco, J.L. Dufresne, and G. Sèze, 2008. Use of CALIPSO lidar observations to evaluate the cloudiness simulated by a climate model. *Geophys. Res. Lett.*, **35(15)**.

Chiriaco, M., H. Chepfer, V. Noel, A. Delaval, M. Haeffelin, P. Dubuisson, and P. Yang, 2004. Improving retrievals of cirrus cloud particle size coupling lidar and three-channel radiometric techniques. *Mon. Wea. Rev.*, **132**, 1684-1700.

Cooper, S.J., T. S. L'Ecuyer, P. Gabriel, A. J. Baran, and G. L. Stephens, 2006. Objective assessment of the information content of visible and infrared radiance measurements for cloud microphysical property retrievals over the global oceans. Part II: Ice clouds. *J. Appl. Meteor. Climatol.*, **45**, 42-62.

Davis, S.M., L.M. Avallone, B.H. Kahn, K.G. Meyer and D. Baumgardner, 2009. Comparison of airborne in situ measurements and Moderate Resolution Imaging Spectroradiometer (MODIS) retrievals of cirrus cloud optical and microphysical properties during the Midlatitude Cirrus Experiment (MidCiX). *J. Geophys. Res. Atmos.*, **114(D2)**

Deschamps, P.Y., F. M. Bréon, M. Leroy, A. Podaire, A. Bricaud, J. C. Buriez, and G. Seze, 1994. The POLDER mission: Instrument characteristics and scientific objectives. *IEEE Trans. Geosci. Remote Sens.*, **32**, 598-615.

Dessler, A. E. and P. Yang, 2003: The distribution of tropical thin cirrus clouds inferred from Terra Modis data. *J. Climate*, **16,** 1241-1247.

Ding, Y., Yang, P., Bowman, K. P. & Baum, B. A., 2017. Comparison of Bayesian and Optimal Estimation approaches for the inference of ice cloud properties from Visible Infrared Imaging Radiometer Suite (VIIRS) infrared measurements. *J. Atmos. Oceanic Technol.,* in progress

Evans, K. F., S. J. Walter, A. J. Heymsfield, and G. M. McFarquhar, 2002. Submillimeter-wave cloud ice radiometer: Simulations of retrieval algorithm performance. *J. Geophys. Res. Atmos*, **107(D3)**.

Fu, Q., and K. N. Liou, 1992. On the correlated k-distribution method for radiative transfer in nonhomogeneous atmospheres. *J. Atmos. Sci.*, **49**, 2139-2156.

Garrett, K. J., P. Yang, S. L. Nasiri, C. R. Yost, and B. A. Baum, 2009. Influence of cloud-top height and geometric thickness on a MODIS infrared-based ice cloud retrieval. *J. Appl. Meteor. Climatol.*, **48**, 818-832.

Hansen, J. E. and J. W. Hovenier, 1971: The doubling method applied to multiple scattering of polarized light. *J. Quant. Spectrosc. Radiat. Transfer*, **11,** 809-812.

Hansen, J. E. and L. D. Travis, 1974: Light scattering in planetary atmospheres. *Space Science Reviews*, **16,** 527-610.

Hartmann, D. L., and Short, D. A., 1980. On the use of earth radiation budget statistics for studies of clouds and climate. *J. Atmos. Sci.*, **37,** 1233-1250.

Hartmann, D. L., J. R. Holton, and Q. Fu, 2001: The heat balance of the tropical tropopause, cirrus, and stratospheric dehydration. *Geophys. Res. Lett.*, **28,** 1969–1972.

Heidinger, A. K., Y. Li, B. A. Baum., R. E. Holz, S. Platnick, and P. Yang, 2015. Retrieval of cirrus cloud optical depth under day and night conditions from MODIS Collection 6 cloud property data. *Remote Sens.*, **7**, 7257-7271.

Herman, G. F., M. L. C. Wu, and W. T. Johnson, 1980. The effect of clouds on the earth's solar and infrared radiation budgets. *J. Atmos. Sci.*, **37**, 1251-1261.

Heymsfield, A.J. and C.M.R. Platt, 1984. A parameterization of the particle size spectrum of ice clouds in terms of the ambient temperature and the ice water content. *J. Atmos. Sci.*, **41(5)**, 846-855.

Holz, R. E., and Coauthors, 2015. Resolving ice cloud optical thickness biases between CALIOP and MODIS using infrared retrievals. *Atmos. Chem. Phys.*, **16**, 5075-5090.

Inoue, T., 1985. On the temperature and effective emissivity determination of semi-transparent cirrus clouds by bi-spectral measurements in the 10 μm window region. *J. Meteorol. Soc. Japan*, ***63***, 88-99.

Irvine, W. M., 1968: Diffuse reflection and transmission by cloud and dust layers. *J. Quant. Spectrosc. Radiat. Transfer*, **8,** 471-485.

Iwabuchi, H., S. Yamada, S. Katagiri, P. Yang, and H. Okamoto, 2014. Radiative and microphysical properties of cirrus cloud inferred from infrared measurements made by the Moderate Resolution Imaging Spectroradiometer (MODIS). Part I: Retrieval method. *J. Appl. Meteor. Climatol.*, **53**, 1297-1316.

Jensen, E. J., S. Kinne, and O. B. Toon, 1994: Tropical cirrus cloud radiative forcing-sensitivity studies. *Geophys. Res. Lett.*, **21,** 2023-2026.

Joiner, J., A. P. Vasilkov, P. K. Bhartia, G. Wind, S. Platnick, and W. P. Menzel, 2010. Detection of multi-layer and vertically-extended clouds using A-train sensors. *Atmos. Meas. Tech.*

JPSS, 2012. Joint Polar Satellite System (JPSS) cloud top Algorithm Theoretical Basis Document (ATBD). *Revision A.*

JPSS, 2013a. Joint Polar Satellite System (JPSS) Visible Infrared Imaging Radiometer Suite (VIIRS) Sensor Data Records (SDR) Algorithm Theoretical Basis Document (ATBD). *Revision C.*

JPSS, 2013b. Joint Polar Satellite System (JPSS) Operational Algorithm Description (OAD) document for VIIRS Cloud Optical Properties (COP) Intermediate Product (IP) Software. *Revision C.*

JPSS, 2014a. Joint Polar Satellite System (JPSS) VIIRS Cloud Mask (VCM) Algorithm Theoretical Basis Document (ATBD). *Revision E.*

JPSS, 2014b. Joint Polar Satellite System (JPSS) cloud effective particle size and cloud optical thickness Algorithm Theoretical Basis Document (ATBD). *Revision A.*

Lacis, A. A. and J. Hansen, 1974: A Parameterization for the absorption of solar radiation in the earth's atmosphere. *J. Atmos. Sci.*, **31,** 118-133.

Levenberg, K., 1944. A method for the solution of certain non-linear problems in least squares. *Quart. Appl. Math.*, **2**, 164-168.

Liou, K.-N., 1973: A numerical experiment on Chandrasekhar's discrete-ordinate method for radiative transfer: applications to cloudy and hazy atmospheres. *J. Atmos. Sci.*, **30,** 1303-1326.

Liou, K.N., 1986. Influence of cirrus clouds on weather and climate processes: A global perspective. *Mon. Wea. Rev.*, **114**, 1167-1199.

Liu, C., P. Yang, S. L. Nasiri, S. Platnick, K. G. Meyer, C. Wang, and S. Ding, 2015. A fast Visible Infrared Imaging Radiometer Suite simulator for cloudy atmospheres. *J. Geophys. Res. Atmos*, **120**, 240-255.

Liu, X., W. L. Smith, D. K. Zhou, and A. Larar, 2006: Principal component-based radiative transfer model for hyperspectral sensors: Theoretical concept. *Appl. Opt.*, **45,** 201-209.

Marquardt, D. W., 1963. An algorithm for least-squares estimation of nonlinear parameters. *SIAM J. Appl. Math.,* **11**, 431-441.

McClatchey, R. A., R. W. Fenn, J. E. A. Salby, F. E. Volz, and J. S. Garing, 1972. Optical properties of the atmosphere. *Air Force Cambridge Res. Lab. Tech. Rep.* AFCRL-72-0497, 108 pp.

McFarquhar, G. M., A. J. Heymsfield, J. Spinhirne, and B. Hart, 2000: Thin and subvisual tropopause tropical cirrus: Observations and radiative impacts. *J. Atmos. Sci.*, **57,** 1841-1853.

Menzel, W. P., and Coauthers, 2008. MODIS global cloud-top pressure and amount estimation: Algorithm description and results. *J. Appl. Meteor. Climatol.*, **47**, 1175-1198.

Meyer, K. G., 2004: The study of cirrus clouds using airborne and satellite data. M.S. thesis, Dept. of Atmos. Sci., Texas A&M University, 82 pp.

Mie, G., 1908, Beiträge zur optic trüber medien, speziell kolloidaler metallösungen, *Ann. Phys.*, **330**, 377–445.

Minnis, P., and Coauthors, 2011. CERES edition-2 cloud property retrievals using TRMM VIRS and Terra and Aqua MODIS data—Part I: Algorithms. *IEEE Trans. Geosci. Remote Sens.*, **49**, 4374-4400.

Minnis, P., and Coauthors, 2011. CERES edition-2 cloud property retrievals using TRMM VIRS and Terra and Aqua MODIS data—Part II: Examples of average results and comparisons with other data. *IEEE Trans. Geosci. Remote Sens.*, **49**, 4401-4430.

Moeller, C., D. Tobin, and G. Quinn, 2013, September. S-NPP VIIRS thermal band spectral radiance performance through 18 months of operation on-orbit. *SPIE*, 8866-88661N.

Moncet, J.-L., G. Uymin, and H. E. Snell, 2004: Atmospheric radiance modeling using the Optimal Spectral Sampling (OSS) method. *Proc. SPIE*, **SPIE-5425,** 368-374.

Nakajima, T., and M. D. King, 1990. Determination of the optical thickness and effective particle radius of clouds from reflected solar radiation measurements. Part I: Theory. *J. Atmos. Sci.*, **47**, 1878-1893.

Nasiri, S.L. and B.A. Baum, 2004. Daytime multilayered cloud detection using multispectral imager data. *J. Atmos. Oceanic Technol.*, **21(8)**, 1145-1155.

Newman, S. M., J. A. Smith, M. D. Glew, S. M. Rogers, and J. P. Taylor, 2005: Temperature and salinity dependence of sea surface emissivity in the thermal infrared. *Quart. J. Roy. Meteor. Soc.*, **131**, 2539–2557

Parol, F., J. C. Buriez, G. Brogniez, and Y. Fouquart, 1991. Information content of AVHRR channels 4 and 5 with respect to the effective radius of cirrus cloud particles. *J. Appl. Meteor.*, **30**, 973-984.

Pavolonis, M.J. and A.K. Heidinger, 2004. Daytime cloud overlap detection from AVHRR and VIIRS. *J. Appl. Meteorol*., **43(5)**, 762-778.

Plass, G. N. and G. W. Kattawar, 1968: Monte Carlo calculations of light scattering from clouds. *Appl. Opt*, **7,** 415-419.

Platnick, S., and Coauthors, 2017: The MODIS cloud optical and microphysical products: Collection 6 updates and examples from Terra and Acqua, *IEEE Trans. Geosci. Remote Sens.*, **55,** 502–525, doi:10.1109/TGRS.2016.2610522.

Poore, K.D., J. Wang and W.B. Rossow, 1995. Cloud layer thicknesses from a combination of surface and upper-air observations. *J. Climate*, **8(3)**, 550-568.

Rienecker, M. M., and Coauthors, 2011. MERRA: NASA's modern-era retrospective analysis for research and applications. *J. Climate*, **24**, 3624-3648.

Rodgers, C.D., 2000. *Inverse methods for atmospheric sounding*. World scientific. 238pp.

Segelstein, D., 1981. The complex refractive index of water. Ph.D. dissertation, University of Missouri--Kansas City

Sissenwine, N., M. Dubin, and H. Wexler, 1962. The US standard atmosphere, 1962. *J. Geophys. Res.*, **67**, 3627-3630.

Stamnes, K., S. C. Tsay, K. Jayaweera, and W. Wiscombe, 1988: Numerically Stable Algorithm for discrete-ordinate-method radiative transfer in multiple scattering and emitting layered media. *Appl. Opt.*, **27,** 2502-2509.

Stephens, G.L., and Coauthors, 2002. The CloudSat mission and the A-Train: A new dimension of space-based observations of clouds and precipitation. *Bull. Amer. Meteor. Soc.*, **83**, 1771-1790.

Stubenrauch, C.J., A. Chédin, G. Rädel, N. A. Scott, and S. Serrar, 2006. Cloud properties and their seasonal and diurnal variability from TOVS Path-B. *J. Climate*, **19**, 5531-5553.

Wang, C., P. Yang, B. A. Baum, S. Platnick, A. K. Heidinger, Y. Hu, and R. E. Holz, 2011. Retrieval of ice cloud optical thickness and effective particle size using a fast infrared radiative transfer model. *J. Appl. Meteor. Climatol.*, **50**, 2283-2297.

Wang, C., P. Yang, and X. Liu, 2015. A high-spectral-resolution radiative transfer model for simulating multilayered clouds and aerosols in the infrared spectral region. *J. Atmos. Sci.*, **72(2)**, 926-942.

Wang, C., S. Platnick, Z. Zhang, K. Meyer, and P. Yang, 2016. Retrieval of ice cloud properties using an optimal estimation algorithm and MODIS infrared observations: 1. Forward model, error analysis, and information content. *J. Geophys. Res. Atmos*, **121**, 5809-5826, doi: 10.1002/2015JD024526.

Wang J. and W.B. Rossow, 1998. Effects of cloud vertical structure on atmospheric circulation in the GISS GCM. *J Climate*, **11**, 3010–29.

Wang, J., W.B. Rossow, and Y. Zhang, 2000. Cloud vertical structure and its variations from a 20-yr global rawinsonde dataset. *J Climate,* **13(17)**, *3041-56.*

Webster, P.J. and G.L. Stephens, 1980. Tropical upper-tropospheric extended clouds: inferences from winter MONEX. *J. Atmos. Sci.*, **37**, 1521–41.

Wei, H., P. Yang, J. Li, B. A. Baum, H. L. Huang, S. Platnick, Y. Hu, and L. Strow, 2004: Retrieval of semitransparent ice cloud optical thickness from Atmospheric Infrared Sounder (Airs) Measurements. *IEEE Trans. Geosci. Remote Sens.*, **42,** 2254-2267.

Wind, G., S. Platnick, M.D. King, P.A. Hubanks, M.J. Pavolonis, A.K. Heidinger, P. Yang, and B.A. Baum, 2010. Multilayer cloud detection with MODIS near-infrared water vapour absorption band. *J. Appl. Meteorol. Climatol.*, **49(11)**, 2315-2333

Yang, P., K. N. Liou, L. Bi, C. Liu, B. Yi, and B. A. Baum, 2015. On the radiative properties of ice clouds: Light scattering, remote sensing, and radiation parameterization. *Adv. Atmos. Sci.*, **32**, 32-63.

Yu, H., and Coauthors, 2006. A review of measurement-based assessments of the aerosol direct radiative effect and forcing. *Atmos. Chem. and Phys.*, **6(3)**, f613-666.

Zhang, Z., and Coauthors, 2007: A fast infrared radiative transfer model based on the adding-double method for hyperspectral remote-sensing applications. *J. Quant. Spectrosc. Radiat. Transfer*, **105**, 243–263.